Laser-Assisted Synthesis and Time-Resolved Growth Control of Two-Dimensional Quantum Materials

by

Nurul Azam

A dissertation submitted to the Graduate Faculty of
Auburn University
in partial fulfillment of the
requirements for the Degree of
Doctor of Philosophy

Auburn, Alabama
December 10, 2022

Keywords: 2D Materials, Quantum Materials, TMDC, Laser-assisted Synthesis, Time-resolved Synthesis, Vacancy Tailoring

Approved by

Masoud Mahjouri-Samani, Chair, Assistant Professor of Electrical and Computer Engineering
Guofu Niu, Professor of Electrical and Computer Engineering
Michael C. Hamilton, Professor of Electrical and Computer Engineering
Mark L. Adams, Associate Professor of Electrical and Computer Engineering
Marcelo A. Kuroda, Associate Professor of Physics

ABSTRACT

Two-dimensional (2D) layered materials, including transition metal dichalcogenides (TMDCs), have recently been at the heart of quantum materials and information sciences research due to unusual properties associated with their firmly defined dimensionalities. Many efforts have focused on developing new methods for the accelerated growth and discovery of 2D materials, including physical and chemical vapor deposition techniques. However, synthesizing these multi-component crystals in the gas phase has been extremely challenging due to complex and uncontrolled gas-phase reactions and flow dynamics. A novel laser-assisted synthesis technique (LAST) has been demonstrated in response to existing growth complexities to accelerate the growth of 2D materials in this study. This novel bottom-up synthesis approach facilitates the growth of various 2D materials directly from stoichiometric powders through laser vaporization. The directed laser heating allows pressure-independent decoupling of the growth and evaporation kinetics enabling the use of stoichiometric powder as precursors for the growth of high-quality 2D materials, including MoS_2, $MoSe_2$, WSe_2, and WS_2.

Controlling and understanding the growth of atomically-thin transition metal dichalcogenides (TMDCs) monolayer two-dimensional (2D) materials is vital for next-generation 2D electronics and optoelectronic devices. However, their growth kinetics is not fully observed or well understood due to the bottlenecks associated with the existing synthesis methods. In pursuit of resolving these issues, this study further explored and demonstrated the time-resolved and ultrafast growth of 2D materials by this novel laser-based synthesis approach that enables rapid initiation and termination of the vaporization process during crystal growth. Stoichiometric powder (e.g., WSe_2) minimizes the complex chemistry, while the vaporization and growth process allows rapid initiation/termination control over the generated flux. An extensive set of experiments

is performed to understand the growth evolution from both feedstock supply and surface diffusion perspective, achieving sub-second growth as low as 10 ms along with the record-breaking 100 μm/s growth rate on a non-catalytic substrate such as Si/SiO_2. The process parameter further predicts that this ultrafast crystal growth rate is highly reproducible and scalable.

Tuning the structural and electronic properties of atomically-thin two-dimensional (2D) materials via defect and vacancy engineering is the key to their potential use in various applications, including electronics, energy, and sensing devices. Vacancies are, for instance, becoming highly promising for enhanced interaction of gases and biomolecules with 2D materials in energy and sensing applications. However, the deterministic generation of desirable vacancies with tunable concentration remains a challenge in 2D materials due to the limitations in the current growth methods, such as the complex reaction chemistries and gas flow dynamics. Therefore, engineering defects and vacancies in 2D materials have been mainly limited to destructive top-down processes such as heating, ion bombardments, and laser post-processing. In order to address these challenges, this study introduced a single-step bottom-up synthesis approach of LAST to grow monolayer $MoSe_2$ crystals with tunable vacancy concentrations. This method utilizes the spatiotemporal properties and adjustable power density of the lasers to control the vaporization dynamics of the stoichiometric $MoSe_2$ powders. Such a mechanism in the vaporization allows us to grow tunable stoichiometry monolayer $MoSe_{2-x}$ crystals on the substrates. The localized and time-controlled (250 ms to 2 s) vaporization of the $MoSe_2$ powder by a CO_2 laser enables the formation of monolayer crystals with controlled vacancy concentrations ranging from ~1 to 20%. The effects of laser power, laser irradiation time, and background pressure on the vacancy tuning range and subsequent properties of the crystals are investigated and quantified using Raman and

photoluminescence spectroscopy, scanning transmission electron microscopy (STEM), and time-correlated single-photon counting (TCSPC).

LAST facilitates observation and understanding of the 2D crystal evolution and growth kinetics with time-resolved and sub-second time scales. Furthermore, this bottom-up synthesis is a promising approach that allows deterministic vacancy tuning for future electronics, particularly gas and bio-sensing applications, without the need for further post-processing and potential structural disruption of the crystals. Overall, this research work presents a general yet straightforward approach to accelerating the synthesis and discovery of emerging quantum materials.

ACKNOWLEDGMENTS

Firstly, I would like to express my sincere gratitude to my academic advisor **Dr. Masoud Mahjouri-Samani** for his constant guidance, assistance, and financial support during my Ph.D. study and research at Auburn University. I would also like to thank **Dr. Guofu Niu**, **Dr. Michael C. Hamilton**, and **Dr. Mark Adams** for their review and commentary. I also thank **Dr. Marcelo A. Kuroda** for serving as the University Reader for this work. Their comments and advice are instrumental in build of this dissertation.

Special thanks to **Dr. Mengkun Tian** and the Materials Characterization Facility at the Institute for Electronics and Nanotechnology (IEN), Georgia Tech, for the STEM characterization of the grown 2D monolayer crystals. Special thanks also go to **Dr. Matthew G. Boebinger** and **Dr. Raymond R. Unocic** for conducting the STEM characterization for vacancy quantification at the Center for Nanophase Materials Sciences (CNMS), Oak Ridge National Laboratory, a U.S.Department of Energy (DOE), Office of Science User Facility. I would like to extend my sincere thanks to **Dr. Jordan Hachtel** for his assistance with defect concentration analysis algorithms. At the same time, I appreciate the support from the Alabama Micro/Nanoelectronic Science and Technology Center (AMNSTC) for providing access to the cleanroom facility.

I would like to thank my past and present lab-mates **Salah Elafandi, Baha Yakupoglu, Zabihollah Ahmadi, Parvin Fathi-Hafshejani, Suman Jaiswal, Adib Taba,** and **Aarsh Patel** for their cooperative support and encouragement during my Ph.D. study and stay at Auburn. I am thankful to the department of **Electrical and Computer Engineering (ECE)** of Auburn University for creating a unique environment for learning and working for the last five years. I appreciate the ECE department's staff members for their help on numerous occasions.

On a personal note, I would like to dedicate all my efforts to this research study in memory of my departed brother **Sahed Alam**, who was a mentor, a teacher, and a financial supporter at every step of my academic and personal endeavor. I am also grateful to my mother, **Hasina Begum**, and my sisters, **Jannatul Ferdous** and **Jannatul Naeem**, for their unwavering support and inspiration despite all difficulties and challenges.

I would like to thank my wife, **Yeasmin Hasan,** for her support during this journey. I would also appreciate my little daughter **Auritree Arin** for filling moments with joy, hope, and love.

TABLE OF CONTENTS

LIST OF FIGURES

LIST OF TABLES

LIST OF ABBREVIATIONS

2D Materials	Two-Dimensional Materials.
QM	Quantum Materials.
LASER	Light Amplification by Stimulated Emission of Radiation.
TMDC	Transition Metal Dichalcogenides.
LAST	Laser-Assisted Synthesis Technique.
CVD	Chemical Vapor Deposition.
VPC	Vapor-Phase Chalcogenization.
MOCVD	Metal-Organic Chemical Vapor Deposition.
MBE	Molecular Beam Epitaxy.
PLD	Pulse Laser Deposition.
PL	Photoluminescence spectroscopy.
AFM	Atomic Force Microscopy.
STEM	Scanning Transmission Electron Microscopy.
HAADF	High-Angle Annular Dark-Field.
EDS	Energy Dispersive X-ray Spectroscopy.
TCSPC	Time-Correlated Single-Photon Counting.
PMMA	Poly(methyl methacrylate).

CHAPTER 01

INTRODUCTION TO TWO-DIMENSIONAL QUANTUM MATERIALS

1.1 Material's Dimension

In the last few decades, nanostructured materials have drawn intense attention due to their high surface area, unusual size effects, and substantially enhanced kinetics with superior performance compared to their bulk counterparts.[1, 2] These nano-structure materials can be classified depending on different attributes such as size, dimension, composition, shape, and origin. For example, depending on dimensions, nanostructured material can be categorized as zero-dimensional (0D), one-dimensional (1D), two-dimensional (2D), and three-dimensional (3D) nanomaterials.[3] The interesting thing regarding these classifications is the ability to predict the distinctive properties of the Nanomaterials.[2] This chapter mainly focuses on two-dimensional materials (2D) for their extraordinary properties, which justify the demand for their efficient synthesis and application in next-generation science and technologies. In the later part of this chapter, the challenges in the synthesis, growth control, and vacancy tuning of 2D quantum materials have also been discussed along with outline of this study.

1.2 Two-dimensional Materials

Mechanical exfoliation of graphene first introduced the world to the astonishing electronic[4], optoelectronic[5, 6], and mechanical[7] properties of atomically-thin two-dimensional (2D) systems[8, 9]. Two-dimensional materials are crystalline solids containing a few nanometers or a less thick single layer of atoms. Typically, 2D materials are layered structures where each layer is chemically bonded in-plane while those layers are held together by Van der Waals force in their

bulk form.[10, 11] When a layer is isolated from bulk materials, electrons' motion in the single layer is confined to the two-dimensional plane; as a result, quantum mechanics govern many properties. The absence of van der Waals interactions, increased surface area-to-volume ratio, quantum confinement, and broken inverse symmetry are the critical properties of 2D materials.[12] These properties lead to a wide range of applications in energy, electronics, and sensing, to mention a few. Preceding discussions are structured chronologically, from the discovery of the first 2D materials to the recent update in the field of 2D materials in a brife.

1.3 Graphene

It was believed until 2004 that 2D crystals such as graphene were thermodynamically unstable and could not exist in the free state.[9] In 2004, two researchers at the University of Manchester, Professor Andre Geim and Professor Kostya Novoselov isolated the 2D crystals of only a few atomic layers of thick graphite and showed field-effect transistors constructed from those flakes.[13] Research reveals that 2D crystals such as graphene shows high crystal quality and a contentious crystal nature with sp^2-bonded carbon atoms assembled in a hexagonal lattice[14], as shown in **Figure 1.1 a-b**. These carbon atoms are bonded together at the length of 0.142 nm. Later, many more exotic properties start to unfold, such as charge carriers moving into crystals thousands of interatomic distances without scattering.[9] Graphene electrons behave similarly to massless Dirac fermions and gain high mobility ~50,000 $cm^2\ V^{-1}\ s^{-1}$ at electron densities of $2x10^{11}\ cm^{-2}$, which enables the study of quantum phenomena up to room temperature.[15] The origin of graphene's high mechanical strength and chemical inertness is attributed to the strong C–C bonds and the absence of dangling bonds in the basal plane, respectively.[16]

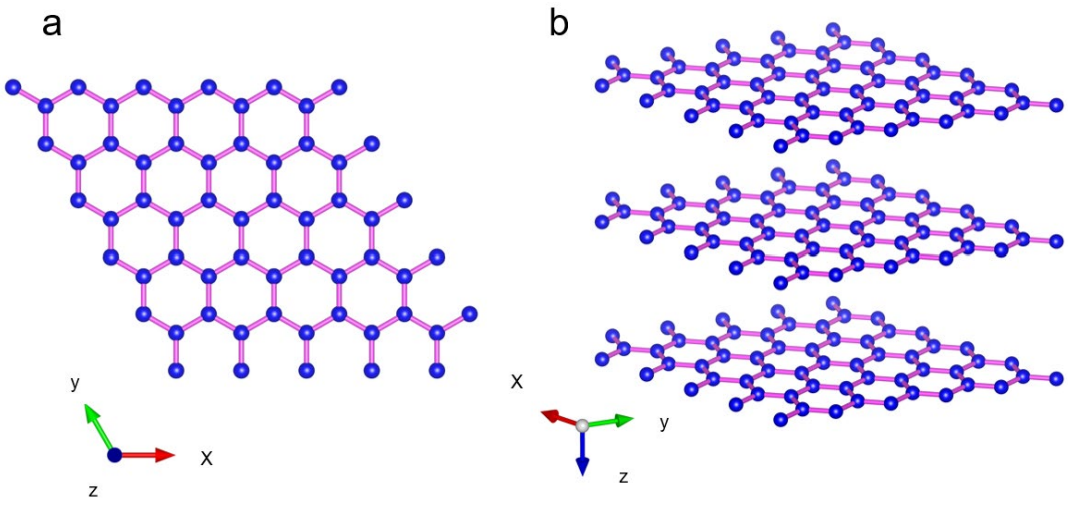

Figure 1.1. In a graphene layer (XY plane), each atom is attached through a stable σ-bond for its other three nearest neighboring atoms and forms a honeycomb lattice with a C-C bond length of 0.142 nm(a).[14] In the bulk form, these layers are attached with weak out-of-plane (along the Z-axis) van der Waals forces (b) Data retrieved from the Materials Project for C (mp-48) from database version v2021.11.10.

Furthermore, high surface area (2630 m^2g^{-1}), excellent thermal conductivity (5000 W m^{-1} K^{-1}), very high Young's modulus 1 Tpa, and very high light transmittance ~98%, and many other unusual properties lead to the discovery of graphene to receive the 2010 Nobel prize in physics.[13, 14] Because of its unique novel properties, graphene makes a wide variety of practical applications possible in electronics, sensing, medical and industrial applications.[17, 18]

1.4 Beyond Graphene

Although the massive success of graphene introduces many exotic properties and applications, graphene shortcomings, such as lack of bandgap[19, 20], and doping challenges, diminish graphene's chances of finding a robust electronic application. Since Moore's law drives the semiconducting community to find an alternative to silicon technology, the electronic device

community put much effort into forcing graphene to perform in the same way as the semiconductor and making fast transistors owing to graphene's extreme mobility.[21] Unfortunately, those attempts have been unsuccessful entirely or caused low mobility of electrons—beating the critical reasons for employing graphene. Since the mobility of semiconductors is coupled to the band structure, mobility decreases with increasing bandgap.[21] Furthermore, the absence of a band gap has limited the graphene field-effect transistors' achievable on/off ratio (FETs), typically around 5 in top-gated graphene FETs.[22] Since the logic circuit requires the ability to switch current on and off; it gradually became evident that graphene is unsuitable for application in transistors. However, Graphene's role as a pioneer in 2D materials unleashed the search for other layered materials similar to graphene, such as two-dimensional (2D) van der Waals (vdW)[23] materials and many others.

After discovering graphene, the 2D materials family extended into the compound and mono-elemental materials. Some examples of recent mono-elemental 2D materials are silicene, germanene, stanene, phosphorene, tellurene, and borophene, which are the 2D counterpart of their bulk forms of Si, Ge, Sn, P, Te, and B, respectively[18]. High mobilities and semiconducting behavior make some mono-elemental 2D materials find their applications in electronics and optoelectronics. However, in an ambient atmosphere, these elemental 2D materials are commonly volatile and make the synthesis, processing, and characterization of these materials challenging.[16] On the other hand, transition metal dichalcogenides (TMDC) and Hexagonal boron nitride (h-BN) are the most studied compound form of 2D materials. It should be noted that Hexagonal boron nitride (h-BN) is a large bandgap insulator with a bandgap of ~ 5 eV, while TMDCs are mainly semiconducting materials with band gaps ranging from 1-2eV as shown in **Figure 1.2 a-c**.

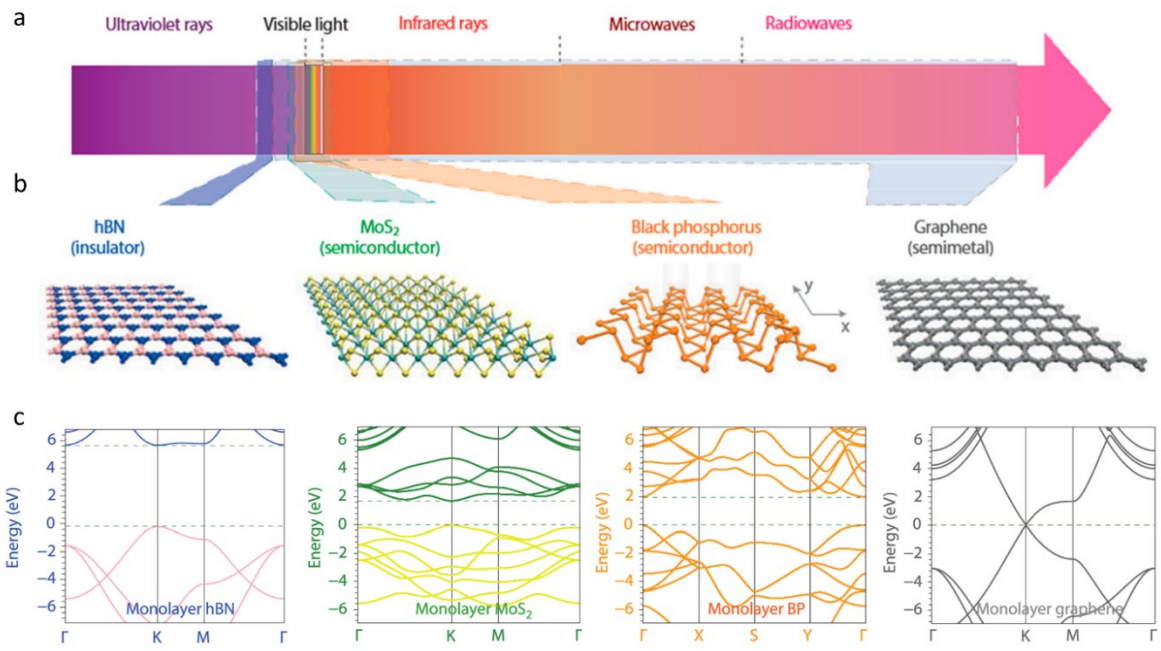

Figure 1.2 Energy spectrum (a) of the key representative 2D materials such as hexagonal boron nitride (h-BN), transition metal dichalcogenides (TMDCs), black phosphorous (BP), and graphene and their crystal structure (b). Electronic band structures of these corresponding 2D materials show graphene behaves as a conductor and hBN as an insulator while both TMDC and BP show semiconducting properties (c) Reprinted (adapted) with permission from reference[24]. Copyright © 2014, Nature Publishing Group, a division of Macmillan Publishers Limited.

1.5 Transition Metal Dichalcogenides

After the discovery of graphene, Transition metal dichalcogenides (TMDCs)[4, 25] caught the scientific communities attention among all other layer-structured materials. MoS_2 is the most researched two-dimensional material after graphene, which belongs to this TMDCs family.[4] TMDCs are generally MX_2 semiconductors where M represents a transition metal group atom (e.g., Mo or W) and X represents a chalcogen group atom (e.g., S, Se, or Te) [18, 26, 27], as shown in **Figure 1.3**. These different transition metal and chalcogen atoms form 40 different layered TMD

compounds.[28] Interestingly, along the plane, TMDCs show strong covalent bonds, while out of the plane, they exhibit weak interlayer Van der Waals (VdW)[10,29] interaction **Figure 1.3a-c**. Mechanical or liquid exfoliation can easily overcome the weak out-of-plane bonding and enable the extraction of a single or a few layers from their bulk materials.[30]

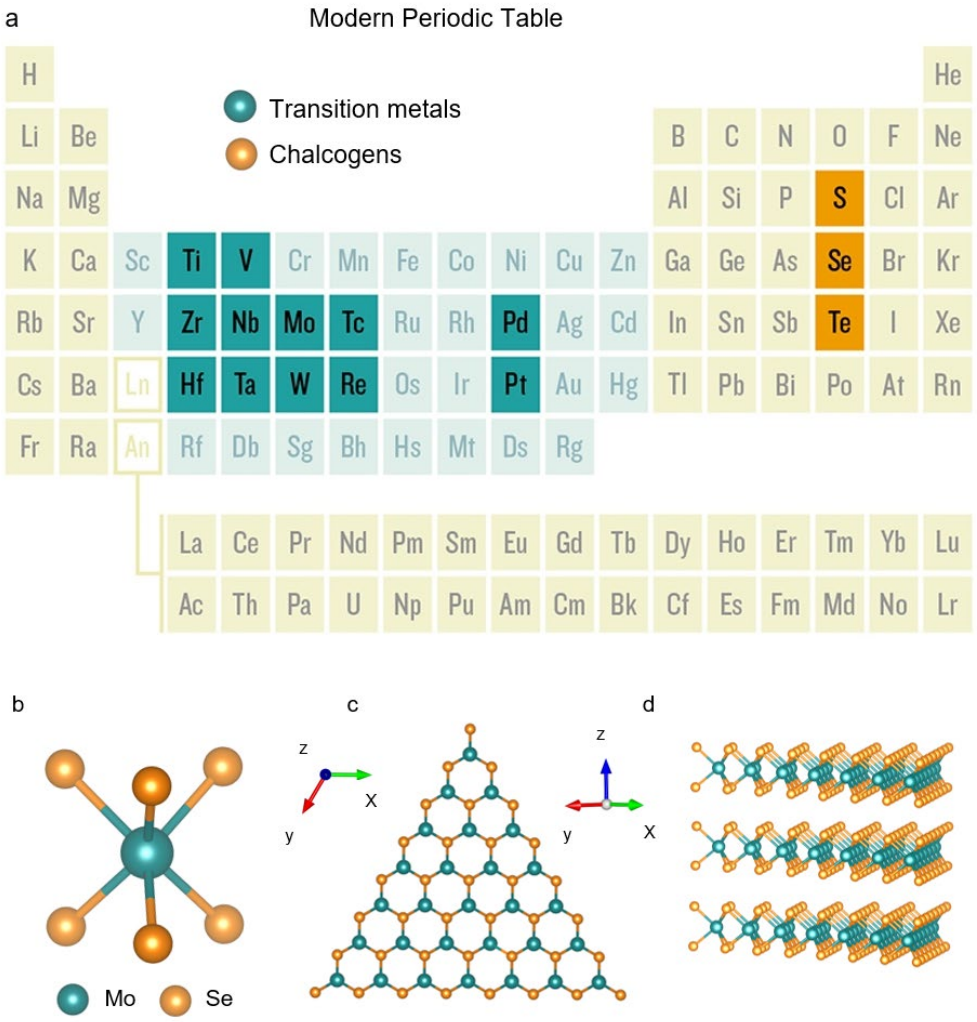

Figure 1.3 a) Modern periodic table shows the elemental zoo for a possible combination of the TMDC layered materials b) Unit cell of a TMDC b) Hexagoanally oriented TMDC seen from Z-axis d) three monolayer forming the layered structure seen from XY plane.

Physically, these TMDCs are known as layered van der Waals solids and display numerous structural phases, such as the 2H, 1T, 1T', and $1T_d$.[31] Among these phases, bulk 2H TMDCs (e.g., MoS_2) exhibit indirect band-gap semiconducting behavior.[31] MoS_2, $MoSe_2$, WS_2, and WSe_2 show 1.0–1.29 eV, 1.1 eV, 1.3–1.4 eV, and 1.2 eV indirect band gaps, respectively, in bulk forms.[32] Yet, in the monolayer forms, these TMDCs materials transit from indirect band gap materials to direct band gap materials because of the quantum restraint and lack of interlayer interaction, as shown in **Figure 1.4**.[13] In contrast to bulk counterparts, TMDCs, such as MoS_2 (1.8-1.9eV)[33], $MoSe_2$ (1.5-1.6eV)[34], WS_2 (1.81-2.1eV)[34], and WSe_2 (1.6-1.7 eV)[33], show desirable band gap ranging from the visible to the near-infrared spectrum [32, 35]. Because of this indirect to direct bandgap transition, the photons generated by the radiative recombination of electrons and holes in direct-bandgap semiconductors occur more significantly.[35]

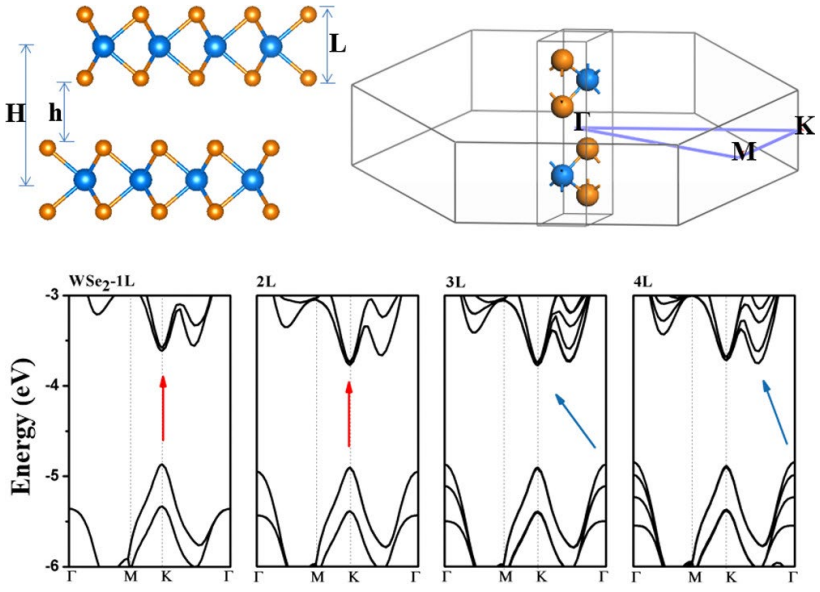

Figure 1.4 The band structure progression of a representative 2H-TMDs WSe_2 as a function of the layer number at the first Brillouin zone. Reprinted (adapted) with permission from reference [36]. Copyright © 2016 American Chemical Society.

This direct-bandgap [31, 37] at the monolayer facilitates strong light-matter interactions and enables applications of these TMDSc in high-end electronics[38-41] optoelectronics[35, 42-44], flexible electronics[27], biosensors[45], solar cells, photodetectors[24,46], light-emitting diodes, unlike graphene.[35, 47] Electronic devices such as field- effect transistors (FETs) and memories are potential electronic[48, 49] applications of TMDCs. In addition, TMDCs exhibit many quantum applications[50], such as spintronics[4, 51,52], and valleytronics[53]. As a result, monolayer TMDCs have become the emerging class of atomically thin semiconducting materials and hold excellent capability for fundamental sciences and technologies.[54-57]

1.6 Synthesis of Mono- and Few-Layer TMDC Single Crystals

"There is Plenty of Room at the Bottom" lecture at the annual meeting of the American Physical Society (APS) On Dec 1959, Richard P. Feynman raised some crucial questions regarding layered structured materials such as "What could we do with layered structures with just the right layers? What would the properties of materials be if we could really arrange the atoms the way we want them?".[32, 58] Eventually last two decades Feynman vision revived since the discovery of graphene and other low dimensional materials shows their characteristics different from the bulk properties indeed.[1] As a result, research communities have made synthesizing two-dimensional nano-structured materials one of the key focus areas in recent years. Layered materials are characterized by extended crystalline planar structures held together by strong in-plane covalent bonds and weak out-of-plane van der Waals forces. Fortunately, many-layered form van der Waals minerals are available in nature with various crystal structures and chemical compositions, many of which properties are yet to explore. [59] As pointed out in **Figure 1.3**, different combinations of transition metal atoms and chalcogen atoms can form 40 different layered TMDC compounds[28]. Generally, 2D materials synthesis can be divided into two broad categories, such as top-down and

bottom-up approaches. Both categories provided some advantages and disadvantages, which have been discussed below.

1.6.1 Top-down Approaches

Mono and few-layer MoS_2 crystals were among the first synthesized and studied MX_2 structures by a top-down mechanical exfoliation[8, 60-63] method. Soon after, the closely analogous materials, including WS_2, $MoSe_2$, and WSe_2 crystals, became the center of attention in the emerging quantum materials and devices community.[64] Laser thinning[65] and liquid-phase exfoliation[66] are the other top-down methods for separating a single layer from the bulk material. However, these top-down techniques were uncontrollable and limited to a small scale.[67, 68]

1.6.2 Bottom-up Approaches

The limitations of the top-down exfoliation approaches have shifted the synthesis perspective to bottom-up[60] methods that rely mainly on creating M^{n+} and nX^{2-} in the gas phase[60] for 2D growth. Several gas phase techniques such as chemical vapor deposition (CVD) [69-71], metal-organic chemical vapor deposition (MOCVD)[69], molecular beam epitaxy (MBE)[72], and pulse laser deposition (PLD)[73-77] have been successful in creating few high-quality 2D crystals and thin films.[78] However, the significant challenges in these growth environments include the choice of desired precursors, proper precursor transport and mixing, controlled chemical reactions, the formation of byproducts, contaminations, and complex growth kinetics.[79,80] Such complexities are common problems in most bottom-up synthesis approaches. For instance, the growth of MoS_2 crystals in CVD requires the evaporation of molybdenum and sulfur-containing precursors, including MoO_3 and sulfur in different heat zones of the tube furnace followed by precursor transport to the substrate using a carrier and reaction gases ($Ar+H_2$). Similarly, MOCVD requires the flow of metal-organic gasses such as $Mo(CO)_6$ and $(C_2H_5)2S$ for chemical reaction and growth

processes. MBE[81, 82] requires a high vacuum system for elemental molybdenum and sulfur evaporation and transport to the substrate for chemical reactions and growth.[14] However, PLD[63,75,76] is a promising approach in the stoichiometric transfer of precursor materials to the substrate but results in the formation of thin films with nano-domains and many grain boundaries. These problems have significantly hindered the rapid synthesis and discovery of emerging 2D materials and devices.

Recently, many efforts have been made to modify and enhance the efficiency of the CVD synthesis process[79]. For example, Zhou et al. proposed molten-salt-assisted CVD[71, 83] for reducing the growth temperature. Although this method slightly reduces the growth temperatures, the addition of salt adds further complexities to the CVD process. In pursuing a simple and universal solution, developing novel synthesis methods for controllable, reproducible, fast, and simplified growth of high-quality mono and few-layer 2D TMDCs has been highly demanded.

1.7 Time-Resolved Growth Dynamics

CVD has been the most common synthesis technique among bottom-up synthesis approaches, and most crystal growth and kinetics studies have been performed in this process. For instance, the ultrafast growth dynamics studies in the CVD have been done through process modification such as reverse flow process[84], substrate engineerings such as the use of metal[85] and catalytic as substrate [86, 87], and precursor modifications such as the use of salt[71, 88]. However, the crystal growth evolution is still a mystery due to the technical bottleneck of time-resolved growth in the current synthesis methods. The time-resolved growth is a powerful technique to shed light on the crystal evolution mechanisms from both spatial and temporal perspectives.

The lack of time-resolved studies for 2D materials growth evolution is due to the fundamental limitation of conventional synthesis processes. The initiation and termination of the growth process should be highly controllable within a millisecond time regime, which is not possible, for example, in conventional CVD due to the ultralong (typically tens of minutes to hours)[89] and complex growth processes. After the growth process, it is impossible to track each crystal's birth and growth time. The lack of such information makes it challenging to identify the sources of variation (e.g., defects), growth rate, and process impact on each crystal. For example, smaller crystals could be the ones that were grown at the beginning of the process to a large size but remained under thermal exposure for a long time resulting in the re-evaporation and shrinkage, or maybe they were grown for a short time at the end of the growth process. Similar questions can also be valid for defect evolution and growth kinetics.

Moreover, the ability to independently control the vaporization and growth temperatures is crucial since equilibrium must be settled between supplies of feedstock and surface diffusion rate. For example, if the feedstock supply is more than the surface diffusion rate, then vertical growth takes place while less feedstock supply quenches the growth. In these circumstances, to accelerate the lateral surface diffusion, the crystal growth temperature needs to increase[89]. However, elevated growth temperatures tend to vaporize the precursor before the growth starts or may re-evaporate the already-grown crystals. Besides, crystal growth becomes more challenging at low feedstock supply for non-catalytic substrates such as Si/SiO_2 and sapphire in conventional CVD. Furthermore, nucleation reduction is regarded as a significant role in creating large single crystal[90] and since forming nucleation is a quantum probabilistic scenario, the nucleation site increases at a slow growth rate[91]. Hence, due to these challenges, time-resolved and ultra-fast growth rates have not been possible by conventional synthesis methods.

1.8 Vacancies in 2D Materials

Due to the higher volatility of the chalcogen atoms, TMDC layers are more prone to chalcogen vacancies[92]. Structural defects can form during the synthesis due to the growth kinetics, which could substantially impact their properties.[93,94] Sometimes, these new properties are desirable for various applications and can be used to understand fundamental science. For example, defect engineering plays a vital role in understanding and regulating the properties of graphene[93]. Similarly, for the 2D TMDC crystals, deliberately creating chalcogen vacancies in a controlled manner can effectively modulate their physical, chemical, and electronic properties[95, 96] with a wide range of applications such as energy, sensing, photonics, and spintronics.[97, 98]

For example, several recent reports demonstrated the single-photon emission due to atomistic defects in the atomically thin layer of MoS_2 crystals.[99, 100] In addition, the carrier concentration of 2D TMDCs can be precisely controlled by the single-atom vacancies to alter the conductivity.[101] Furthermore, a recent report[102] shows thermodynamically stable defects in $MoSe_2$, such as single (V_{se}) or double (V_{se2}) point vacancies, demonstrate better catalytic activity than MoS_2 in hydrogen evaluation reaction (HER) and potentially can replace expensive Pt-based catalysts.

One of the potential roles of defects and vacancies in 2D materials is their significant impact on gas and biosensing applications.[103, 104] Since the surface of the pristine 2D materials is chemically inert, the interaction of molecules and atoms typically takes place via a weak physisorption process.[105] The vacancy engineering in 2D materials enables the chemisorption of the atoms and molecules with the vacancies that enhance the device response in 2D gas and biosensors.[103, 104] For instance, It has been reported that the more defective 2D monolayer allows more intense interaction of gas molecules with the 2D materials for sensing.[103, 104, 106, 107]

Therefore, the controlled engineering of such defects in 2D material is crucial for gas and bio-sensing implications[19].

1.9 Deterministic Vacancy Generation in 2D Materials

In recent years, there has been rapid progress in the synthesis and characterization of chalcogen vacancy engineering in 2D TMDCs.[108] In this period, numerous strategies ranging from direct synthesis to post-growth processing have been implemented to create various types of defects, including chalcogen vacancies.[109] Depending on the strategies to deliberately induce defects in 2D materials, the synthesis approaches can be separated into two groups, including the top-down and bottom-up methods.[110]

The top-down synthesis mainly relies on post-processing approaches [95] including electron-beam irradiation[23,111], laser irradiation[112] plasma etching[113], ultraviolet exposure[114], ion-beam irradiation[115, 116], and ozone treatment[117] to produce defects controllably. The top-down approach typically starts with using already synthesized pristine crystals followed by post-processing steps to generate the defect and vacancies. Different types of defects, such as chalcogen atom vacancies (single or double), metal vacancies[118], antisite[119], and line defects[120], have been manufactured in these methods. However, control over the formation, distribution, and type of defects while keeping the integrity of these crystals are still a challenge in such top-down post-processing techniques.[121] Typically, the low-energy nature of the already defective positions in the crystal compared to the pristine location makes these sites more vulnerable to the subsequent beam (i.e., ions or electrons) interaction and thus causes aggressive degradation and decomposition of the crystals.[122] Furthermore, reactive plasma etching and electron beam irradiation are limited by directionality for large-scale synthesis.[96]

On the other hand, recently reported bottom-up strategies, including chemical vapor deposition (CVD)[123], vapor-phase chalcogenization (VPC)[124], and liquid phase synthesis[96], successfully induced vacancies in the TMDC monolayers. However, these processes involved multiple stages with complex precursor mixing chemistry, long growth time, and uncertainty in yield. For example, in the conventional gas-phase processes, due to the use of multiple precursors (e.g., MoO_3 and Se for $MoSe_2$ in the CVD process), control of the gas mixing and chemistry on the surface of the substrate makes it difficult to induce controlled vacancies into the crystals. Furthermore, CVD parameters such as the carrier gas's flow rate, the substrate's position, and temperature significantly impact the crystal's size and quality. As a result, the CVD parameters vary from sample to sample and lab to lab. Thus, vacancies generated in these bottom-up processes are mostly uncontrolled, i.e., vacancies are created unintentionally during the synthesis process. As a results, controlled generation of vacancies with tunable concentrations in semiconducting TMDCs remains a challenge.

1.10 Outline of Dissertation

This dissertation introduced several original findings to address the challenges discussed in sections **1.6-1.9.**

In Chapter 1, 2D materials are introduced as a low-dimensional nanomaterials sub-class. Primary 2D materials such as graphene and beyond graphene are discussed with their critical properties. The discussion clearly shows the capability of the transitional metal dichalcogenide among the 2D materials for their stability and many potential applications in science and technology. The critical problems in synthesizing TMDC 2D materials have been discussed from both top-down and bottom-up perspectives. Based on recent literature, the challenge in time-resolved synthesis and deterministic vacancy tuning of 2D have also been discussed in this chapter.

In Chapter 2, A novel laser-assisted synthesis technique with 2D growth-controlling capabilities is introduced to resolve current issues in existing synthesis techniques discussed in Chapter 1. This new synthesis technique's process parameters and working mechanisms are discussed in great detail with extensive sets of experiments. In addition, the synthesis of four significant TMDCs, such as MoS_2, $MoSe_2$, WS_2, and WSe_2, have been demonstrated with widely accepted 2D materials characterization techniques.

In Chapter 3, The spatiotemporal control of the laser vaporization has established to unlock the time-resolved, sub-second, and ultra-fast growth of 2D crystal on the non-catalytic substrate such as Si/SiO_2 substrates with record-breaking growth rates. The time-resolved growth dynamics experimentation has been supported with precise temperature measurements at each experiment step.

In Chapter 4, a novel bottom-up synthesis strategy of LAST has been introduced where compositional inhomogeneities and concentration tunability have been demonstrated in a single step using energy and time-controlled laser vaporization of stoichiometric powder in the $MoSe_2$ growth processes. Vacancy tuning was comprehensively discussed with two different controllability of the LAST system. Various characterization techniques and algorithms have been used to identify the vacancy type and quantify the vacancy amount.

In Chapter 5, The key finding of this study is concisely discussed with concluding remarks.

CHAPTER 02

TWO-DIMENSIONAL QUANTUM MATERIALS SYNTHESIS BY A NOVEL LASER-ASSISTED SYNTHESIS TECHNIQUE (LAST)

2.1 Introduction

In the existing bottom-up gas phase synthesis, TMDCs mono and few-layers crystals growth are extremely challenging due to the complex and uncontrolled gas-phase reactions and flow dynamics. This chapter introduces a fast yet effective novel laser-assisted synthesis technique (LAST) that significantly reduces the challenges in the current gas-phase TMDC mono and few-layers crystals growth systems. In this new approach, the direct laser vaporization of stoichiometric powders (e.g., MoS_2 powder) is utilized to grow precisely controlled and high-quality 2D crystals (e.g., MoS_2) in an inert argon environment. Due to a very high vaporization temperature of stoichiometric TMDC powders (e.g., ~1400 ºC for MoS_2) compared to their growth temperature (e.g., ~850 ºC for MoS_2), the use of stoichiometric powders as the precursors in existing synthesis techniques not been employed. This approach's selective laser heating process allows efficient pressure-independent decoupling of the evaporation of precursors and crystal growth processes, which enables the growth of a large number of 2D materials directly from their stoichiometric powders, including the growth of high-quality 2D crystals of MoS_2, $MoSe_2$, WSe_2, and WS_2. This laser-based approach also offers rapid heating, evaporation, and growth as well as cooling and termination control in the system. This feature can be utilized for growing heterostructures with no cross contaminations by fast changing of the precursors. The crystal quality of MoS_2, WS_2, $MoSe_2$, and WSe_2 has been assessed by mainstream characterization techniques such as Raman spectroscopy, photoluminescence spectroscopy, Atomic force microscopy (AFM), scanning

tunneling electron microscopy (STEM) etc. The following sections discuss the detailed study of LAST's system and 2D crystal growth parameters.

2.2 System Design Flow

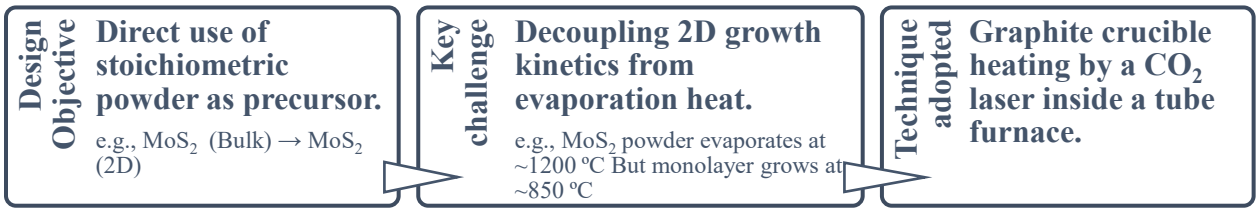

2.3 Experimental Setup

The key novelty of LAST is its ability to significantly reduce the existing growth complexities enabling accelerated synthesis and discovery of emerging 2D materials. Decoupling the growth from evaporation mechanisms in the LAST system allows the growth of monolayer 2D materials directly from the bulk stoichiometric 2D powders. In this approach, a laser beam is used as a precise and fast heating source for the evaporation of the stoichiometric powder in a highly controlled manner without disturbing the growth environment.

As shown in **Figure 2.1**, the LAST system consists of three main components, including a continuous wave CO_2 laser (10.6 µm wavelength) as an evaporation heating source that is coupled to the tube furnace via a zinc selenide (ZnSe) window, a custom-made graphite boat (1.2×0.7×0.7 cm^3) for absorbing and uniformly transferring the laser heat to the stoichiometric powder for vaporization,[125] a tube furnace with vacuum system used to create a suitable environment (i.e., pressure and temperature) for 2D materials growth. The substrate is positioned upside down right above the graphite boat to capture the vapor for the nucleation and growth process.

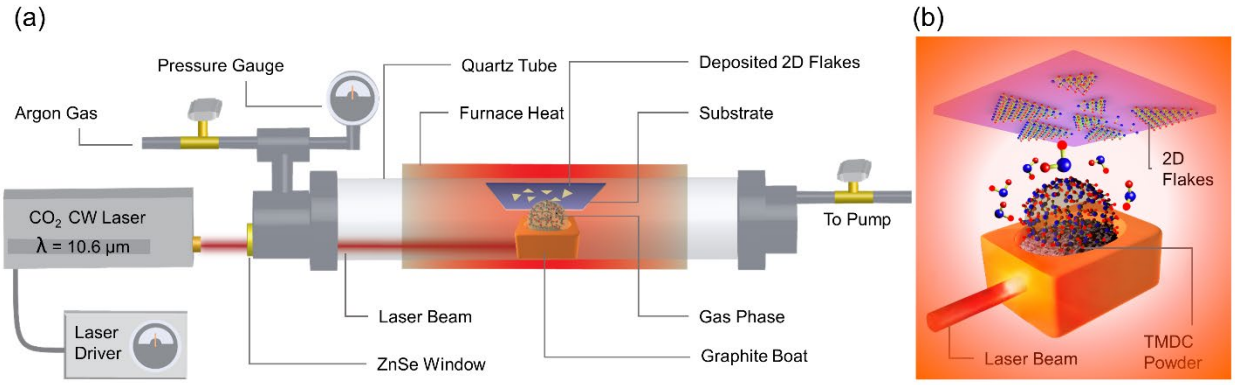

Figure 2.1 Schematic representation of LAST setup (a) with a close-up view (b) of the growth dynamics while laser heating a graphite boat containing the stoichiometric powders for vaporizing and subsequent growth of 2D layers on a Si/SiO_2 substrate. A tube furnace is used to create a suitable growth environment (i.e., temperature and pressure), while a laser is used for controlled heating and evaporation of stoichiometric powders. This apparatus allows the decoupling of growth from the evaporation mechanism enabling the direct use of stoichiometric 2D powders as precursors for the growth of high-quality monolayer 2D crystals.

2.4 LAST Process Parameters

Systematic experiments were performed under various times, laser power, pressure, and background temperature, as shown in **Figure 2.2a-c,** to decipher the nature of laser interaction with the graphite boat and the contribution of heat from the boat to the substrate. Due to the high infrared absorption efficiency of the graphite boat, its temperature increased within a few seconds after the laser irradiation. First, the decoupling mechanism was examined without tube furnace heat. **Figure 2.2a** (red line) shows the temperature of a graphite boat that ranges from 750 to 1150 ºC, corresponding to the laser irradiation powers ranging from 20 to 60 W, respectively. Then, for the same laser irradiation power, the substrate temperature was measured which was placed 6 mm above the graphite boat (**Figure 2.2a**, green line). The substrate temperature was in the range of

~500-650 ºC. This difference between the substrate and graphite temperatures facilitates the required decouple mechanism between the evaporation from growth effectively and precisely controls each process separately. These measurements suggested that although the boat temperature was sufficient for evaporating the stochiometric powders, the substrate temperature was still well below the 2D growth temperature, and another assisting heat source is required for the growth process, which is discussed further in the following paragraphs.

The heat contribution mechanism was confirmed by measuring the temperature at various argon background pressures. The heat coupling mechanism was found to be pressure-independent (further discussed in section 2.12). **Figure 2.2c** shows the temperature of a graphite boat and a substrate under various background pressures. It was apparent from the graph that pressure is not a significant factor in defining the boat and substrate temperature behaviors. This indicates the fact that convection heat from the boat to the substrate is negligible. Therefore, it can be concluded that the heat transfer is mainly due to radiation from the boat to the substrate. This feature of the system was remarkable since the pressure variable could now be considered a noninterfering parameter in the synthesis process because the pressure was not affecting the temperature change in the system. Thus, the pressure role in controlling the vapor flux and growth kinetics becomes much easier since it would not affect the synthesis environment, as discussed above.

It was clear from **Figure 2.2a** that besides the decoupling mechanism, it is also required to tune and maintain a suitable environment to enable the nucleation and growth of 2D materials on the substrates. A tube furnace has been utilized in addition to the laser irradiation source to tune the substrate temperature to control the growth kinetics. This feature enabled the system to precisely and selectively set the desired temperatures for the evaporation and growth of 2D materials. Thus, the LAST operation process is mainly an interplay between the laser heating of

the graphite boat and maintaining substrate temperature by tube furnace. As an example, considering a synthesis case in **Figure 2.2b**, when the tube furnace temperature was set at 750 ºC (dotted blue line), heating the boat with 30W laser irradiation power for 120 seconds resulted in the boat (red line) and substrate (green line) temperatures profile. The system achieved a saturation temperature of ~1100 ºC for the graphite boat and 825 ºC for the substrate, respectively, within 60 seconds.

These studies clearly show that the behavior of these two heat sources could not be described separately by a simple summation of boat and substrate temperatures. For example, at 750°C furnace temperature (dotted blue line, **Figure 2.2b**) and 30 W laser power combined, the Si/SiO_2 substrate and boat saturation temperatures were ~825°C and ~1100°C, respectively. In this case, the laser only contributed about 75 °C to the substrate temperature beyond the furnace. However, in a similar condition but without the background temperature (i.e., when the furnace was off), the laser contributed 275 °C to the Si/SiO_2 substrates (**Figure 2.2a**). Detailed experimental results for a large number of conditions are included in **section 2.13**. These studies revealed a coherent set of data on the nature of interactions between the CO_2 laser interaction, graphite boat, and the substrate that led to the successful synthesis of a large number of 2D materials.

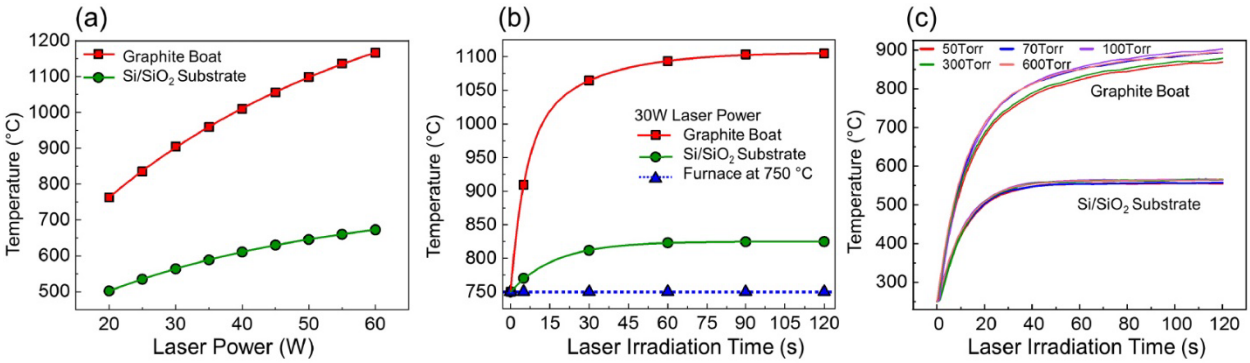

Figure 2.2 LAST system behavior. Boat and substrate temperatures as a function of laser power when the tube furnace is OFF showing a considerable temperature difference between the boat and the substrate, (a) A synthesis scenario at a specific laser power (30W) when the tube furnace is set to 750°C describes the temperature profile of boat and substrate as a function of time (b) The fitting lines are plotted to guide the eyes. Both (a) and (b) demonstrate the required decoupling mechanism to facilitate 2D growth. Boat and substrate temperature coupling as a function of pressure indicates a pressure-independent process (c).

2.5 Major 2D TMDC Synthesis Using LAST

The growth of various 2D TMDCs materials was tested employing the LAST decoupling mechanisms from their bulk stoichiometric powder. In this case, the growth of four primary TMDCs monolayer crystals, such as MoS_2, $MoSe_2$, WSe_2, and WS_2, has been successfully synthesized and demonstrated using LAST, as shown in **Figure 2.4**. First, the evaporation of these stochiometric TMDC powders has been studied using different laser energies by varying laser power and irradiation time, along with providing furnace temperatures such as 750 ºC, as shown in **Figure 2.3a**. Considering the effect of the heat transfer from the boat to the substrate during the vaporization of stochiometric powder, as discussed above, the furnace temperature was raised to the desired initial temperature for each 2D material so that the final temperature could reach the anticipated 2D growth temperature. Raising the furnace temperature to the growth level before applying the laser allowed the vapor flux to interact with the substrate at suitable growth temperatures. The threshold values for the laser power and furnace temperature are needed to initiate evaporation, and the growth of each material depends on its chemical composition. Therefore, the material systems can be classified as the growth conditions, as shown in **Figures 2.3a** and **b**, in terms of Sulfide/Selenide and Tungsten/ Molybdenum material systems.

Since stoichiometric powders were used to generate the precursor vapor, there was no need to introduce gasses, such as hydrogen, to reduce the growth environment. This excellent feature further simplified the growth process and eliminated hazardous gasses. The role of argon in the system was merely to adjust the background pressure for tuning the vapor flux and 2D growth from mono to multi-layers (Further discussed in **section 2.8**). **Figure 2.3a** and **b** describe the evaporation and growth conditions for the reported four TMDC materials. In these experiments, the graphite boat dimensions (1.2×0.7×0.7 cm^3) with 0.7mm thickness and the weight of precursor powders (10 mg) were kept the same for all the experiments. Laser irradiance time is referred to as crystal growth time, and after turning off the laser, the system cooled to room temperature by natural cooling, as shown in **Figure 2.3c**. Silicon substrate with 250 nm of thermal oxides was used as the growth substrate and was placed upside-down about 6 mm above the graphite boat for all the materials synthesis experiments.

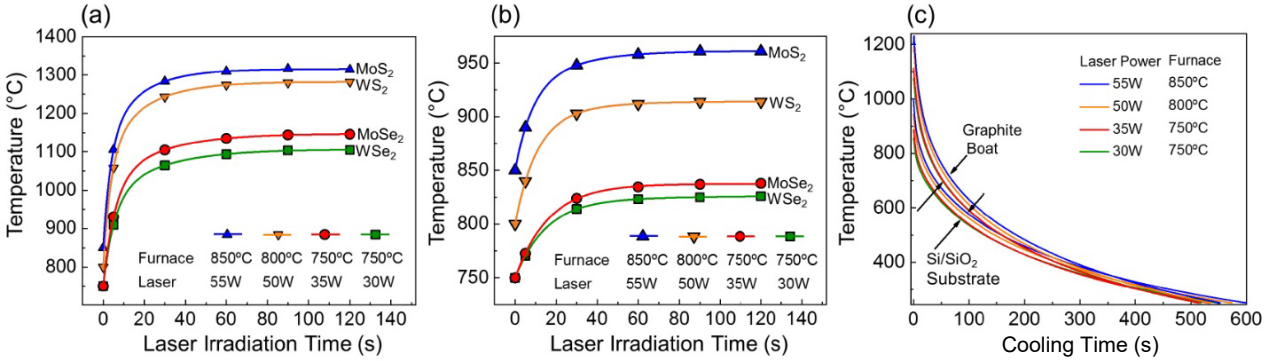

Figure 2.3 The laser irradiation time effect on evaporation and growth. The optimized evaporation (a) and growth (b) temperatures for MoS_2, $MoSe_2$, WSe_2, and WS_2 at indicated laser powers and irradiation times. The trend of evaporation and growth profiles match with the bonding length and energy of the MX_2 systems – i.e., MoS_2 requires the most laser power and heat while WSe_2 needs the least. The natural cooling time profiles (c) follow exponential decay as indicated in the graph.

For the selenide system (i.e., WSe_2 and $MoSe_2$), the low laser powers (20-30 W) were sufficient to create vapor, and moderate furnace temperatures (~650-750 ºC) were required to form a few micron size monolayer triangular crystals on the substrates. The optimized growth parameters for large monolayer crystals were achieved quickly after a few trial-and-error. For instance, large monolayer WSe_2 single crystals (~10-100 μm in size) were successfully synthesized using 30-watt laser power with 120-second laser irradiance time at 750 ºC furnace temperature and 300 Torr background pressure (**Figure 2.4e**). These optimized parameters translated to boat and substrate temperatures of 1100 ºC and 825 ºC, respectively, as can be seen in **Figures 2.3a** and **b**. A typical 2D monolayer formed by LAST is shown in **Figure 2.4a,** while **Figure 2.4c-f** shows the grown monolayer single crystal for each material. The growth optimization and correlation of process parameters to the layer formation are described in **section 2.8**. The WSe_2 synthesis results set a guideline for the growth of analogous $MoSe_2$ crystals.

Interestingly, the required laser power for evaporation increased to about ~35W while keeping other parameters constant. Consequently, the boat and substrate temperatures were about 1150 and 870 ºC, respectively, slightly higher than that of WSe_2 crystals. The increases in laser power and temperatures can be attributed to the chemical structures of those materials – i.e., Mo-Se has a shorter bond length and higher bonding energy than W-Se. This initial experimental data helps to reduce the trial-and-error experimentation for synthesizing a material with unknown synthesis parameters. The origin of this predictability was imminent from the precursor's simplicity and utilizing a graphite boat as a crucible in the system. The primary purpose of choosing the graphite boat as a crucible was its efficiency in absorbing laser power and uniformly transferring heat to the stoichiometric powders. Additionally, it develops coherent statistics of synthesis data for many materials, which can be used for predicting new materials' growth

parameters. These unique features enabled the synthesis of other 2D materials by employing the developed growth curves (**section 2.13**) and extracting the potential laser powers and substrate temperatures. For example, the sulfide systems (MoS_2 and WS_2) required relatively higher laser power and furnace temperatures than selenide systems ($MoSe_2$ and WSe_2), as shown in **Figure 2.3a** and **b** due to the shorter bond length and stronger bonding energies in the sulfide systems. The growth of large WS_2 crystals requires about 50W laser power, 120 seconds of irradiation time, and 800 °C background temperature at 300 Torr background pressure. This parameter corresponds to the boat temperature of 1250 ºC and the substrate temperature of 925 ºC. MoS_2 followed the same trends in the selenide system, requiring relatively more significant laser power. MoS_2 required 55W laser power at 120 second irradiation time and 850 °C furnace temperature corresponding to the boat temperature of 1300 ºC and the substrate temperature of about 950 ºC during the growth. These experiments also show that larger crystals (~100 μm) can be achieved by slowly ramping the laser power from an evaporation threshold to higher values during the growth (explained in section 2.9).

2.6 Characterization of Synthesized Crystals by LAST

Widely used two-dimensional materials characterization methods such as optical imaging, atomic force microscopy (AFM), transmission electron microscopy (TEM), as well as Raman and photoluminescence (PL) mapping and spectroscopy measurements were utilized to evaluate the size, the number of layers, and quality of the grown crystals. Depending on optimization, LAST produces few-layer to monolayer crystals. However, all the characterization discussion is limited to monolayer crystals, while multi-layer crystal formation dynamics have been discussed in section 2.8.

2.6.1 Optical and Atomic Force Microscopy

Figure 2.4a-f shows the optical and AFM images of typical monolayer 2D crystals, including MoS_2, $MoSe_2$, WSe_2, and WS_2 grown on Si substrates with 250 nm SiO_2 layer. The image contrast shows that most crystals were monolayer in the abovementioned conditions. The crystal's AFM measurement results showed about ~0.7nm height profile (**Figure 2.4g),** confirming their monolayer thicknesses.[115,126]

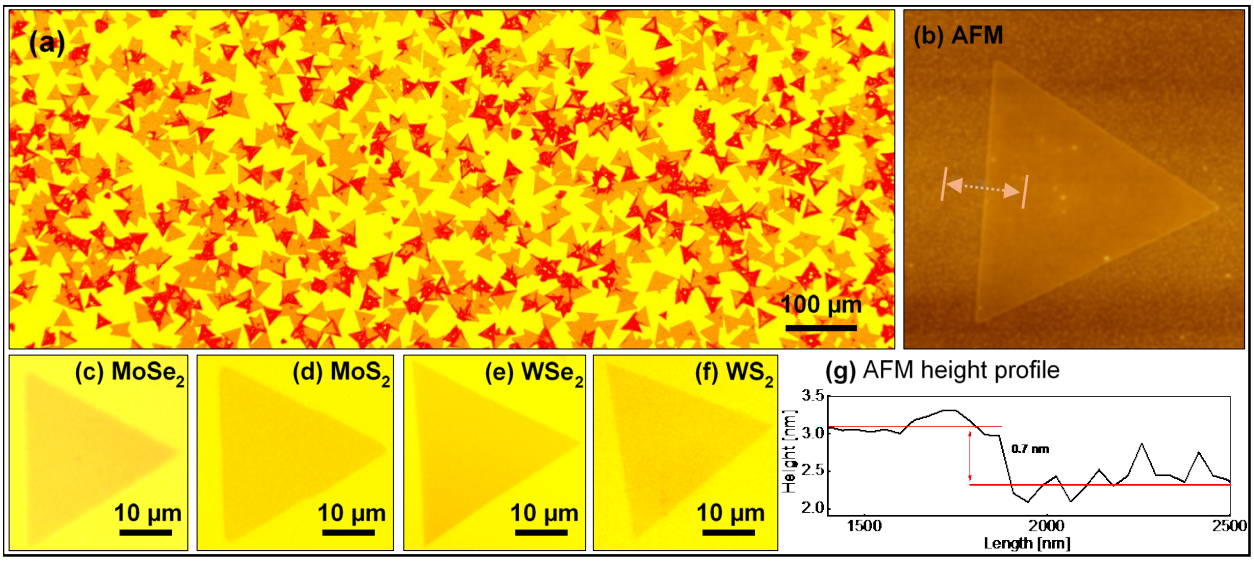

Figure 2.4 Optical images of the typical monolayer crystals materials grown by LAST show the crystals' growth density, morphology, and size (a). Optical images of monolayer $MoSe_2$ (c), MoS_2 (d), WSe_2 (e), and WS_2 (f). The optical contrast indicates that the crystals are mainly monolayers. An AFM image (b) and the measured height profile (g) confirm the thickness (~0.7 nm) of a monolayer crystal.

2.6.2 Raman and PL Spectroscopy

Raman and PL spectroscopy are essential characterization techniques in the field of layered materials[127], which provide valuable information about the identity and quality of the layered 2D crystals. For instance, Raman spectroscopy provides structural fingerprints, including the number

of layers, stacking order, and defects information based on the frequency, width, and amplitude of the vibrational modes of the crystals[128]. Typically, the Raman spectrum of bulk trigonal prismatic TMDCs exhibits three active signals at high frequencies, including E^1_g, E^1_{2g}, and A^1_g, where the E^1_g and E^1_{2g} are in-plane modes, and the A^1_g is an out-of-plane mode[129]. On the other hand, all TMDCs transition from indirect materials in the bulk form to direct bandgap when becoming monolayer[130]. Therefore, the PL emissions are more intense in monolayer crystals and decrease significantly by adding layers.[131, 132]

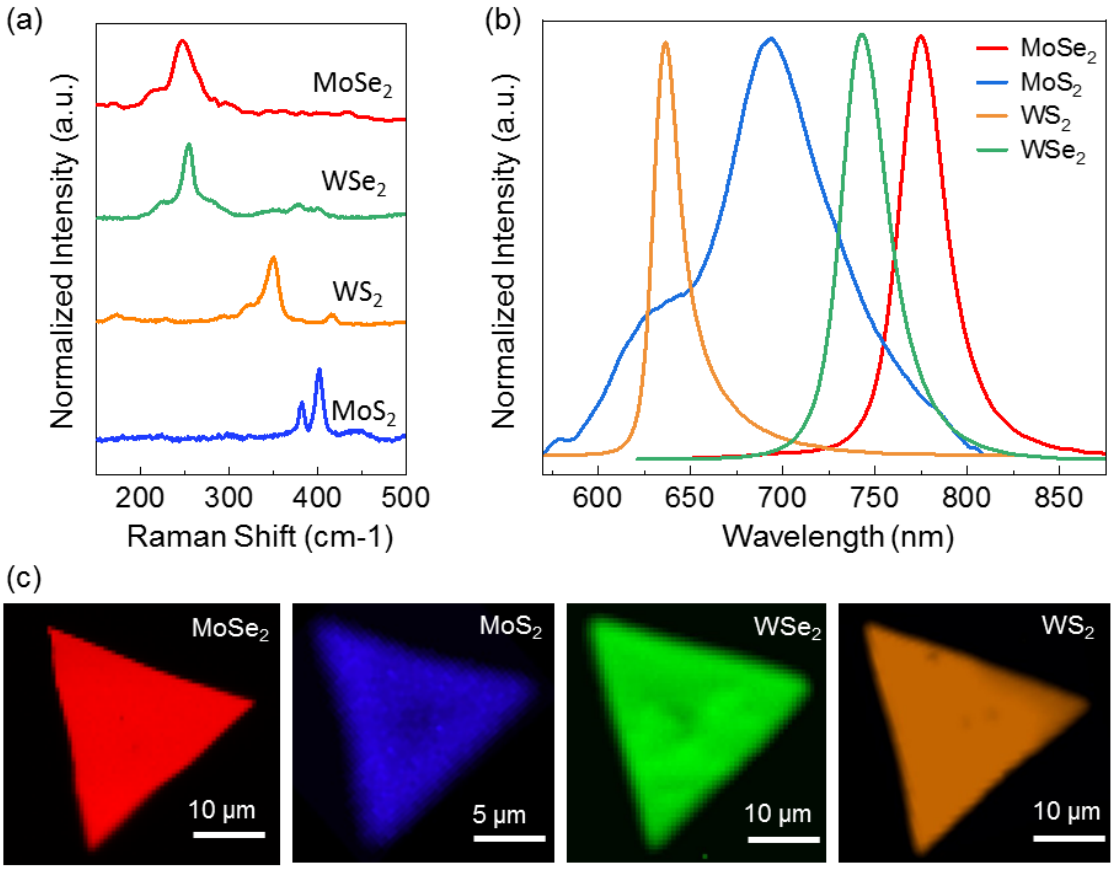

Figure 2.5 Optical spectroscopy and mapping of the single layer $MoSe_2$ (red line), WSe_2 (green line), WS_2 (orange line), and MoS_2 (blue line) crystals under 532 nm laser excitation source. Raman (a) and PL (b) spectra show the peak location of each material matching the reported values

in the literature. [61, 64, 67, 128, 133-137] The PL maps (c) of the monolayer crystals, as labeled, show the overall uniformity of the grown crystals.

Figure 2.5a and **5b** show the Raman and PL spectra collected from single-layer $MoSe_2$ (red line), WSe_2 (green line), WS_2 (orange line), and MoS_2 (blue line) crystals. Raman and PL spectroscopy is performed at room temperature using a 532nm laser as an excitation source with intensity below 200 μW for a <1μm diameter spot size. These specs were selected to prevent sample damage during the measurements. For $MoSe_2$, the Raman characteristics vibration mode A^1_g is found at ~240 cm^{-1}.[128] The Raman peak around 353 cm^{-1} associated with an interlayer interaction was not observed, suggesting this $MoSe_2$ film is indeed a single layer, which was further confirmed from its strong PL emission at ~790 nm (**Figure 2.5b**). The Raman active modes of WSe_2 crystals, including E^1_{2g} at ~236 cm^{-1} and A^1_g at ~251 cm^{-1} (**Figure 2.5a**), were observed, and its PL emission was centered at ~750 nm (**Figure 2.5b**). [128, 133-135] In the case of WS_2 Monolayers, Raman spectra showed E^1_{2g} and A^1_g phonon modes at ~346 cm^{-1} and ~409 cm^{-1} (**Figure 2.5a**) while PL peak was centered at ~640 nm (**Figure 2.5b**). [64, 136] Finally, MoS_2 monolayers showed two representatives Raman active modes, including E^1_{2g} at ~378 cm^{-1} and A^1_g at ~403 cm^{-1} (**Figure 2.5a**) along with PL at 690 nm. [61, 67, 137] In general, the characteristics of Raman vibration modes and PL spectra for all four monolayers were in accordance with reported literature similar to the exfoliation and conventional CVD-grown methods. Further, the PL mapping of the synthesized crystals was performed to monitor the uniformity of the grown crystal (**Figure 2.5c**).

2.6.3 Atomistic Analysis

To obtain atomistic insight into the quality, stoichiometry, and defect density of the synthesized monolayers in this method, the crystal structure of WSe_2, WS_2, $MoSe_2$, and MoS_2 monolayers were characterized by atomic resolution ADF-STEM imaging, which is capable

of identifying individual atoms, or the total mass of atoms within columns, via the image intensity contrast as shown in **Figures 2.6a-p**. The STEM images confirm the single-crystalline nature of the monolayers, while the fast Fourier transform (FFT) of those images (**Figure 2.6b,f,j,n**) also confirms the hexagonal symmetry of the obtained monolayer crystals. These LAST-grown samples have not shown significant vacancies, defects, or doping levels while characterizing various monolayers with different techniques. The lattice fringes of WSe_2, WS_2, $MoSe_2$, and MoS_2 in the STEM images show hexagonal crystal structures with a lattice constant, *a,* of 3.3 Å, 3.15Å, 3.16 Å, and 3.28 Å respectively similar to the reported values. By carefully analyzing the line profiles (**Figure 2.6d,h,l,p**) of the atoms in the STEM images (**Figure 2.6c,g,k,o**) for each material respectively, confirm their stoichiometry close to 1:2 ratio of the transition metal to chalcogenide atoms.

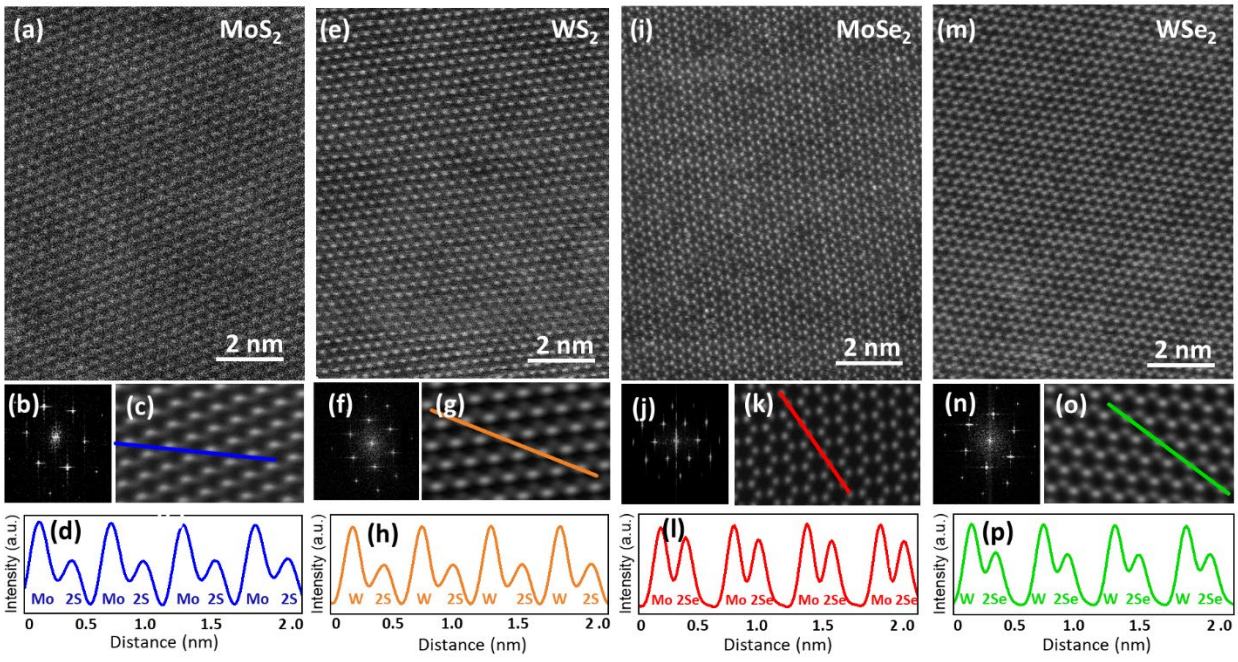

Figure 2.6 STEM characterization of LAST-grown materials. **Figures a, e, i, m** show the actual TEM image of WSe_2, WS_2, $MoSe_2$, and MoS_2 monolayers, respectively. **Figures b, f, j, n** represents the FFT of each crystal. **Figures c, g, k o** shows an enlarged and filtered version of the

original TEM image of each crystal. **Figures d, h, l, and p** illustrate the line profile of the synthesized crystal, which is a direct representation of the stoichiometry of the grown materials.

2.7 LAST and Other Existing Synthesis Techniques

Since LAST is a new synthesis technique for synthesizing 2D semiconducting quantum materials, it is logical to draw a comparative discussion with other existing synthesis techniques in the current literature. The comparative discussion, such as System/Method, Materials, Size, Layer number, Ref. [138, 139 63, 75, 81-83, 140-144], as shown in **Table 2.1.** The comparison between LAST and PLD is also discussed in **section 2.7.1** to clarify their differences.

Table 2.1 TMDCs Synthesis Methods

Method	Precursor	Domain Size	Thickness	Growth time	Impurity	Ref
CVD	Metal Oxides & Chalcogenides[138, 139]	Tens of microns[138, 140]	Mono to few-layer crystals[138, 139]	minutes[83]	Moderate[140]	138, 139 83, 140
MOCVD	Metal-organic compounds[141, 142]	Few micron[141, 142]	Mono to few-layer crystals[141, 142]	Tens of minutes to hours[142]	High[82]	82, 141, 142
MBE	Elemental[82]	Tens of Nanometers[143, 144]	Mono to few-layer crystals[53]	Hours	Low[81]	81, 82, 143, 144
PLD	Stoichiometric target[63, 75]	Few to tens nanometers[140]	Mono to few-layer films[25]	Seconds to minutes[25]	Low[140]	63, 75, 140
LAST	Stoichiometric Powder	Tens of microns	Mono to few-layer crystals	Sub-seconds to minutes	Low	

2.7.1 Differences Between LAST and PLD

The LAST and PLD are different based on the nature of their synthesis mechanisms. PLD is a nonequilibrium ablation process at short time scales (typically within nanoseconds),[145, 146],

while LAST is a thermal vaporization process with much longer time scales (seconds). Typically, the PLD (using a high-energy pulsed laser such as an excimer laser) involves the generation of a laser plasma consisting of high kinetic-energy ions and neutral atoms, followed by slower-moving molecules and clusters. The high nonequilibrium PLD process in a vacuum environment can produce fast ions and neutrals with sufficiently high kinetic energies (> 100 eV) to form thin films with nanodomains. However, typically background gases (tens of milliTorr) moderate the kinetic energies to ~ 1 eV, leading to the formation of nanoparticles and deposition of rough films[147].

In contrast, the LAST uses a continuous laser beam (a CO_2 laser in this case) to heat a graphite crucible containing the stoichiometric 2D powder and vaporize the material. This vapor contains molecular species with very low kinetic energies, similar to the CVD environment. The vapor species slowly nucleate on the substrate and grow into larger single-crystalline domains.

2.8 Layer Formation Dynamics

The demonstrated results are the optimized experimental parameters resulting in the formation of monolayer crystals due to the high interest in monolayer TMDCs for electronic and optoelectronic applications. This section discusses the effect of process parameters away from the optimized monolayer growth conditions.

The control over the layer number mainly depended on the interplay between the growth pressure, temperature, source amount, vaporization laser power, laser irradiation time, and distance between the substrate and the source. These parameters control the precursor flux and their diffusion rate on the substrate, which define the crystal growth dynamics. The physical process parameters, such as the precursor source amount (10 mg) and the distance between the substrate to the source (6 mm), were kept constant throughout the study to simplify the growth parameters. Therefore, pressure and temperatures were employed in tuning the layer numbers in this work.

Before controlling the growth of the multi-layer crystal, the system first calibrates to the monolayer crystal growth parameters, then pressure and temperature constrain are employed for different layer formations.

Generally, from monolayer growth parameters, increasing the background pressure at a constant temperature starts adding layers to the crystals. This addition of layers was due to the contraction and expansion of the vapor plume by increasing and decreasing the pressure, respectively. Such confinement of the vapor into smaller volumes resulted in an increased flux and the formation of thicker layers than their relatively lower-pressure conditions. On the other hand, by decreasing the temperature at constant pressure, the formation of multi-layer crystals was also observed, possibly due to the reduced lateral diffusion of the precursor species on the substrate and the top of an existing crystal resulting in the nucleation and formation of subsequent layers.

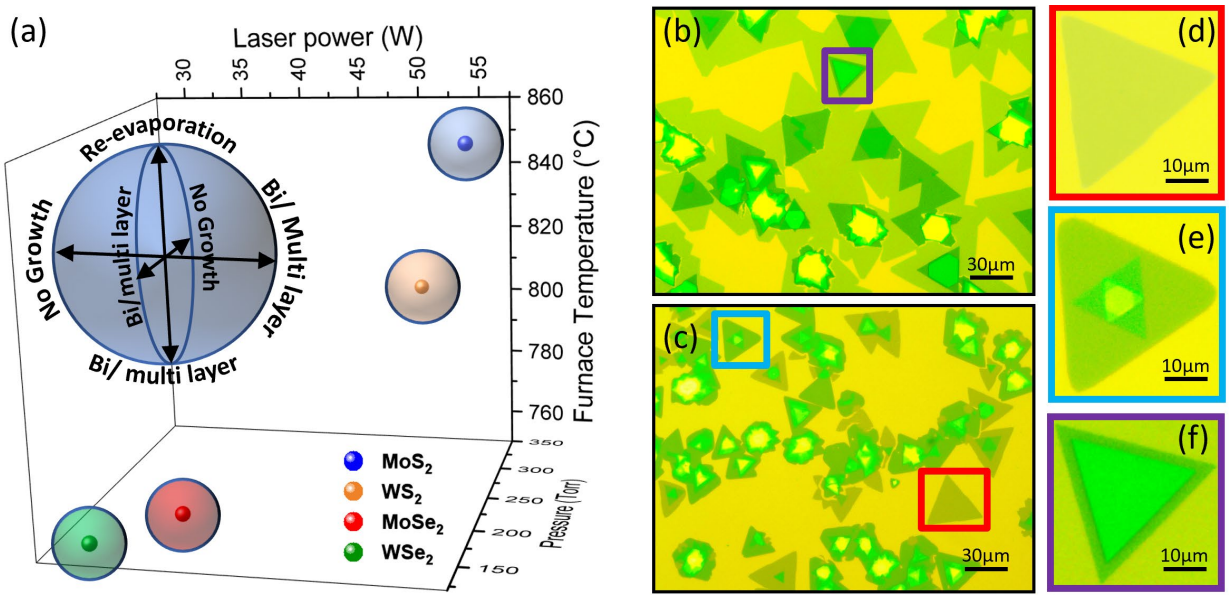

Figure 2.7 Multi-layer growth of 2D materials. The optimized conditions for monolayer growth for MoS_2, WS_2, $MoSe_2$, and WSe_2 are represented with the solid blue, orange, red, and green dots, respectively (a). Assuming the growth process parameters as a sphere, the sphere's center

represents the optimum growth parameters. Deviation from the center results in the formation of bi/multi-layers, re-evaporation, and burning, or no growths as graphically indicated on the enlarged blue sphere. Optical images show the growth of mainly multi-layer MoS_2 crystals (b) and (c). These multi-layer growth conditions are similar to monolayer conditions except for their growth temperature, which is reduced by 50^{o}C. In these two optical images, three different types of layer formation are marked by red, green, and violet windows. Figures (d), (e), and (f) are enlarged pictures of the indicated zones.

Figure 2.7 (a) shows the experimentally derived optimized pressure, temperature, and laser power conditions for forming monolayer 2D material as represented by the solid dots (blue, orange, red, and green dots for MoS_2, WS_2, $MoSe_2$, and WSe_2, respectively). The diffused sphere around the central dots represents a bi/multi-layer formation zone along with other possibilities such as re-evaporation and no growth depending on deviation direction from the optimized point. For example, the enlarged version of the blue dot (MoS_2) shows how changes in the laser power, pressure, or temperature result in bi/multi-layer, re-evaporation, and no growth. **Figure 2.7 b-f** shows an example of multi-layer MoS_2 growth by this method. For instance, by reducing the furnace temperature in a condition where mainly monolayer crystals growth happens, by decreasing 50^{o}C, the growth of multi-layer MoS_2 crystals is observed, as shown in **Figure 2.7**. Alternatively, increasing the pressure by 100 Torr resulted in the same effect. Laser irradiation power and distance between the substrate and graphite crucible are essential factors in tuning the layer thickness. Changing the distance or laser power requires finding a new set of background temperatures and pressure to achieve mono and multi-layer crystals.

2.9 Larger Crystals Growth Technique

After obtaining the initial process parameter such as laser power, furnace temperature, laser irradiation time, and pressure for the growth of high-quality monolayer crystals, this optimization study focused on forming larger crystals.

In this optimization process, the primary purpose was to reduce the nucleation density and grow them as large as possible before merging and forming grain boundaries. Experiments show that ramping laser power from low to high during growth can help achieve larger crystals. For example, **Figure 2.8 a, b** shows a two-stage ramping process during the growth of WS_2 crystals resulting in flakes as large as 100 microns.

The ramping assists the growth by creating less flux and donating less temperature to the substrate at the initial nucleation and growth process, which might reduce nucleation density. The further ramping adds more flux and heat to the system, allowing the already-formed nuclei to grow larger. Although this approach seems very promising for the growth of larger crystals, further experiments will be required to optimize and understand the growth mechanism fully.

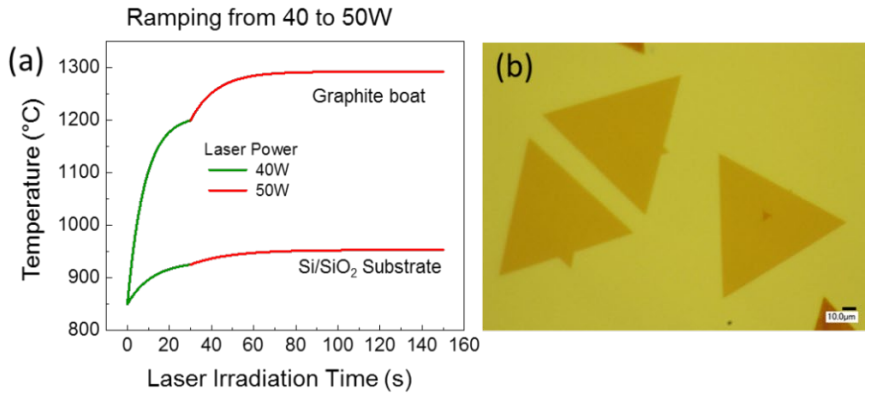

Figure 2.8 Growth of larger crystals by ramping laser power. Evaporation and growth graph (a) shows how the ramping of laser power from 40 W (green) to 50 W (red) resulted in the growth of large (~100 um) WSe_2 crystals (b).

2.10 Stoichiometry in Synthesized 2D Crystals

More experiments were also performed to find conditions where a non-stoichiometric crystal can form. According to our observation, the lack of stoichiometry was observed at low background pressures, mainly in the $MoSe_2$ case. When the background pressure was reduced (<100 Torr), the Raman fingerprints deviated from the stoichiometric crystals. However, as the pressure was increased, the vapor plume became smaller, and Raman signatures were recovered to stoichiometric fingerprints. The $MoSe_2$ central Raman peak at ~240 cm^{-1} split into two peaks at ~225 and 250 $cm^{-1,}$ which is previously related to a large amount of selenium vacancy in the crystal.[148] It assumed that the lack of stoichiometry at lower pressure is due to evaporation and the escape of chalcogen atoms from the vapor. Higher pressures confined the vapor plume, preventing the chalcogen atom losses during the growth process. However, it should note that this effect was not as noticeable for the other 2D materials reported (MoS_2, WS_2, WSe_2) in this work, and they mainly showed stoichiometric crystal signatures. **Chapter 4** elaborates further on growing crystals with different vacancy levels.

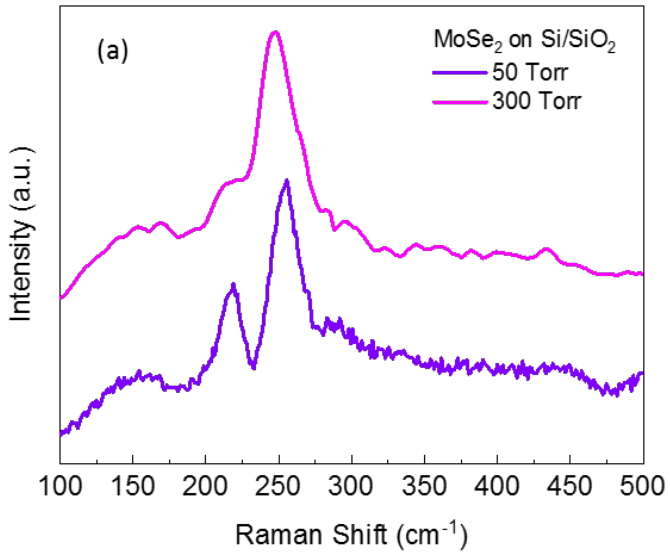

Figure 2.9 Raman spectra of $MoSe_2$ synthesized at 50 and 300 Torr background pressures (a). At low pressure, the prominent Raman peak at ~241 cm^{-1} split into two peaks at ~225 and 250 cm^{-1} related to selenium vacancy, as previously reported.[3]

Further optical characterization has been performed on the powders and the synthesized flakes to understand their correlation. The Raman characterization results obtained from our synthesized crystals showed signatures similar to the reported theoretical and experimental works.[149, 150] (**Figure 2.10**) A tabulated powder source information is included in **section 2.11**.

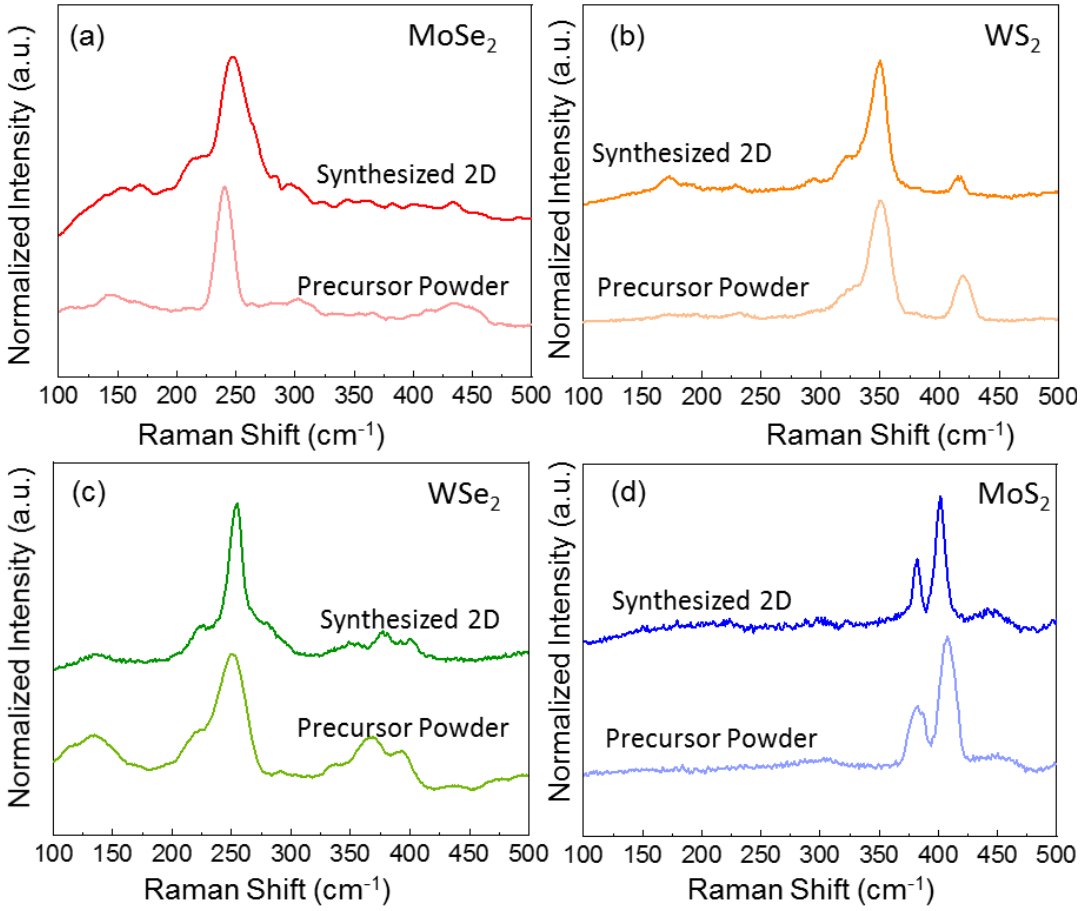

Figure 2.10 Raman spectroscopy comparison between the as-synthesized $MoSe_2$ (a), WS_2 (b), WSe_2 (c), and MoS_2 (d) 2D crystals and their respective precursor powders as labeled.

2.11 Precursor Details

Precursor materials used in this study were purchased from **Alfa Aesar** from Thermo Fisher Scientific. The specifications are tabulated in the following table.

Table 2.2 Precursors used to synthesize monolayer crystals by LAST.

	Molybdenum (IV) sulfide	Molybdenum (IV) selenide	Tungsten (IV) sulfide	Tungsten (IV) selenide
Product Number	41827	13112	11829	13084
Molecular formula	MoS_2	$MoSe_2$	WS_2	WSe_2
Molecular weight	160.08	253.87	247.98	341.77
Purity	99%	99.9%	99.8%	99.8%

2.12 System Pressure Study

System pressure is a critical issue for a synthesis method since pressure is a crucial parameter for any synthesis method. System pressure mainly determines the crystal growth dynamics. For the LAST system, it is critical to know the impact of pressure, while the graphite boat receives heat from the laser and the substrate receives heat from the graphite boat. In other words, to build a clear understanding of the convection heat coupling mechanism between the graphite boat and the Si/SiO_2 substrate (**Figure 2.11).**

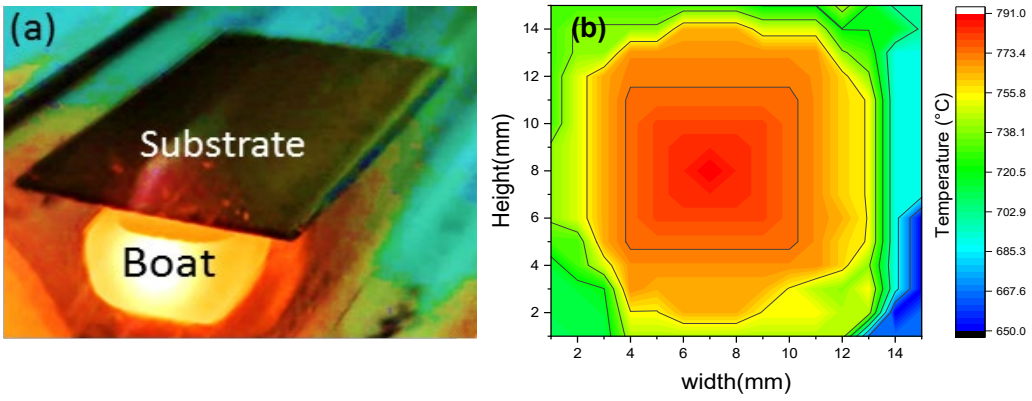

Figure 2.11 An optical image (a) showing the graphite boat and substrate locations. A CO_2 laser heated the graphite boat, and the silicon substrate was placed upside down about 6 mm above the graphite boat. The substrate heat map (b) is constructed from a matrix of data points of different locations.

Figure 2.12 shows the temperature of the boat as a function of various laser power at different background pressures. The laser power was tuned from 20W to 60W with 5W increments while the background pressures varied to 50Torr, 70 Torr, 100 Torr, 300 Torr, and 600 Torr. In this process, for each background pressure, the temperature increased exponentially in the first 20 seconds and saturated at a specific temperature depending on the laser power. This rise time was similar for all the laser powers. The saturation temperatures varied from 700 °C at 20W to 1150 °C at 60W laser powers with no substantial pressure effect on the boat temperatures.

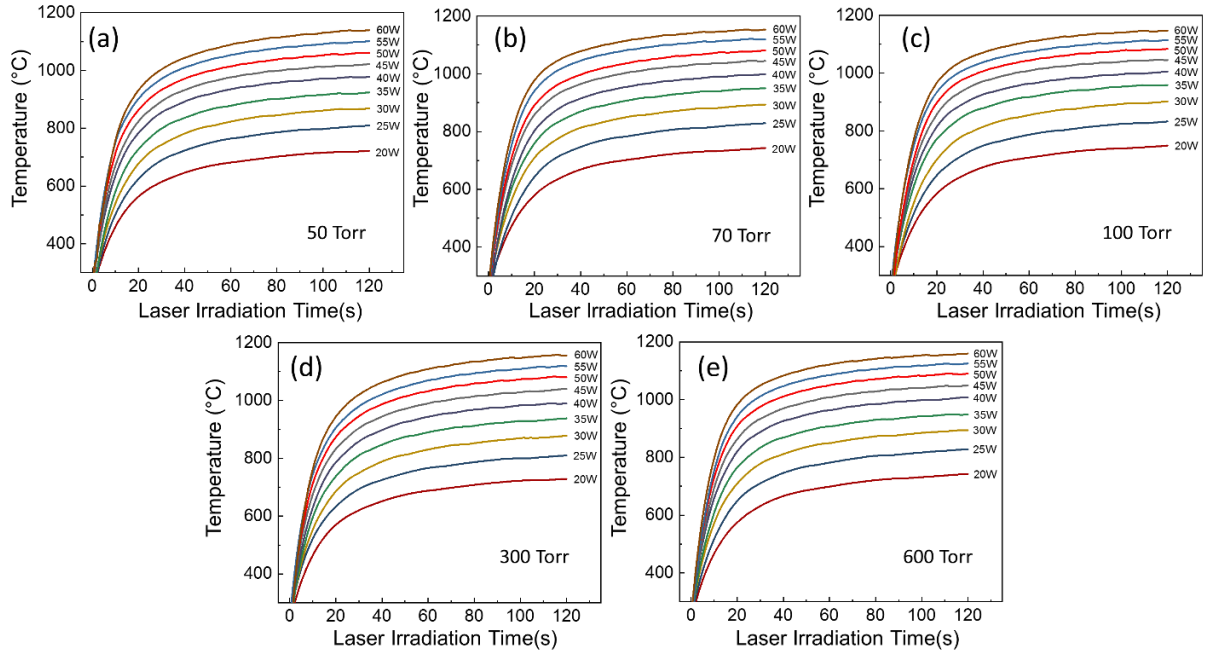

Figure 2.12 Measured graphite boat temperature as a function of different laser power (20-60W) at 50 Torr (a), 70 Torr (b), 100 Torr (c), 300 Torr (d), and 600 Torr (e) pressure, respectively, when the tube furnace was off.

Next, the Si/SiO_2 substrate temperature was measured on the same experimental setup to observe the heat transfer mechanism from the graphite boat to the substrate (**Figure 2.13**) from a 6 mm distance (**Figure 2.11a**). The pyrometer emissivity was set to 71% for Si/SiO_2 substrate temperature measurements.[151,152] The pyrometer measuring spot was placed slightly away from the center to eliminate the contribution of boat radiation through the silicon at low temperatures. The substrate had about 50 °C variations in the temperature from the center to the edge, as shown in the temperature distribution profile in **Figure 2.11b.** According to these experiments, the temperature profiles show a similar trend as the graphite boat, i.e., the exponential increase in the beginning and saturation at a later time. The saturation temperature varied from 450 °C at 20 W to 650 °C at 60W laser power. The pressure variation has shown a minimal effect on the heat transfer from the boat to the substrate, which has been discussed further in more detail.

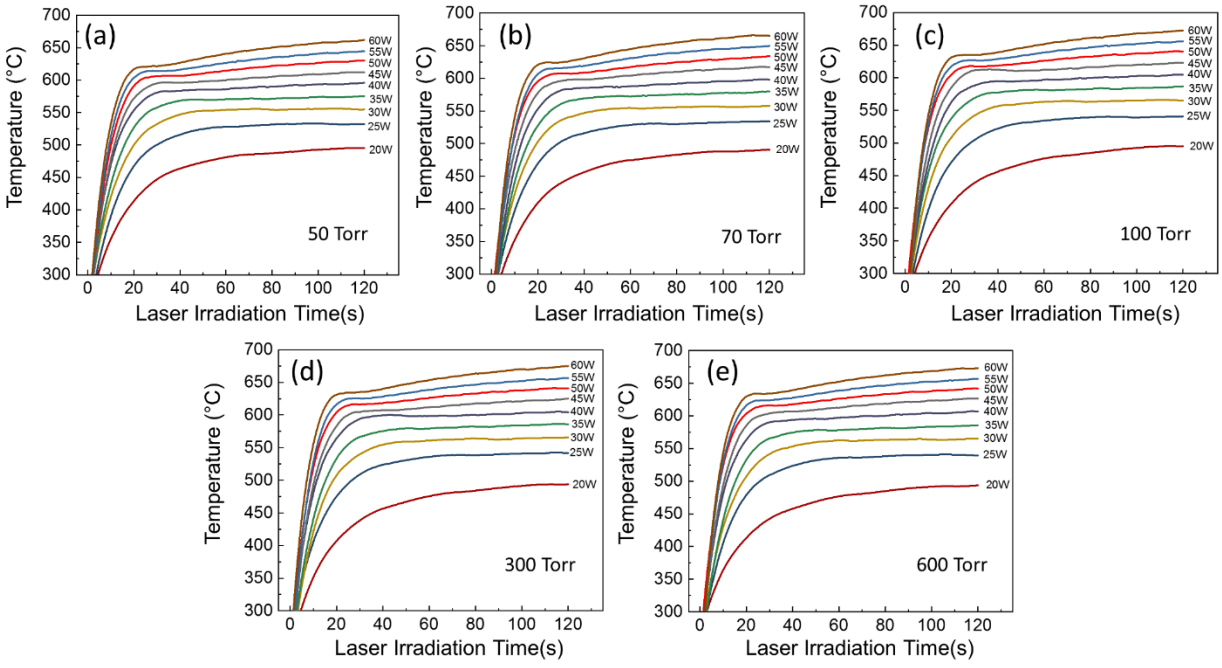

Figure 2.13 Substrate temperature as a function of different laser power (20-60W) at 50 Torr (a), 70 Torr (b), 100 Torr (c), 300 Torr (d), and 600 Torr (e), respectively, when the tube furnace was off.

Overlapping **Figure 2.12** and **Figure 2.13** for all the pressure cases, **Figure 2.14 a** and **b** are created, and this pressure does not affect the heat transfer from the graphite boat to the substrate, which confirms the pressure-independent response of the system. This feature was remarkable since one of the primary variables did not disturb the evaporation and growth temperatures allowing us to freely choose a working pressure suitable for the growth conditions, as the pressure was still effective in confining the vapor flux.

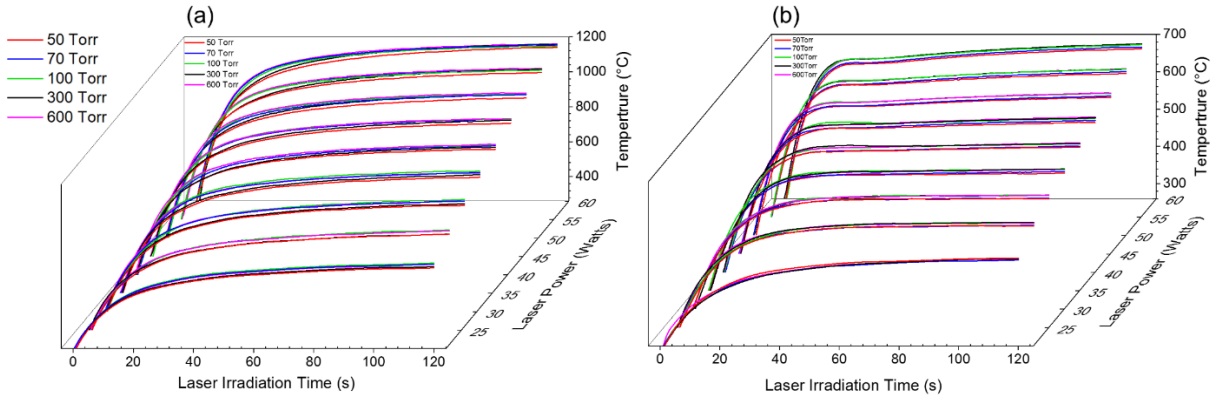

Figure 2.14 Pressure-invariant temperature response of the system. The superimposed 3D graphs from Figures S2 and S3 show the temperatures of the graphite boat (a) and the substrate (b) in response to various pressures.

2.13 Growth Curves

The substrate and graphite boat temperature plays a crucial role in the crystal growth dynamics. The graphite boat's and substrate's temperature has been measured at different crystal growth conditions to evaluate the crystal's growth dynamics. The measurements of temperatures were obtained by quickly opening and closing the furnace door. The built-in internal thermocouple shows that the system retains the internal condition if the brief interval of opening and closing time of the furnace door is kept within 3 seconds. First, the graphite boat temperature was measured for the background temperatures of 600, 650, 700, 750, 800, and 850 °C by keeping the pressure at

300 Torr using the same laser power interval (20 to 60W). A similar procedure was repeated to measure the temperature of the Si/SiO_2 substrate. In this experiment, it was observed that the interaction of the laser heating and tube furnace heating sources was not simply the sum of both. For example, the graphite boat saturation temperature for 60W laser power without tube furnace heat is 1100 °C while it is 1325 °C with 850 °C tube furnace heat for the same laser power. This means 850 °C tube furnace temperature only contributed 225°C to the graphite boat. The saturation trends were similar to the previous condition when the furnace was off. The substrate temperature behavior was similar to the graphite boat condition. For example, the substrate saturation temperature for 60W laser power without the furnace heat was around 650 °C. Still, it increased to 960 °C with an 850 °C background temperature for the same laser power. This indicated that the 850 °C background temperature only donated about 310°C to the substrate.

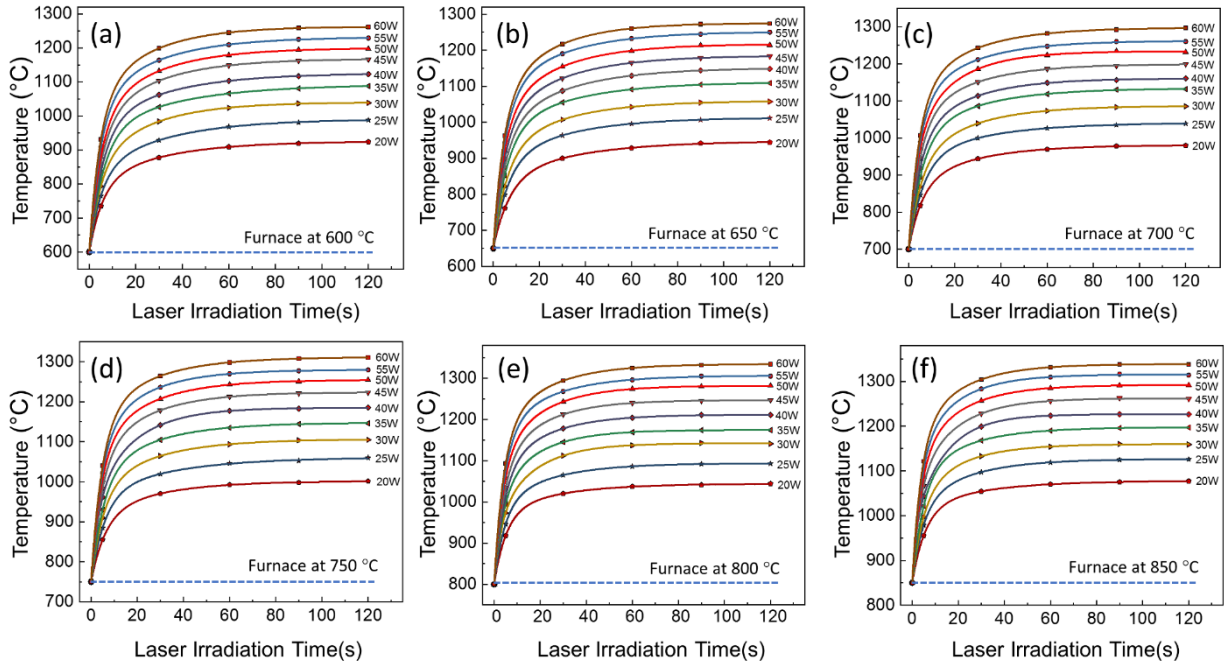

Figure 2.15 Graphite boat temperature as a function of different laser power (20-60W) at 300Torr when the tube furnace was set to 600, 650, 700, 750, 800, and 850 °C, respectively.

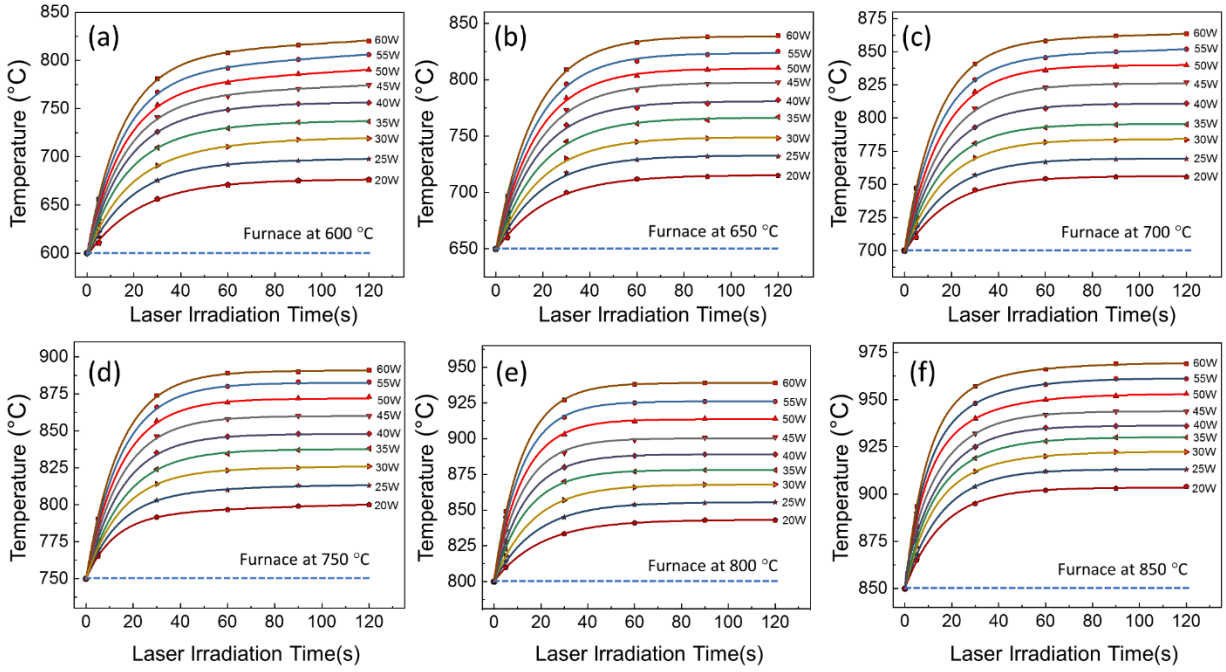

Figure 2.16 Substrate temperature as a function of different laser power (20-60W) and at 300 Torr when the tube furnace was set to 600, 650, 700, 750, 800, and 850 °C.

Overall, these graphs are crucial to selecting the growth environment of targeted 2D materials depending on their thermodynamic properties. The high temperature is critical to growing larger flakes in many cases due to the increased diffusion rate. However, high temperature can also re-evaporate already-developed flakes. As a result, it is critical to select a growth temperature between re-evaporation and optimal diffusion window.

2.14 Cooling Behaviour of LAST

The termination and cooling behavior of the system were relatively straightforward. The termination process starts with turning off the laser and immediately opening the furnace door to room temperature. This setting lets the graphite boat and substrate cool down naturally to room temperature. Graphite and silicon needed almost 2.5 minutes to cool down to 250°C, as shown in **Figure 2.17**(a) and (b), respectively, while the tube furnace kept off during the laser irradiation.

Figure 2.17(c) shows the tube furnace, graphite boat, and substrate combined cooling profile of specific laser power (30W,35W,50W, and 55W), which required 10 minutes to cool down to 250°C.

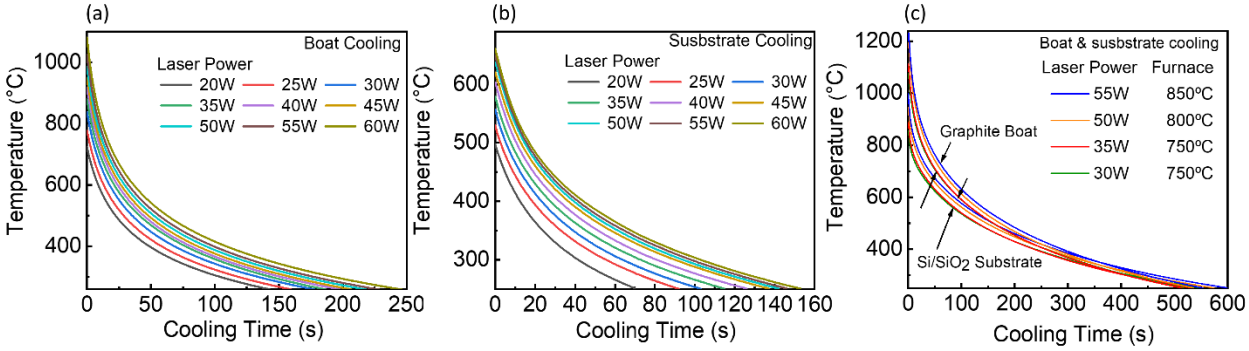

Figure 2.17 Cooling profiles of the graphite boat (a) and substrate (b) for various laser powers while the furnace was off during the laser irradiation. (c) Graphite and substrate cooling profiles while the furnace was at different temperatures during the laser irradiation.

2.15 Experimental Methods

2.15.1 Growth Process

Silicon substrates with 250 nm thermally grown oxide were used as the substrates for all the experimenters. These substrates were cleaned under the standard cleaning procedures (acetone, methanol, DI water). A continuous wave CO_2 laser with 10.6 μm wavelength was used for evaporating the stoichiometric powders placed on a custom-made graphite boat ($1.2\times0.7\times0.7$ cm^3). The graphite boat was placed inside the 1-inch furnace tube with one end connected to the vacuum pump and another end terminated by a Zinc Selenide (ZnSe) optical window for the CO_2 laser beam entrance. First, the tube furnace was pumped down to a few millitorrs, followed by purging argon gas to remove the residual molecules from the tube and adjust to the desired background pressure. The tube furnace was used to adjust the growth temperature independent of the evaporation temperature. The laser power varied from 30 W to 55W depending on the precursor.

The laser irradiation time was tuned from 90 to 120 seconds. Finally, the system was naturally cooled down by turning off the furnace immediately after stopping laser irradiation and opening the tube furnace led while maintaining the vacuum system active.

2.15.2 Raman and PL Spectroscopy and Mapping.

A custom-made Raman and PL spectroscopy and mapping system was used for optical diagnostics of LAST-grown 2D materials. The measurements are performed in a confocal micro configuration using a 100x microscope objective lens (NA = 0.9) and a motorized XY stage with a 100 nm step size. A Horiba HR spectrometer was used with 1200 grooves/mm grating and a laser excitation wavelength of 532 nm.

2.15.3 TEM Sample Preparation.

Samples with 2D flakes were first spin-coated with Poly (methyl methacrylate) (PMMA) to form a thin layer of ~200 nm, using 3000 rpm for 45 s to transfer TMDC flakes from the Si/SiO_2 substrates onto the TEM grids. After being cured at 100 °C for 15 min, the PMMA/flake films were detached from the Si/SiO_2 substrates using a 20% KOH solution at 90ºC. The removed PMMA/flake films were then transferred to DI water to remove the KOH residue. Afterward, the PMMA/flake films were transferred onto the Quantifoil TEM grids, then heated with a hot plate at 100°C for 5 min. Finally, the as-prepared samples were immersed into the acetone (60 ºC, 30 minutes) to remove the PMMA, leaving 2D flake on the TEM grids.

2.15.4 Temperature Measurement

All the temperature measurements were done remotely from 50 cm away through the quartz tube with the measuring spot size of ~4 mm^2 for a silicon substrate and 10 mm^2 for a graphite boat using the IGA 15 plus pyrometer from LumaSense Technologies. This pyrometer is chosen based on its spectral responsivity compatible with the transmission of the quartz tube. The pyrometer

was capable of measuring from 250 °C to 1800 °C, which is well in between the range of our measurements. While measuring the temperature with the pyrometer, graphite and silicon emissivity were selected as 90 and 71, respectively. The pyrometer was factory calibrated and rechecked using the built-in tube furnace thermocouple.

2.16 Summary

A new and universal laser-assisted synthesis technique (LAST) demonstrates the growth of large 2D materials directly from stoichiometric powders. This technique offers a significantly simplified growth mode that eliminates the existing complexities, such as uncontrolled gas-phase reactions and flow dynamics in the current gas-phase growth methods. This method has shown a novel way to decouple the evaporation of stoichiometric powders from their 2D growth temperatures by a selective laser irradiation process. Due to high vaporization temperatures of stoichiometric TMDC powders (e.g., ~1400 ºC for MoS_2) compared to their growth temperature (e.g., ~850 ºC for MoS_2), the use of stoichiometric powders in current CVD systems has not been considered or possible. The use of a selective laser heating process allows efficient decoupling of the evaporation and growth processes enabling the growth of a large number of 2D materials directly from their stoichiometric powders. This laser-assisted approach also offered rapid heating, evaporation, and growth as well as cooling and termination control in the system. Growing Various 2D TMDC materials, including monolayer MoS_2, WS_2, $MoSe_2$, and WSe_2 crystals, shows the universality of this laser-assisted synthesis technique. This method presents a simple yet general approach capable of accelerating the synthesis and discovery of emerging 2D quantum materials.

Note. This chapter is a slightly modified version of Nurul Azam et al."Accelerated synthesis of atomically-thin 2D quantum materials by a novel laser-assisted synthesis technique." 2D Materials 7, no. 1 (2019): 015014.

CHAPTER 03

TIME-RESOLVED ULTRAFAST GROWTH OF TWO-DIMENSIONAL QUANTUM MATERIALS

3.1 Introduction

In this study, the time-resolved (sub-second) capability of the 2D crystal growth has been systematically established. This time-resolved growth strategy enables the ultrafast growth rate ever reported to date on a non-catalytic substrate (Si/SiO_2). A novel gas-phase laser-assisted synthesis technique (LAST) demonstrated in chapter-two overcomes most of the challenges associated with the existing bottom-up synthesis methods and successfully synthesizes high-quality semiconducting TMDC crystals such as WSe_2, $MoSe_2$, WS_2, and MoS_2 crystals[25]. The unique features of LAST were instrumental in developing the time-resolved synthesis of 2D TMDC quantum materials. Instead of multi-component precursor vaporization and mixing as in conventional thermal CVD, in the LAST system, direct vaporization of stoichiometric powders (e.g., WSe_2 powder) was achieved with a continuous wave CO_2 laser while an external furnace controlled the growth temperature. Such independent control of the laser vaporization and growth processes is a critical problem to overcome[153] to independently supply feedstock without hampering the growth dynamics within a short time scale as low as 10 ms. The ultrafast feedstock supply and rapid termination option through laser irradiation make the growth environment ideal for the time-resolved study. It should be noted that the ultrafast feedstock supply naturally prevents nucleation formation problem without any physical design adoption. In addition, this system supply zero nucleation before reaching the optimal growth condition since growth start with laser irradiation after reaching to the growth condition by the furnace. The remarkable growth rate (100 μm/s) and shortest synthesis time (10 ms growth) were both achieved in this process using a 120W

laser. Data analysis and process parameters suggest that these numbers are scalable with higher-power lasers (>120W). Various characterization schemes such as Raman spectroscopy, photoluminescence spectroscopy, and atomic force microscopy confirm the quality of the grown crystal.

3.2 Key Enablers of Time-Resolved 2D Crystals Growth

The spatial and temporal control of the vapor flux is the key to achieving a time-resolved study of 2D growth. A laser vaporization process allowed localized vapor flux generation by direct vaporization of stoichiometric powders while eliminating the need for precursor mixing and complex chemistry for the growth process. The localized laser heating of a graphite boat[125] containing the precursor powders achieved enough temperature in a short time to evaporate the stoichiometric powders. This technique addressed the critical challenge of growing 2D materials from their bulk counterpart due to the significant difference between the vaporization temperatures of stoichiometric powders and their growth temperatures. For instance, WSe_2 needs ~1500 °C for evaporation [154], while the growth temperature of the WSe_2 monolayer is near ~900 °C. Furthermore, the ability to rapidly control and modulate the laser power allows initiation and termination of the growth process at desired time stamps. Thus, localized flux generation, instant flux initiation, instant flux termination, and simplified chemistry enable ultrafast and time-resolved 2D WSe_2 crystal growth.

3.3 Experimental Setup and Procedure

Figure 3.1a-c shows the growth system where a vacuum tube furnace of a 1-inch diameter facilitates the growth environment by providing the right temperature and pressure to the growth zone (Si/SiO_2 substrate). Before the synthesis process started, stoichiometric WSe_2 powder (~10mg) was placed in a homemade graphite crucible for evaporation. The growth pressure was

kept at 150 Torr throughout this study to maintain monolayer growth (**Figure 3.1d-e**). Also, Si/SiO_2 substrate was kept upside down at a constant distance right above the graphite crucible, as shown in **Figure 3.1 a-b**. Depending on the graphite laser irradiation time and power, the stoichiometric powder's evaporation was precisely controlled during the synthesis process. It is evident from **Figure 3.1c** that growth and evaporation dynamics are ideally decoupled to facilitate 2D monolayer crystals formation from the bulk stoichiometric precursor powder. The doted pulse represents the laser on time or laser irradiation time, defined as the growth time throughout this study. According to the substrate temperature measurement during the process, at longer growth time (>1s), some heat transfer (up to ~150 °C) from the boat to substrates was observed (**Figure 3.2b).** However, no heat transfer from the boat to the substrate was observed at a shorter timescale (<1s) (**Figure 3.2b)**.

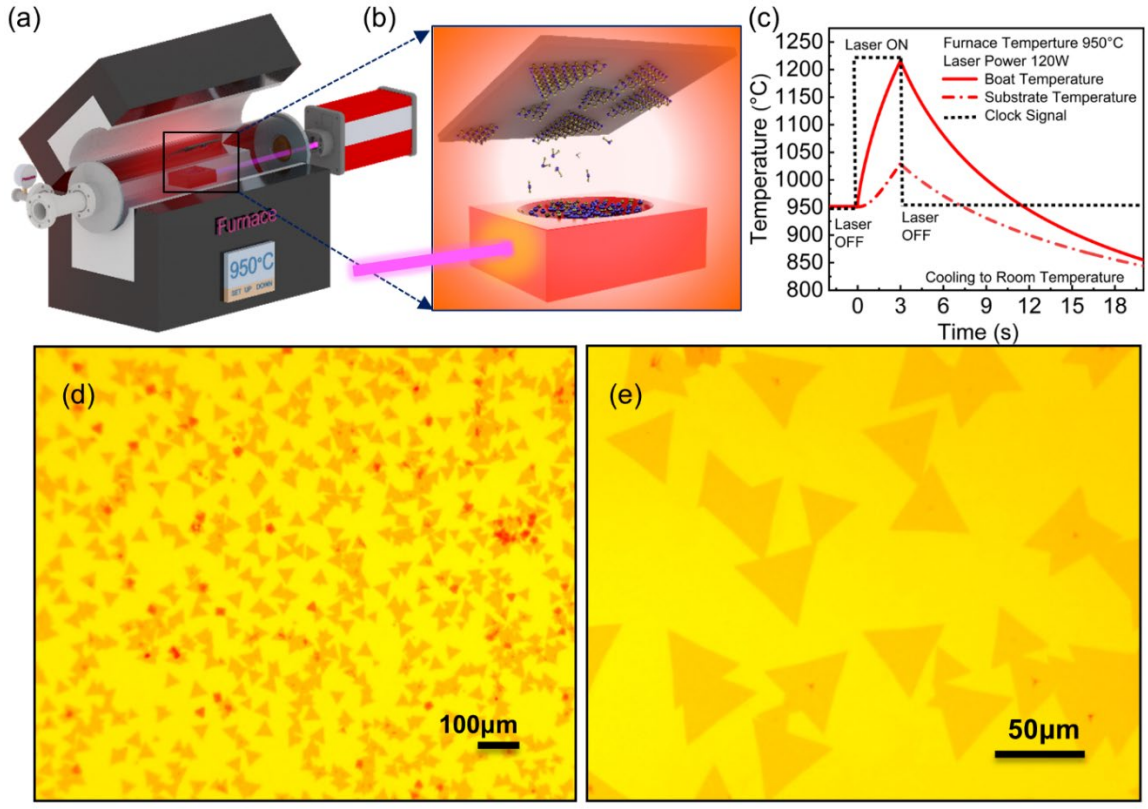

Figure 3.1 Graphic illustration of the time-resolved growth technique: **(a)** In the laser-assisted synthesis technique (LAST), a continuous wave CO_2 laser heats the stoichiometric bulk precursor powder through a graphite crucible. The laser power and irradiation time control the vapor supply rate to the growth zone. On the other hand, a tube furnace separately controls the crystal growth kinetics. Inert argon gas is used to create the background pressure. **(b)** An enlarged version of the evaporation and growth zone. **(c)** An illustration of time-correlated temperature profiles of the boat (continuous red line) and substrate (dotted red line) for a specific laser irradiation time (dashed black line). The graphite crucible and substrate temperature remain the same at furnace temperature before laser ON ($t < 0$) (in this case, 950 °C). As soon as the laser irradiation was initiated ($t = 0$s), both the graphite crucible and substrate temperature continued to rise. Turning off the laser and the furnace simultaneously ($t = 3$s) terminated the growth process. **(d, e)** Optical images of a representative sample with mostly uniform monolayer crystals.

3.4 Experiment Design of Time-Resolved Crystal Growth

The first set of experiments was focused on determining the time-resolved growth correlation to the laser power, irradiation time, and furnace temperature using a custom-made graphite boat with $1\times0.6\times0.6\ cm^3$ dimensions with 0.5mm wall thickness (**Figure 3.1b**). This graphite boat provided a moderate heat coupling to the powders, and variation of the laser power allowed the system to achieve ~10 - 25 °C temperature control of the boat with laser heating. Laser powers ranging from 40 to 120W for three different irradiation times (2s, 3s, 5s) at 850, 900, and 950 °C furnace temperatures were tested to capture the crystal growth dynamics from no crystal growth to growth and re-evaporation conditions. A pyrometer from LumaSense Technologies (IGA 15 plus) was used to measure the graphite boat temperature profile for each experimental condition remotely from a 50 cm distance with ~4 mm^2 spot size through a quartz window (**See**

Section 3.11, Figure 3.8). **Figure 3.2a and b** show the temperature profiles of the graphite boat and substrate for the chosen furnace temperatures (i.e., 850, 900, and 950 °C) and laser powers (40 to 120W), respectability. **Figure 3.2c** shows the cooling profiles of both the substrate and graphite boat for the 120W laser power condition and the corresponding furnace temperatures.

3.5 Process Parameters and Time-Resolved Crystal Growth

Figure 3.2d-f shows the peak temperatures of the graphite boat for each experimental condition (**See Section 3.11, Figure 3.8**). The corresponding crystal growth results demonstrated a correlation between the process parameters (vapor supply and furnace temperature) and the crystal domain size, as shown in **Figure 3.2g-i.** For example, 850°C sustains a steady acceleration in crystal growth where the 5 s growth curve maintains the highest slope of 0.83 while 2 s maintain a 0.23 growth slope. Other furnace temperatures followed the same trend. Every 10W increase in laser power increased the vaporization temperature by ~25 °C resulting in ~5-7 μm increase in the crystals edge length. As the irradiation time increased, the crystal size increased steadily for all the furnace temperatures and laser powers. **Figure 3.2g-i** shows that increased furnace temperatures accelerated the growth rate, as is evident from the stepper slope of the graphs. For example, 5 s laser irradiation shows 0.83, 1.13, and 1.39 growth slopes for 850°C, 900°C, and 950°C furnace temperatures, respectively. It was also observed that for 2 seconds irradiation time at 850 °C furnace temperature, crystals started to develop from 70W laser power (corresponding to ~1000 °C graphite boat temperature) while the re-evaporation process started from 70W laser power at 950 °C for 5second irradiation (corresponding to ~1250 °C graphite boat temperature). In this experimental window, crystal size varied from 3 μm to 105 μm. It is also visible from **Figure 3.2g-i** that, in the low irradiation time, such as 2 s and 3 s, the growth slope is in the same range, while the 5-second irradiation growth slope is a little higher for each furnace case. The key reasons are

(1) an increased feedstock supply and (2) a temperature leak from the boat to the substrate for the higher irradiation time. Overall, these process parameters and crystal growth dynamics show how this technique fundamentally differs from the existing TMDC synthesis method and indicates possible ways to accelerate the crystal growth rate, which have been discussed in the following sanctions in more detail.

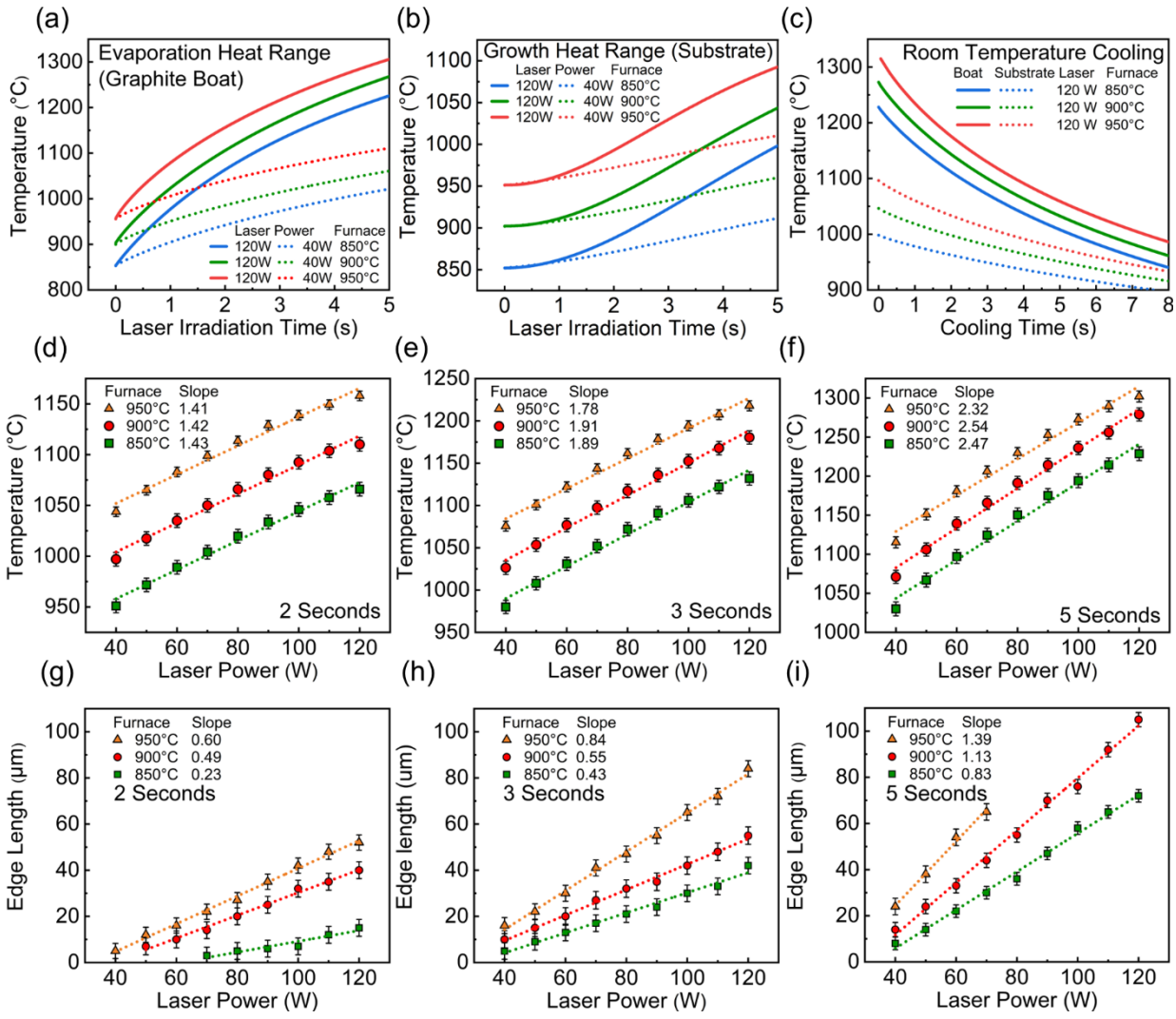

Figure 3.2 Process parameters and crystal growth correlations in the time-resolved study. Process parameters such as laser irradiation (0-5s), furnace temperatures (850, 900, and 950 °C), and a wide range of laser powers (40 to 120 W) were used**.** (a, b) graphite boat and substrate rising

temperature profile as a function of irradiation time for 120W (solid lines) and 40W (dashed lines) laser powers, respectively. The substrate temperature profile indicates for t<1s, the growth and evaporation temperatures are completely decoupled (i.e., the heat from the boat is not affecting the temperatures of the substrate). (c) The boat (solid lines) and substrate (dashed lines) cooling profile for 120W laser irradiation while the furnace was at different furnace temperatures. (d-f) the graphite boat at different laser powers and furnace temperatures after laser irradiation time of t = 2, 3, and 5s are plotted to analyze the growth dynamics. Interestingly, the slopes remain relatively unchanged for different furnace temperatures indicating the system stability for time-resolved crystal growth studies. The detailed temperature measurements of (a-f) are shown in **Section 3.11, Figure 3.8)**. (g-i) The crystal edge length as a function of the laser power for different irradiation times and furnace temperatures. For constant furnace temperatures, the slope increases with the laser irradiation time and furnace temperature, while for a given laser irradiation time, the growth curve starts to ramp as the furnace temperature increases.

3.6 Growth Rate Analysis for Time-Resolved Studies

The time-resolved growth curves in **Figure 3.2 g-i** set the relationship between the process parameters and the crystal growth dynamics, such as building relationships with surface diffusions (furnace) and feedstock supply (laser power and laser irradiation time). Since the growth rate is convoluted results from the surface diffusion and the feedstock supply, **Figure 3.2 g-i** data was investigated in terms of the constant furnace temperature (**Figure 3.3a-c)** and constant laser power (**Figure 3.3d-l**) for further analysis of the growth dynamics. This investigation creates a unique opportunity to make a figurative comparison between feedstock supply and surface diffusion contribution separately in the growth of the crystals.

The growth evolution at the constant furnace temperature follows a linear tread and a particular growth curve. This statement holds for all laser power and furnace temperature (**Figure 3.3a-l**). This strong correlation between a large set of experimentations (total 81 in the initial set) and crystal growth controlling system parameters such as furnace and laser power represents the system's robustness. The growth rate ramping occurs with either the laser power (**Figure 3.3d-l**) increases or the furnace temperature **(Figure 3.3a-c).** For example, every 10W (**Figure 3.3a-c**) increase in the laser power or every 50°C furnace temperature (**Figure 3.3d-l**) significantly ramps the growth rate showing the system sensitivity to a slight change in flux or surface diffusion. In most studies, it has been reported that excessive precursor amounts or feedstock supply resulted in increased nucleation rates due to the supersaturation of precursors[155, 156]. Those high nucleation rate results in smaller domain crystal sizes. From **Figure 3.3d-l,** it is clear that this situation is the opposite of this synthesis technique. Two distinct reasons work in this case; firstly, a high growth rate prevents the increased nucleation at any rate of the feedstock supply, and secondly, before reaching the optimum growth temperature laser does not irradiate the powder. Hence there is no nucleation site created before growth starts.

On the other hand, in this technique, surface diffusion is only limited to the re-evaporation temperature. Before re-evaporation temperature, surface diffusion can be increased without hampering the feedstock source, which is challenging in most existing synthesis techniques. The non-ideal decoupled case, such as longer irradiation time at higher laser power, shows an increased growth rate because of the excessive thermal leak from the graphite boat to the substrate.

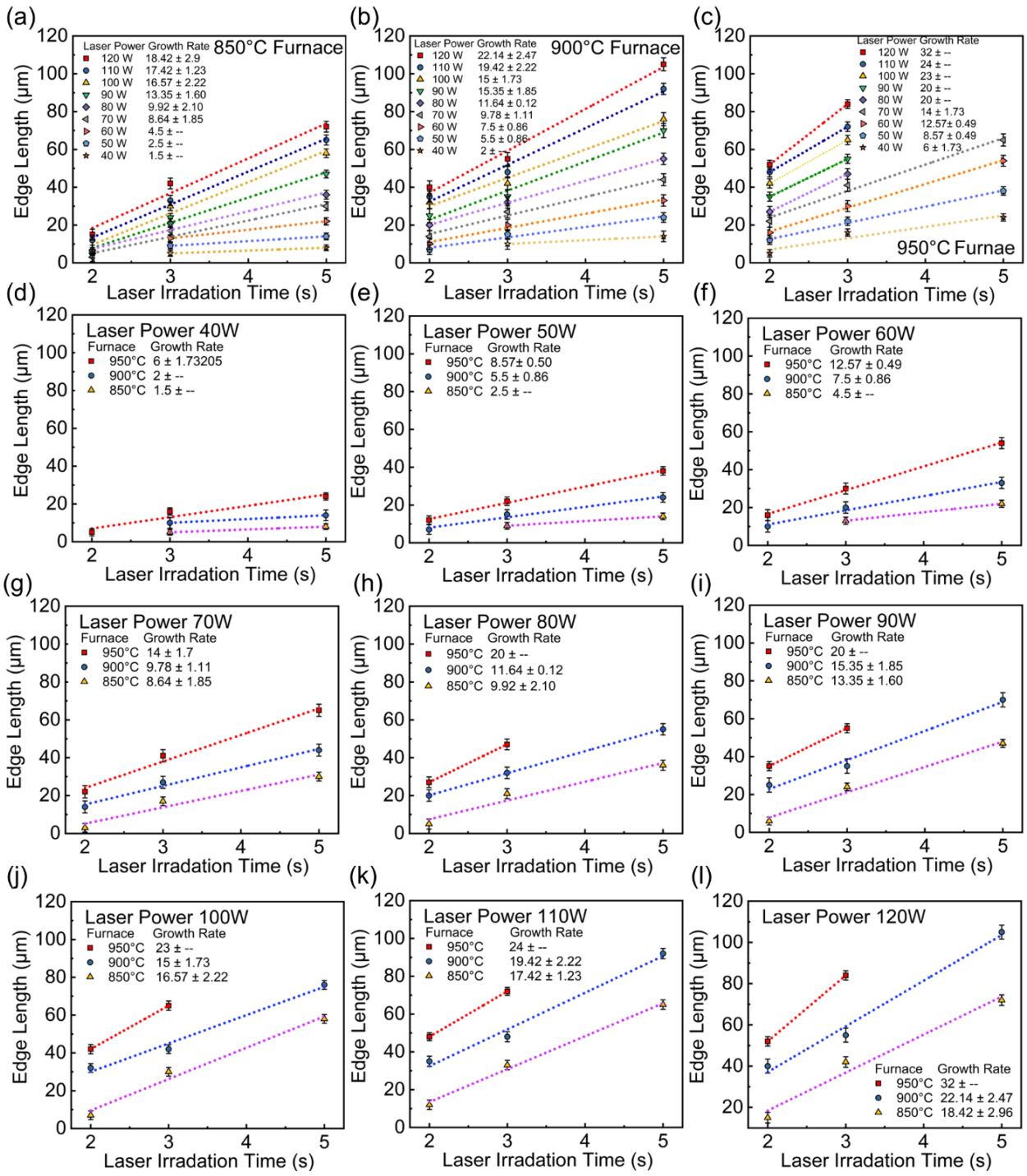

Figure 3.3 Crystal growth evolution. (a-c) The graphs illustrate the crystal edge length and growth rate (slop) at constant furnace temperatures of 850°C, 900°C, and 950 °C. The crystal evaluation at different vapor flux supplies (i.e., evaporation laser powers) and constant diffusion rate (i.e.,

substrate temperature) ramp up steadily, and the growth rate further accelerates at higher furnace temperatures. (d-l) The graphs illustrate the edge length and growth rate (slop) at constant laser powers of 40 to 120W with 10W increments. The vapor flux is constant (i.e., evaporation laser powers), while diffusion (i.e., substrate temperature) varies. In this case, the crystal growth rate (slope) remains nearly the same for the 850 and 900 °C furnace temperatures, while the 950 °C furnace temperature is almost double the growth rate for all the laser powers.

3.7 Optical Images of Time-Resolved Crystal Evolution

The optical image of the grown crystal conveys valuable first-hand information regarding the growth dynamics. **Figure 3.4** is the representative monolayer crystal growth evolution for each experimental condition described in **Figure 3.2 g-i.** In the chosen growth window, the structural integrity remains uniform. In comparison between the three furnace temperatures, the 850°C furnace shows some dots on the crystals (for example, 850°C, 50 W at 3 s irradiation), indicating less surface diffusion, while 950°C shows some extended trunk (for example, 950°C, 120 W at 2 s irradiation) because non-equilibrium between larger incoming flux relative to less the surface diffusion rate. The 900°C furnace shows finer structural integrity where the equilibrium between surface diffusion and incoming flux staled.

Similarly, in the time scale perspective, 3 s laser irradiation at all laser power shows better crystal structural integrity than 2 s and 5 s where equilibrium seems either below or over optimal conditions. Equilibrium just below the re-evaporation temperature produces larger crystals. For example, 120 W laser irradiation for 5s at 900°C furnace temperature produces 105μm single crystal with a clipped edge at a 21μm/s growth rate. The crystal clipping on the triangle's apex after 100 W at 5 s irradiation at 900 °C furnace temperature indicates the start of the re-evaporation process (**See Section 3.15, Figure 3.14**).

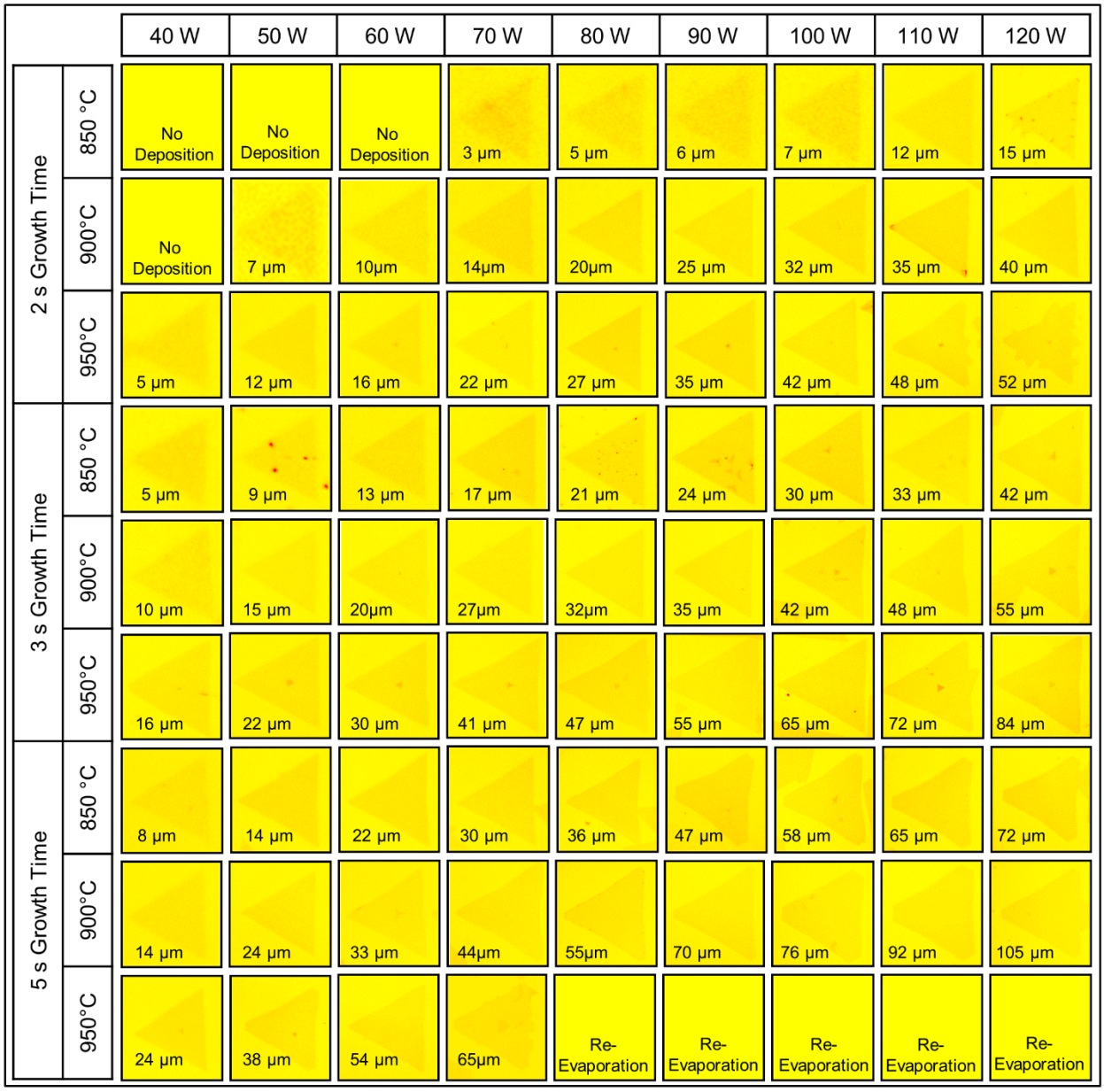

Figure 3.4 Optical images of the crystal evolution. Optical images of the crystals captured at 50X magnification for each experimental condition are described in **Figure 3.2 g-i and Figure 3.3 a-l**. Each flake represents the indicated growth conditions. The onset of crystal growth occurs at 2s laser irradiations for 70W laser power (boat temperature > ~1000C) and 850 °C furnace temperature. On the other end, the re-evaporation of crystals due to excessive heat starts from 5s laser irradiations at 80W laser power while the furnace temperature is at 950 °C. At lower laser

powers and shorter times, flakes consist of small nucleation spots suggesting that the incoming flux is overwhelmed by a low lateral diffusion rate. The 3 seconds irradiation time at different laser powers shows structurally sharp triangular flakes at all three furnace temperatures suggesting the thermodynamic equilibrium condition where incoming flux and the growth conditions are at equilibrium.

3.8 Ultra-Fast Sub-Second Crystal Growth

The analysis discussed in the previous section provided an initial understanding of the interplay between process parameters and 2D crystal evolution. In the first part of the study, the growth time was limited to 2 seconds due to the insufficient heat coupling to the graphite boat with our low-power laser (120W). Higher temperatures could be achieved either by using a higher-power laser or smaller and thinner-wall graphite boats (**See Section 3.11**, **Figure 3.9-3.10**). **Figure 3.5** presents the results achieved for the 0.3 mm thin graphite boat but the exact dimensions, as in the previous experiment shown in **Figure 3.2**. With this modified graphite boat design, 2D materials could grow with time-resolved ultrafast speed using the same 120W laser power.

With the new boat, 950°C furnace temperature and laser irradiation time beyond 3 s at 120 W re-evaporated flake. The growth time from 3 s to 300 ms resulted in the crystals with ~60 µm/s growth rate, as shown in **Figure 3.5a** (green dotted line) under 950°C furnace condition. Below 300 ms and down to 10ms growth time, crystals with ~100µm/s growth rate were achieved under >950°C furnace (1000°C and 1050°C). Below 10 ms, no crystal growth was observed while the furnace temperature was set to a maximum of 1050°C under 120W laser irradiations. The corresponding temperature profile of the thin-walled (0.3mm) graphite boat at 120W laser power for different furnace temperatures, such as 950 (green dot), >950 °C (red dot), indicates enhanced temperature coupling **(Figure 3.5b),** facilitating the ultrafast vaporization and growth process **(See**

Section 3.11 Figure 3.9). The optical images of the corresponding experimental conditions show structural integrity, while the nucleation dots (**See Section 3.16, Figure 3.15**) are visible at shorter growth time scales **(Figure 3.5c).** It should be noted that no other synthesis method has achieved such time-resolved and ultrafast growth rates on catalytic or non-catalytic substrates. The fastest reported growth rate on Si/SiO_2 is ~45um/s.[84]

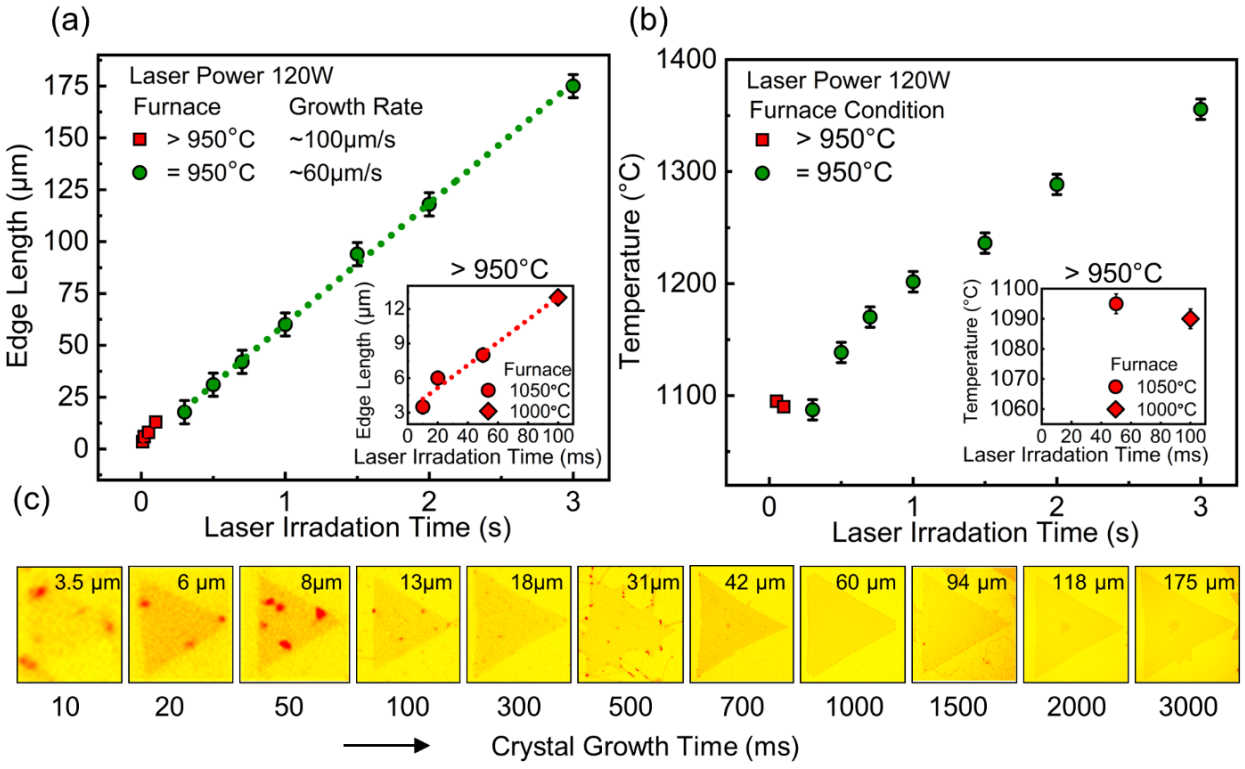

Figure 3.5 Ultra-fast time-resolved growth dynamics. The graphite boat thickness was reduced from 0.5 mm to 0.3 mm for the ultrafast growth process to enhance the boat's heat coupling. (a) The graph shows the ultrafast growth of 2D crystals with a growth rate of up to 100 μm/s and a growth time scale down to 10 ms. (d) The corresponding temperature profile of the thin-walled graphite crucible at 120W laser power for different furnace temperatures, such as = 950 °C (green dotted line) and >950 °C (red dotted line), showing the ultrafast growth. (c) The optical images of

the corresponding 2D materials at the indicated experimental conditions show structural integrity, while the nucleation dots are visible at shorter time scales**.**

3.9 Key Process Factors for Accelerated Growth

Figure 3.6 summarizes the factors that impact the crystal growth dynamics to understand the process better. The laser powers and irradiation times were translated to the heat coupling to the graphite boat with two different wall thicknesses, as shown in **Figure 3.6a.** It clearly shows that the increased slope of crystal edge length for thinner graphite boats is due to faster and higher heat coupling. Closely examining **Figure 3.2** and replotting the data in **Figure 3.6b** reveals identical products of laser powers and irradiation time; for example, 5s at 60W, 3s at 90W, and 2s at 120W produce 20µm flakes at 850 °C furnace temperature. Increasing the furnace temperature by 50 °C dramatically increased the flake size. For an instant, similar flux but 900 °C and 950 °C furnace temperatures produced 40 and 60µm domain sizes, respectively (**See Section 3.13, Figure 3.12**). This analysis reveals the impact of the furnace temperature on the substrate, such as enhancing diffusion for faster crystal growth dynamics.

Nevertheless, creating a similar flux generation condition is unique to this study as no other synthesis technique can generate the exact flux supply condition to the substrate. Utilizing the 120W laser as our guide, **Figure 3.6c** shows the COMSOL Multiphysics simulation results (**See Section 3.12**, **Figure 3.11**) for higher laser powers of 150, 200, 250, and 300W. This temperature coupling from simulation suggests that higher laser powers, such as 300W, may achieve an unprecedented growth rate and ultra-small time resolutions (<10ms) using the current experimental setup.

Overall, time-resolved growth mainly depends on the quantified and distinct amount of the feedstock supplied by the laser energy with tuning laser power and irradiation time (**Figure 3.2-**

3.5). In addition, escalating the growth temperature up to 1050°C for a shorter time (**Figure 3.5a**) is another remarkable achievement since it allows one to choose any surface diffusion rate removing the bar to achieve a high growth rate on the non-catalytic substrate.

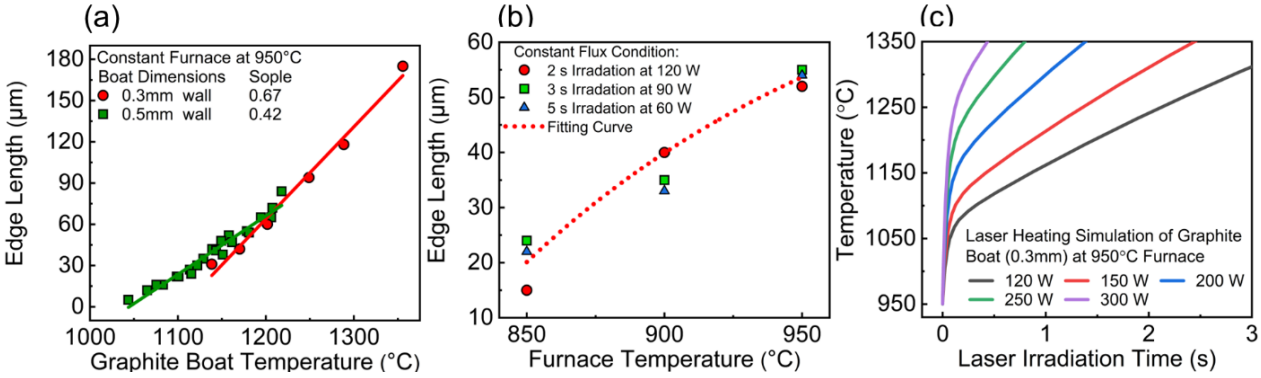

Figure 3.6 Key process factors for accelerated growth. For ultrafast growth, a quick supply of the vapor flux is key to accelerating the growth, which depends on the enhanced laser coupling and accelerated heating of the boat, which relies on three factors (a) Reducing the wall thickness of the graphite boat was an efficient approach to instantaneous heating and vaporization of the stoichiometric powder. (b) Controlling the substrate temperature without hampering the source, for example, three similar source conditions, such as 2 s irradiation at 120 W, 3 s irradiation at 90 W, and 5 s irradiation at 60 W laser power, produced crystals with the exact domain sizes for each furnace temperature while larger crystals for the higher furnace (e.g., ~20 μm for the 850 °C, ~40 μm for 900 °C, and ~60 μm for 950 °C for all three cases). (c) Simulation results show that the increased laser power can also be instrumental for increased heat coupling into the boat. For instance, a 300W laser can achieve five times quicker vaporization temperature, potentially accelerating the growth rate with microsecond growth time scales.

3.10 Characterization of the Grown Crystals

Optical spectroscopy and mapping of the monolayer WSe_2 crystals were performed to analyze the crystalline quality of the grown crystal at different time scales. Raman active modes, including E^1_{2g} at ~236cm^{-1} and $A^1_{\ g}$ at ~251cm^{-1}, were seen in all growth time scales with no detectable variations.[157] Similarly, in the PL spectra, a prominent emission peak at ~748 nm (**Figure 3.7b**) with full width at half maximum (FWHM) of 31.35 nm was observed in monolayer crystals grown above 500 ms, similar to the reported values in literature [158]. However, below 500 ms growth time, the wavelength of PL spectra was mostly around ~748 nm but with a broader FWHM of ~36.37 nm. Slight red-shifted (**See section 3.17, Figure 3.16**) emission was also observed in some crystals at shorter timescales. This FWHM widening and the slight red shift could be due to higher defect density formed in these premature crystals at such short time scales[159]. The PL maps of the monolayer crystals showed the overall uniformity of the grown crystals. **Figure 3.7d** shows the PL map of the representative crystals' growth at 100 and 500 ms time scales. The AFM height profile of representative monolayer crystals (**Figure 3.7e)** showed a 0.7nm step size consistent with the reported monolayer value[126].

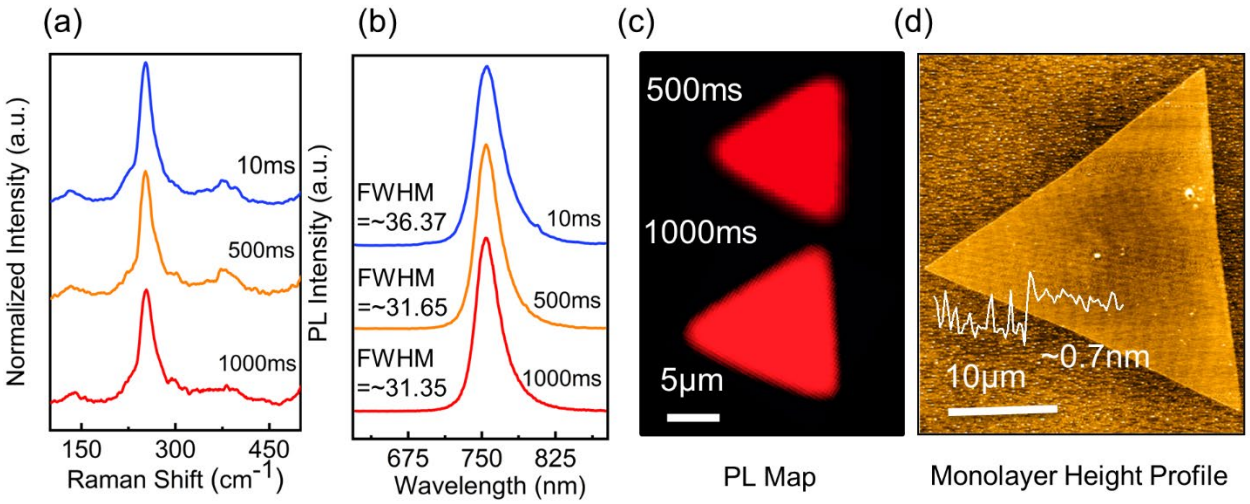

Figure 3.7 Characterization of the grown crystals: Optical spectroscopy and mapping of the single-layer WSe_2 crystals under a 532nm laser excitation source. Raman (a) and PL (b) spectra show the characteristics of peak location at different time scales such as 10ms, 500ms, and 1000ms. Crystals grown below 500ms show some red-shifted PL peak toward 780nm, possibly due to defect formations **(See section 3.17**, **Figure 3.16**). The PL maps (c) of the monolayer crystals show the overall uniformity of the grown crystals at 1000ms and 500ms. AFM image of a monolayer crystal (d) showing the expected 0.7nm high profile.

3.11 Temperature Measurements

The temperature measurements at experimental conditions described in **Figure 3.2d-f and Figure 3.5b** have presented in this section. For measuring the temperature profile, the graphite boat was irradiated by 40 W to 120 W laser power with 10W intervals for 2s, 3s, and 5s laser irradiation time under three different furnace temperatures as 850°C, 900°C, and 950°C. A pyrometer from LumaSense Technologies (IGA 15 plus) was used remotely from a 50 cm distance. The measuring spot diameter is ~5 mm. The emissivity of the pyrometer was set to 90 for all the graphite boat temperature measurements. To access the graphite boat while the laser heating and cooling inside of the tube furnace, similar to the experimental setting, measurements have been facilitated through a quartz window connected to one end of the furnace. It should be noted that the cooling profile is much faster in the actual experiment than appear in the measuring graph since, during temperature measurement, cooling has been performed under respective furnace conditions. In contrast, for experimental cases, cooling was performed at room temperature.

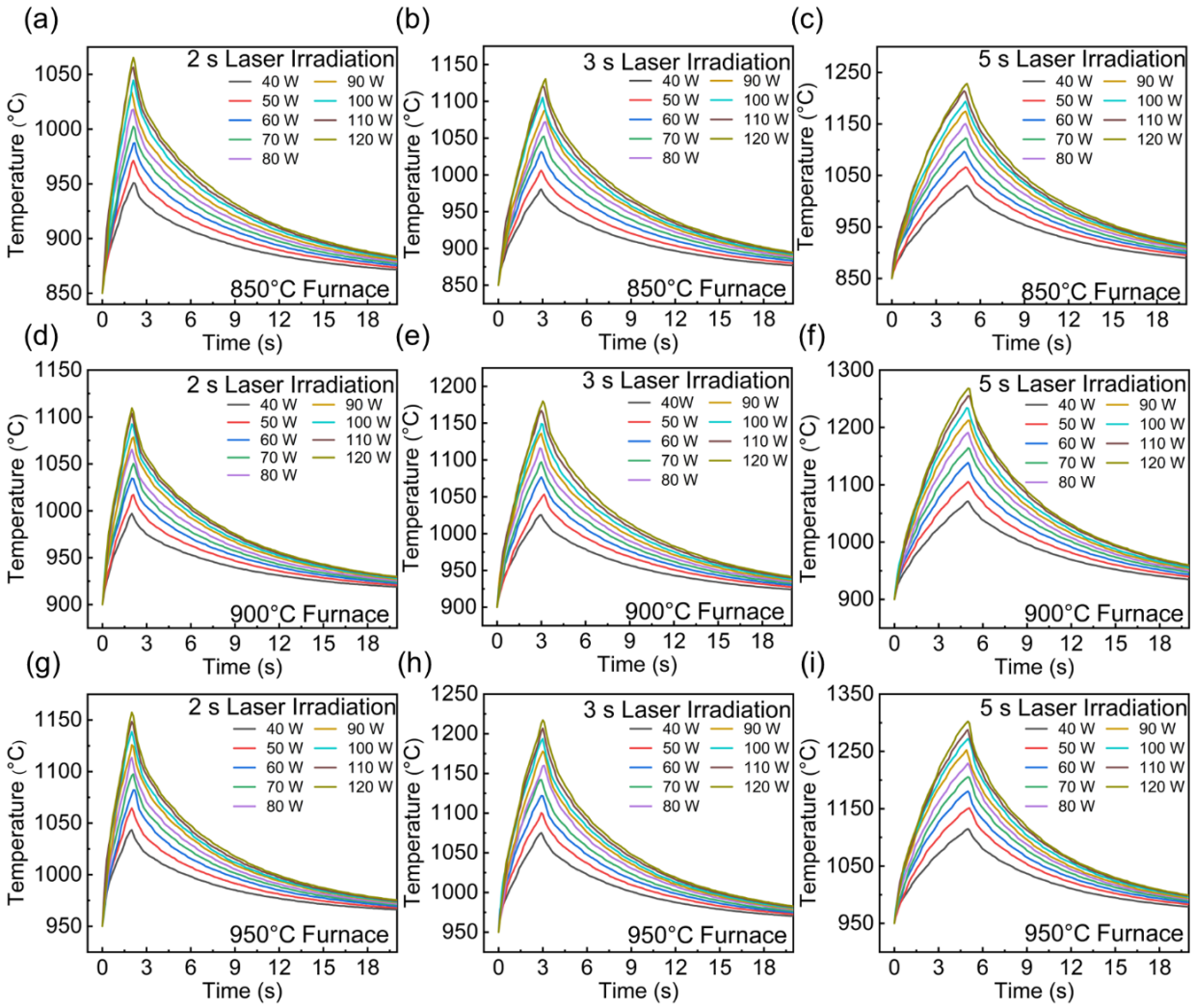

Figure 3.8 temperature measurements for the time-resolved study: The key to the time-resolved mechanism is to create a uniform gradient of temperature coupling with the smallest possible resolutions. The temperature rise time and peak temperature are the indicative parameters that co-relate the amount of flux generated in each experimental case and impact the crystal growth dynamics. The temperature profile of the graphite crucible (0.5mm wall thickness) for a different combination of laser irradiating time, laser power, and furnace temperature is instrumental in explaining the growth dynamics results tabulated in **Figures 3.2-3.3** where the peak temperature of these measurements co-relates with the ' 'flake's edge length for each experimental condition.

In a similar process, the temperature measurement was repeated for the thin graphite boat (0.3 mm). As shown in **Figure 3.9a-c,** the thin graphite crucible was irradiated by 120W laser power at different time scales (10 ms to 3 s) for three different furnace temperatures such as 950°C, 1000°C, and 1050°C. Experimental cases described in **Figure 3.5a-b** was performed under higher furnace temperatures to increase the chance of growth with 120W laser at shorter time scales. For example, 10 ms, 20 ms, and 50 ms time scale growth were facilitated under 1050°C furnace temperature while 100 ms growth was facilitated under 1000°C furnace, and the rest of the experiments from 300 ms to 3 s were performed under 950°C furnace condition. **Figure 3.9a-c** shows the temperature measurements profile at these described conditions. **Figure 3.5b** has been constructed by plotting the peak temperature found in **Figure 3.9a-c.** As in the previous case, the cooling profile is much faster in the experimental cases than shown in the temperature profile measurements as the graphite boat cooled under the furnace environment after laser irradiation shown in **Figure 3.9a-c**. Since the temporal response of the pyrometer is 30 ms, the 10 ms and 20 ms temperature measurements show less temperature than expected.

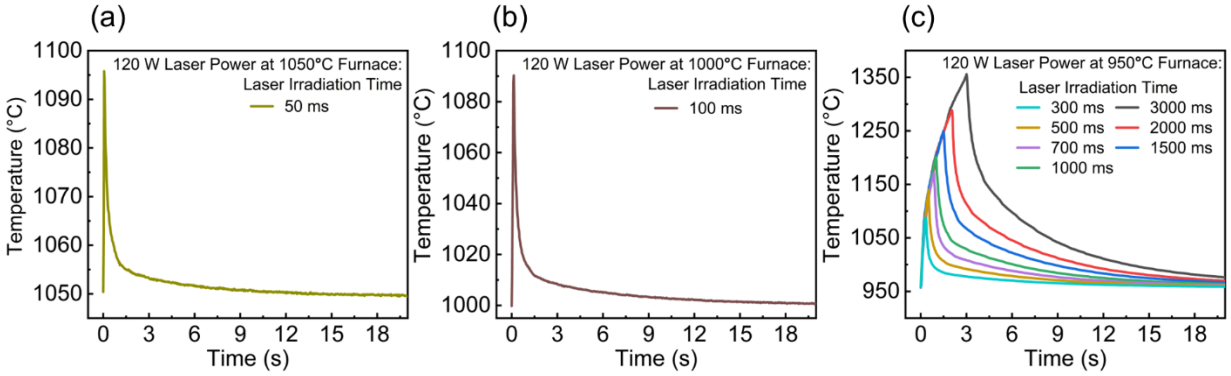

Figure 3.9 temperature measurements for the ultrafast study: Temperature profile of graphite boat (0.3mm wall thickness) at 120W laser power at various time scales (50ms to 3s) for 950C **(a)**

1000°C **(b)** and 1050°C **(c)** furnace environments. The 10ms and 20ms are excluded from the temperature measurements since they fall under the instrument measurement limit.

Both sets of measurements enable us to compare the heat coupling of the graphite boat due to laser heating with two different dimensions. **Figure 3.10** shows the temperature profiles of the thick and thin graphite crucible for 950°C furnace temperature while irradiating the crucible for 3 s at 120W laser power. It is evident from the graph that the 0.3mm thinned wall graphite crucible leads the 0.5mm thick-walled crucible by ~140°C. The COMSOL Multiphysics heat simulations show heat gradients on graphite boats for both boat dimensions, which gives us a clue for the increased heat coupling. **Figure 3.10a-b** shows thinner boat creates a more concentrated hot spot on the graphite boat, while for thicker boat shows a temperature conducted toward a larger area. Indeed, creating a hot spot and less heat conduction to the other part of the boat facilitates quicker temperature rise.

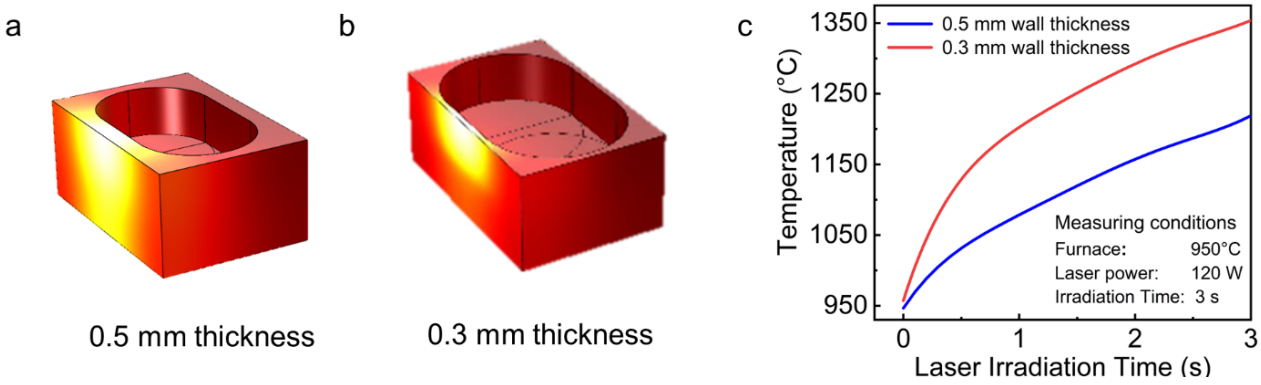

Figure 3.10 enhancing heat couponing for ultra-fast growth: Comparison of temperature coupling between different dimensions of the graphite boat. The COMSOL Multiphysics physics heat simulation shows the temperature gradient of the thicker boat (a) spreads more than the thinner boat (b), indicating narrower dimensions create more localized heat at the sorter time. The actual measurement comparison on the similar condition but different boat dimensions (c) shows that

thinned walled boat led the thick-walled boat by ~140°C in terms of temperature gain from the same condition of laser heating.

3.12 Temperature Simulations

It is evident from the previous discussion that feedstock supply is one of the vital enablers for the higher growth rate. Since the growth initiation depends on how quickly the graphite crucible reaches the powder's evaporation temperature, ramping the laser power can accelerate the growth rate more dramatically than reported in this study. A 120W laser was utilized to conduct this study in the current lab setting. It only required the heat profile of a particular laser power to calculate the growth rate for a higher laser power than 120W. Here for predicting the possible growth rate with higher laser power, the temperature of the graphite crucible illuminated by CO_2 laser at higher laser power than 120 W has been simulated with COMSOL Multiphysics software. The heat generated by a laser beam on a graphite surface is dissipated through conduction, convection, and radiation. The detailed theoretical modeling approach can be accessed in literature [125, 160]. The heat transport equation can be given as

$$Q = mC\frac{\delta T}{\delta t} + hA\delta T + A\sigma\varepsilon(T^4 - T_0^4)$$

Where C is specific heat, h is the convective heat transfer coefficient, A is the surface area of material, ε is emissivity, and σ is ' 'Stefan's constant.

Table 3.1 Simulation attributes

properties of graphite	Values
Thermal conductivity coefficient (K)	100 W $(m{\circ}C)^{-1}$
Specific heat (c)	707 $J(kg.K)^{-1}$
Density (ρ)	2210 $kg.m^{-3}$
Emissivity (ε)	0.97
Reflectivity of graphite	22.7% at 10.6 μm wavelength

The simulation has been performed for the graphite crucible dimension of 1×0.6×0.6 cm^3 with 0.3mm wall thickness while keeping the leaser heating spot size of 5 mm diameter. Before emulating higher laser power, first, the simulation results have been validated by one of the known measurements (**Figure 3.11a). Figure 3.10b/ Figure 3.6c** shows that the graphite boat's temperature reaches the powder evaporation temperature due to the high laser power heating in a much shorter time. For example, the simulation results show that the amount of heat coupling from 120 W laser irradiation for 3 s can be achieved by a 300 W laser within 0.25 s.

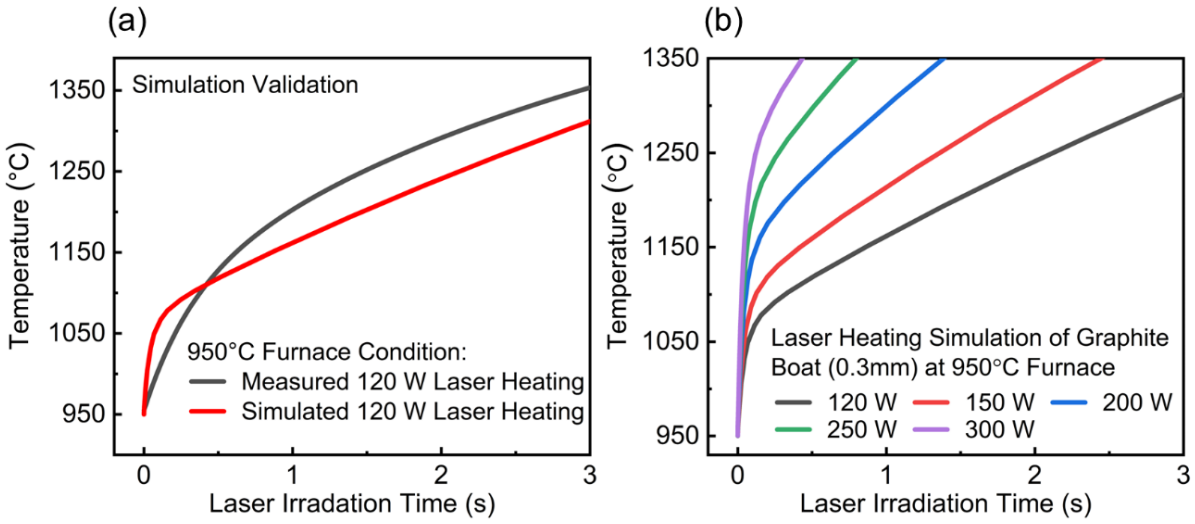

Figure 3.11 COMSOL Multiphysics simulated high-end laser: Measured and COMSOL Multiphysics simulated heat profile for 3 s laser irradiation at 120 W and 950°C furnace temperature shown for validating the simulation (a) COMSOL Multiphysics simulation for the laser heating of the graphite crucible at laser power higher than 120 W such as 150 W, 200 W, 250 W and 300 W (b).

The growth calculation shows that it is possible to accelerate the growth rate to 720µm/s with a 300W laser (**Table 3.2**)

Table 3.2 Prediction of the growth rate.

Laser power (W)	Growth time	Domain size	Growth Rate
120	3	180	60
150	2	180	90
200	1	180	180
250	0.5	180	360
300	0.25	180	720

3.13 Accelerating or Decelerating the Crystal Growth Dynamics

This technique creates a unique opportunity to generate precise gas phases depending on the laser power and irradiation time. **Figure 3.12** shows some similar laser heating conditions with different times and laser power from temperature measurements of **Figure 3.8**. In each case, the graphite boat reaches to specific temperature slower or faster depending on the laser power. Interestingly, this creates control over accelerating or decelerating the crystal growth dynamics.

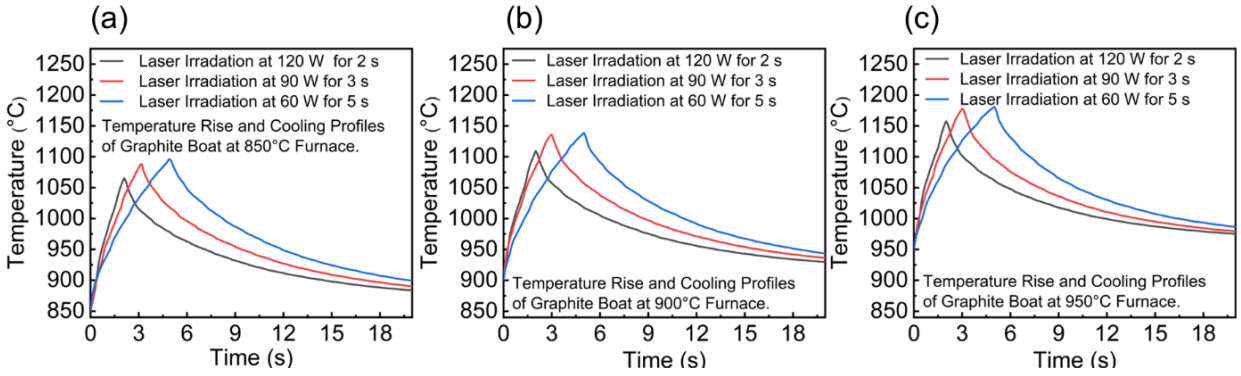

Figure 3.12 The impact of the graphite crucible and furnace temperature: Equivalency of graphite crucible heat at different laser irradiation times and power (5 s at 60 W, 3 s at 90 W, 5 s at 120 W) for 850°C (a), 900°C (b), and 950°C (C) furnace environment. These different laser power create similar peak temperatures resulting in a similar size of crystal growth.

3.14 Representative Crystal's Selection From an Experiment

Due to the localized laser heating of the graphite boat creating the gas phase, the deposition on the substrate is not uniformly distributed. For better visualization of this situation, A COMSOL Multiphysics simulation of the heat map of the graphite boat and Si/SiO_2 substrate during an experimental condition is shown in **Figure 3.13a.** From the heat map, it can be inferred that the laser heating spot achieved the maximum temperature for particular laser power and irradiation time. The amount of gas phase generated from the powder depends on this graphite boat heating area's temperature. The flux delivery area is highly localized between ~25 mm^2 on the substrate above the hot spot. 50% of this deposition area is generally uniform, as shown in **Figure 3.13c.** For choosing the most representative flake for a specific condition, this uniformly deposited area was carefully analyzed with the 50X objective of the optical microscope, where crystal sizes are primarily identical (**Figure 3.6b**). The robustness of this process can be proved in **Figure 3.13b.** For example, 2 s irradiation at 110 W, 3 s irradiation at 80 W, and 5 s irradiation at 50 W generate identical graphite boat temperature (~1150°C for 950°C furnace temperature). Now all these three different conditions produce 40 μm since the diffusion condition (950°C) on the substrate and flux supplies were the same. This production of similar flakes validates the process of statics development criteria and stability of the system over many experimentations.

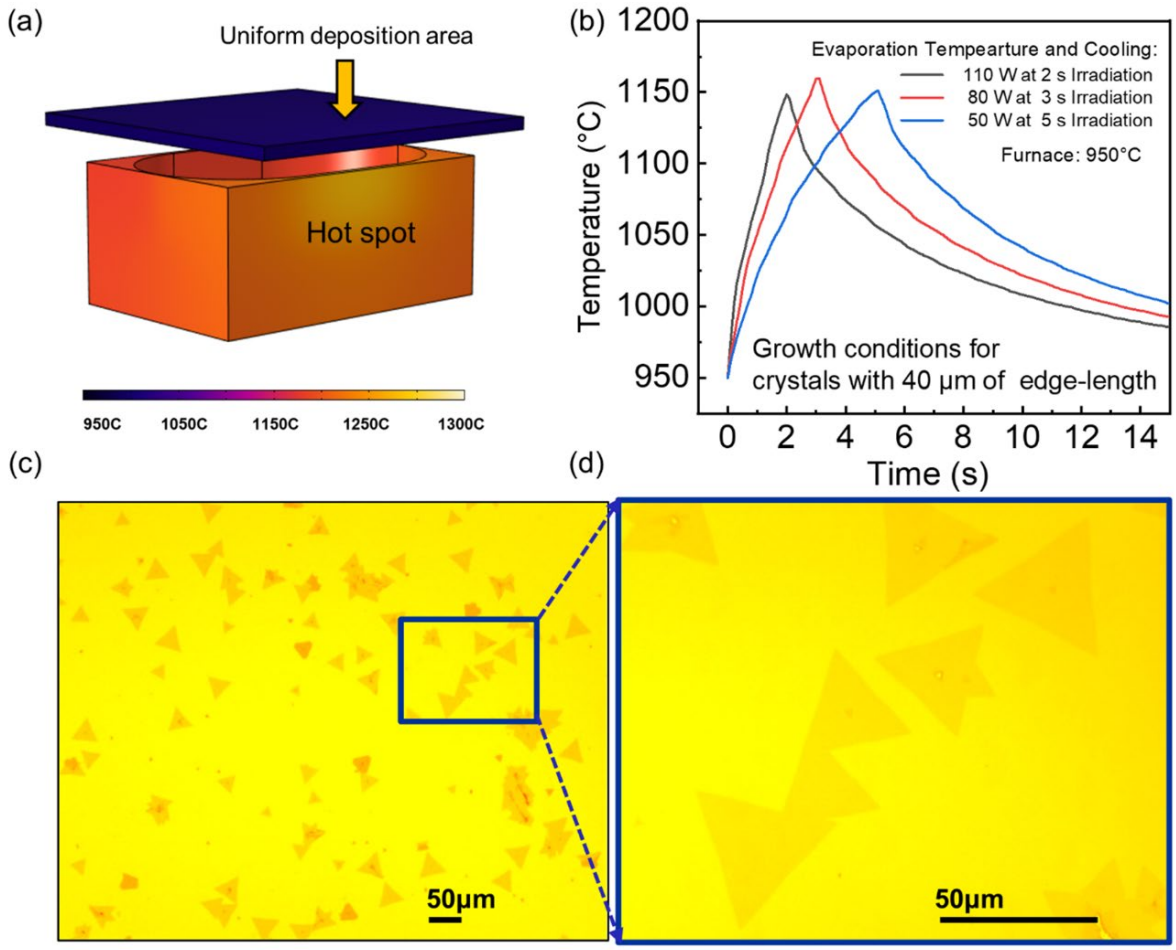

Figure 3.13 The area of interest: **(a)** heat map shows a hot spot created by the laser irradiation on the graphite crucible during the synthesis processes. At this hot spot, the stoichiometric bulk powder of WSe_2 vaporized and produced a uniform deposition of a single crystal on the Si/SiO_2 Substrate on a small localized deposition area. **(b)** At 950°C furnace temperature, three different combinations of irradiation time and laser power, such as 2s at 110W, 3s at 80W, and 5 s at 50 W, create an equivalent graphite crucible (source) temperature of ~1150°C. This identical growth condition, such as source (graphite crucible) and growth (furnace) temperature, create similar ~40 μm edge length crystals. (c, d) An example of the flake selection procedure.

3.15 Re-evaporation Process

In this synthesis technique, triangular single-crystal flakes grow in domain size as the laser continues to irradiate the graphite boat at suitable crystal growth conditions. For specific furnace temperatures, increased graphite boat temperature due to continuous leaser heating breaks the decoupling limit at a certain point and supplies convective heat to the substrate in addition to the radiative heat. This extra heat re-evaporates the already-grown crystals and simultaneously tries to develop new crystals since the feedstock supply is still on, as shown in **Figure 3.14 b**. For the thicker graphite boat beyond 70 W of laser heating for 5 s irradiation time at 950°C furnace temperature (**Figure 3.14 a**) produces evaporated flake (**Figure 3.14 b**). The re-evaporation limit was found at 120W laser irradiation for 3 seconds under 950°C furnace temperature for the thinner boat.

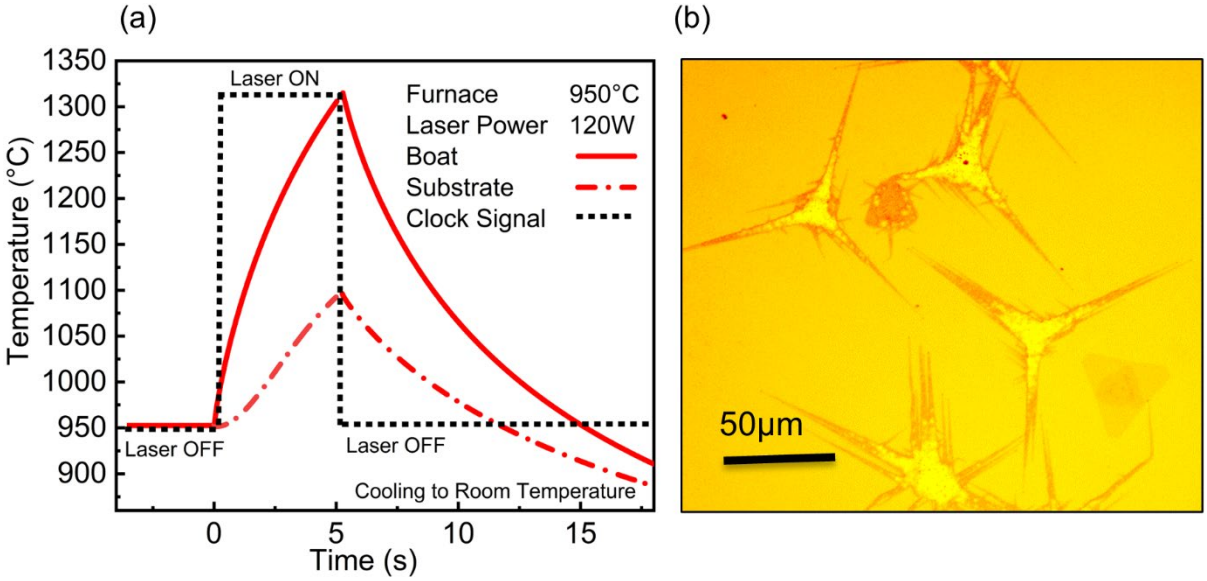

Figure 3.14 Re-evaporation dynamics: A representative re-evaporation conditions (a) and the optical picture (b) of this case describe evaporation dynamics in this time-resolved growth technique.

3.16 Flake Formation Dynamics: Ostwald Ripening

A pressure study has been performed to evaluate the crystal growth dynamics at a lower time scale, such as 300 ms. Interestingly, this study reveals new perspectives on nucleation formation dynamics where nucleations are captured in motion while forming the single crystal monolayer. The system pressure has been varied from 10 Torr to 150 Torr for 120 W laser power at 950°C furnace temperature, as shown in **Figure 3.15**. Low pressure, such as 10 Torr, captures an underlying network, which conceivably represents moving nucleation trying to form single crystals. As pressure increases, these moving nucleations start to aggregate (50 to 100 Torr) and form single triangular crystals at nominal conditions (150 Torrs). This process is similar to the Ostwald ripening process, where smaller particles are dissolved and connected with larger particles to reach a more thermodynamically stable state so that the surface-to-area ratio can be kept smaller.

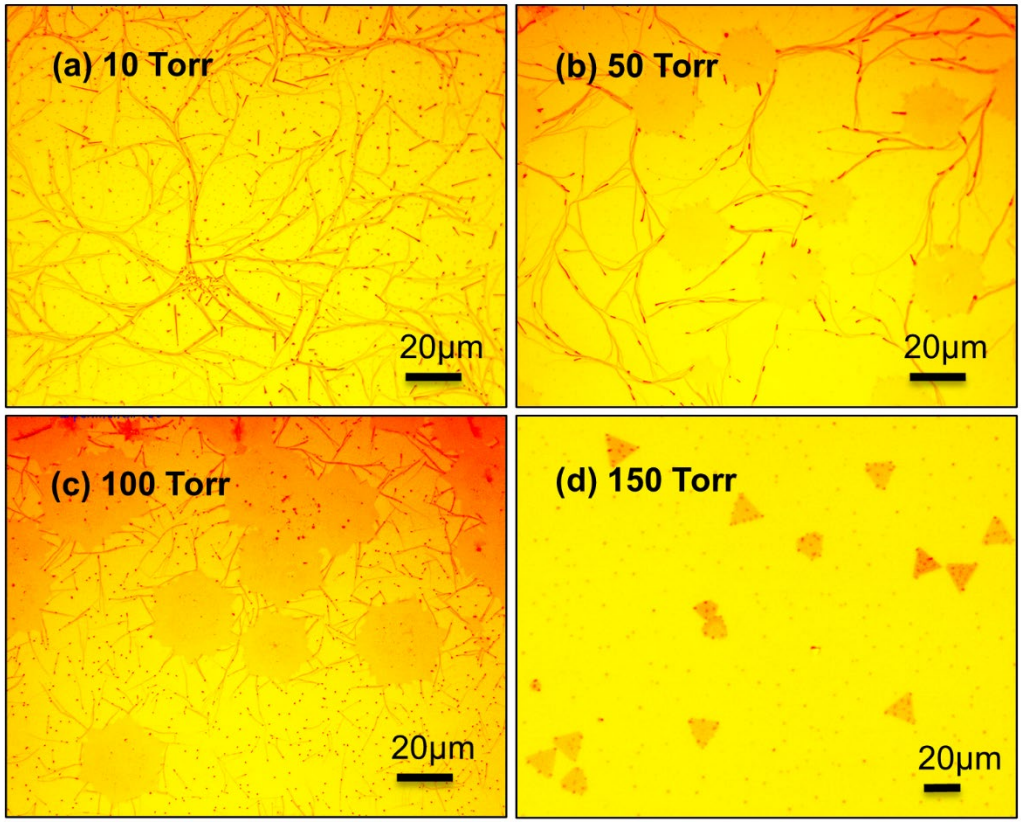

Figure 3.15 impact of pressure at sub-second growth: Optical images of different pressure cases such as 10 Torr, 50 Torr, and 100 Torr show the moving nucleation forming the 2D at 300 ms laser irradiation for 120 W laser power and 950°C furnace temperature.

3.17 Defect Formation at the Lower Time Scale

For ultrafast time-resolved growth, under 500ms, the furnace temperature has been increased beyond 950°C (such as 1000°C and 1050°C) to assist enough flux generation in forming monolayer crystals under such short time scales. Even though single crystal formation was successful in those time scales, defect formation in crystals is prominent in PL measurements, as shown in **Figure 3.16**. The PL red-shifted along with broadened FWHM relative to the pristine conditions shown in **Figure 3.7b.** This variation is attributed to defect formation due to the higher furnace temperature, such as 1000°C and 1050°C, damaging some of the grown crystals in the growth process.

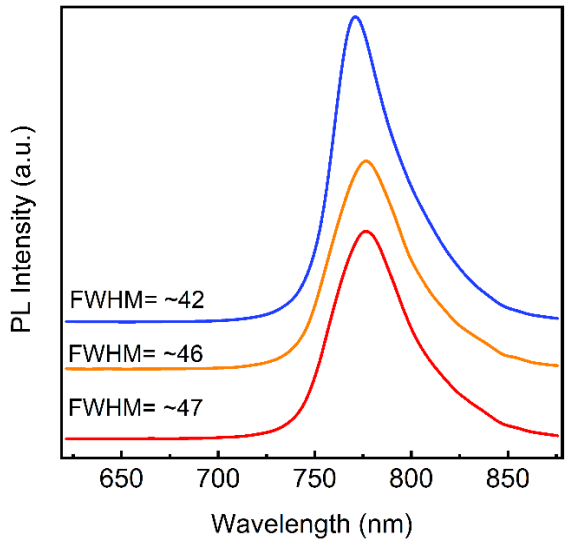

Figure 3.16 PL peak variation below 500 ms growth time at 120W laser power under 1000°C and 1050°C furnace temperature. In these extreme furnace conditions form 30% of defective flakes since the PL was mostly red-shifted, and FWHM became much broader, as shown in the figure.

3.18 Experimental Methods

3.18.1 Time-Resolved Growth of Monolayer WSe_2 on Si/SiO_2

Si/SiO_2 substrate with a thermally grown 250 nm thick oxide layer is used to produce an atomically thin two-dimensional WSe_2 monolayer. Before the experiment, substrates were washed with acetone, methanol, and DI water following standard cleaning procedures. A custom-made graphite crucible with a dimension of $1\times0.6\times0.6$ cm^3 was utilized to facilitate the vaporization of WSe_2 stoichiometric powder. The thickness of the graphite crucible varied from 0.5 mm to 0.3 mm, depending on the experimental design. The graphite crucible was then poured with 10 mg of WSe_2 powder and placed inside the 1-inch furnace tube along with the Si/SO_2 substrate positioned right above the graphite crucible upside-down orientation-maintaining a 2 mm distance between them. The furnace tube maintains the growth dynamics and can be selected at any temperature which is independent of the vaporization condition. One end of the tube furnace is terminated with Zinc Selenide (ZnSe) optical window for a continuous-wave CO_2 laser (λ=10.6 μm) laser beam entry for heating the graphite crucible to vaporize the WSe_2 powder while the other end is connected with a vacuum pump, argon gas inlet, and a pressure gauge. An Arduino Uno (an open-source microcontroller board) was used to turn ON/OFF the laser through a computer program that can control time to the millisecond range (as per as experiment design:10 ms to 5000 ms). After setting all the apparatus as described, the tube furnace was vacuumed down to milli-torr, followed by argon gas purging at 100 SCCM for 4 to 5 minutes to remove all the residual air molecules. Afterward, the tube furnace pressure was adjusted to static 150 Torr by pouring Argon gas, and the furnace temperature was raised as per the experimental design (850°C /900°C /950°C/ 1000°C /1050°C). The trigger signal to the Arduino Uno starts the CO_2 laser and initiates the heating of the graphite crucible. Hence the evaporation of WSe_2 powder starts, which is eventually deposited

on the substrate to form 2D crystals. After finishing the laser irradiation, the furnace lead opened immediately to rapidly cool the system to room temperature while holding the vacuum system functioning.

3.18.2 Temperature Measurement

The Graphite crucible and Silicon substrate temperatures were measured remotely through the quartz tube using the IGA 15 plus pyrometer from LumaSense Technologies. The pyrometer was selected based on the spectral responsivity of the quartz tube's transmission and heat zone temperature range (250 °C to 1800 °C). The temporal response time of the pyrometer is 30 ms. all the measurements are taken 50 cm away from the heat zone with ~5 mm dia spot size for both silicon substrate and graphite crucible. Emissivity was considered as 90 and 71 for the graphite boat and silicon substrate, respectively. The pyrometer calibration was done in the factory and re-evaluated by a built-in furnace thermocouple.

3.18.3 Raman and PL Spectroscopy and Mapping

Optical characterization of the WSe_2 crystals was done by a custom-made Raman and PL spectroscopy and mapping system. A confocal micro design with a 100X microscope objective lens (NA = 0.9) and a 100 nm step size motorized XY stage were used for performing the data acquisition. Horiba HR with a 1200 grooves mm^{-1} grating spectrometer and 532 nm laser excitation source was employed for measurements.

3.19 Summary

Spatiotemporal control of the laser vaporization process was utilized to achieve time-resolved, sub-second, and ultra-fast growth of 2D crystal on Si/SiO_2 substrates. The reduced complexity of growth chemistry via the laser vaporization of stoichiometric powder decoupled control of growth and evaporation and rapid initiation/termination of vapor flux during the growth

process were the critical enabler of this time-resolved approach. The growth technique unfolded two unique features, including the fastest growth rate (100 μm/s) on non-catalytic Si/SiO_2 reported to date and the time-resolved sub-second (10ms) growth of WSe_2 crystals for the first time. The crystal quality assessed through Raman and PL suggested good quality at time scales above 500 ms, and with some PL widening and red-shifted spectra for some samples at shorter time scales (500 ms), possibly due to the insufficient precursor and time for complete growth. Experimental results complemented with simulations showed that shorter growth timescales and faster growth rates could be achieved by enhanced vaporization process using high-power lasers for the vaporization process. This time-resolved technique will be instrumental in revealing the yet-unknown growth kinetics of two-dimensional quantum materials.

CHAPTER 04

BOTTOM-UP VACANCY TAILORING OF TWO-DIMENSIONAL QUANTUM MATERIALS

4.1 Introduction

In this chapter, a novel bottom-up synthesis strategy of LAST has been introduced where compositional inhomogeneities and concentration tunability have been facilitated in a single step using energy and time-controlled laser vaporization of stoichiometric powder in the $MoSe_2$ growth processes. The laser beam was only used to generate and tailor the formation of the vapor flux during the crystal growth. Post-laser or thermal processing on the crystals (i.e., a top-down approach similar to the plasma or electron beam irradiation) has not been performed. Therefore, vacancies are created in this bottom-up approach in a single step. Employing the unique LAST simplified chemistry advantage, instead of using the multicomponent precursor such as Se and MoO_3 used in conventional CVD to produce $MoSe_2$, stoichiometric $MoSe_2$ powder has been utilized to grow monolayer $MoSe_{2-x}$ crystals by controlled laser vaporization of the powder. However, it should be noted that this vacancy tuning capability has facilitated direct heating of the stoichiometric powder by eliminating the use of the graphite boat as a crucible. Depending on the laser power and irradiation time, the vapor can be tailored so that the monolayer crystals with various vacancy concentrations can be uniformly grown on the substrate. Therefore, this technique allows to control of the vaporization and growth processes independently and thus grows monolayer crystals with tailored vacancy levels. Two different routes are investigated, including (i) controlling net energy supplied to the powder by varying laser power and laser irradiation time as well as (ii) confining the vapor to tune the selenium vacancy concentration in the monolayer crystal as they grow. Monolayer $MoSe_{2-x}$ crystals with tunable vacancies ranging from ~1-20%

were successfully synthesized and verified. The samples' atomistic defect densities and corresponding Raman vibrational behaviors were studied under scanning transmission electron microscopy (STEM) and Raman spectroscopy, respectively. Photoluminescence spectroscopy (PL), PL mapping, Raman mapping, atomic force microscopy (AFM), and time-correlated single-photon counting (TCSPC) are among the techniques utilized to assess further the implicit and explicit quality of the vacancies in these samples.

4.2 LAST Features and Vacancy Customization

As demonstrated in **chapter 2,** the laser-assisted synthesis technique (LAST) of 2D materials fundamentally reduces the growth complexity since it directly synthesizes 2D materials from their bulk counterpart, resulting in the growth of contamination-free and high-quality 2D crystals[25]. The uniqueness of this approach is the use of a laser for controlled vaporization of stoichiometric powders and decoupling of the growth from evaporation kinetics. Hence the reproducibility of this synthesis method is much better not only in the same batch of the sample but also from batch to batch. This separate control of growth and vaporization ability further facilitates the customization over the heterogeneity of stoichiometric vapor supply depending on the laser energy absorbed by the powder (i.e., laser power and irradiation time). The critical change introduced here is the direct laser irradiation of the stoichiometric bulk powder instead in direct powder heating with a graphite crucible. At the same time, the secondary customization controllability can be imposed by background pressure which controls the confinement of volumetric vapor flux generated during the laser irradiations of the powder.

4.3 Experimental Setup

In this synthesis approach (**Figure 4.1a**), the growth of 2D $MoSe_{2-x}$ monolayers (**Figure 4.1b**) was carried inside a 1-inch furnace tube where one end is terminated with a zinc selenide

(ZnSe) optical window for laser entrance while the other end is connected to a vacuum pump. A custom-made 45° angled graphite boat having a shallow 1mm deep and 4mm diameter hole in the middle was used to hold stoichiometric $MoSe_2$ powder. This graphite boat was placed in the middle of the furnace tube facing the powder toward the ZnSe optical window for the CO_2 laser ($\lambda = 10.6$ μm) vaporization process[25,161]. A Si/SiO_2 substrate was placed upside down just above the powder to capture the laser-generated vapor flux. The tube furnace was first vacuumed, then the pressure was adjusted to the crystal growth pressure by introducing Ar into the tube (i.e., backfilling the tube to reach the desired pressure and stopping the flow). The furnace was set to the suitable crystal growth temperature to only control the growth kinetics depending on the material's growth requirements. Such independent control of the growth and vaporization enabled the selection of any arbitrary parameters for precise manipulation of growth kinetics. The laser-induced energy coupling was adjusted through laser power and irradiation time. Depending on the absorption properties of the materials, this controllable energy input created tailored vapor flux for the growth of $MoSe_{2-x}$ crystals.

4.4 Design of Experiments

For the systematic study of selenium vacancy creation in the monolayer $MoSe_{2-x}$ crystal as a function of net energy supplied through the laser irradiation, the substrate distance was set to 2 mm above the $MoSe_2$ powder located in a graphite boat, and the growth temperature was set to 700 °C at 500 Torr argon background pressure (based on our previous study) **(Figure 4.1a)**. According to our observation, when pressure was low, the vapor rapidly expanded, and selenium escaped more, as discussed in more detail below. The bulk $MoSe_2$ powder used in this experiment had a particle mesh size of 325. experiments were performed for four different irradiation times such as 0.25s, 1s, 2s, and 5s at each selected laser power, including 20W, 30W, 60W, and 90W

(**Figure 4.2a-d**) to reveal the vacancy formation dynamics in response to the supplied laser energy (i.e., laser power and irradiation time),. The growth conditions mainly produced monolayer triangular crystals. These crystals were around 10-50 microns in size, typically in triangular shapes that were uniformly distributed over the 1.5x1.5 cm^2 substrates (**Figure 4.1b**). Sixteen sets of experiments (4 laser power and 4 irradiation time) were therefore performed, and each condition was repeated at least five times to check the repeatability and reproducibility of the process.

4.5 Direct Laser Heating and Temperature Profile of $MoSe_2$

Figure 4.1c shows the temperature measurement results from the laser-irradiated spot on the stoichiometric $MoSe_2$ powder using a pyrometer. It should be noted that these are average temperature measurements by a pyrometer, and more complex laser materials interaction might happen depending on the absorption coefficient, particle size, porosity, etc. Thus, on average, these profiles indicate the amplitude and time of the temperature rise for each laser power. This is important for understanding the vapor dynamics at each laser heating profile.

As shown in the graph **Figure 4.1c**, the temperature increased rapidly and saturated after a few tens of milliseconds, depending on the laser power. Since the sublimation temperature of the bulk $MoSe_2$ powder is typically >1200 °C[154] (325 mesh-sized powder), the laser power, irradiation time, and pressure impact the vaporization of the powder. For instance, lower laser power and irradiation times, as shown in **Figure 4.1c**, are not sufficient to stoichiometrically evaporate the $MoSe_2$ powder. At these lower temperatures, the selenium tends to escape before the evaporation of Mo or other Mo-Se molecules leading to the growth of selenium-deficient crystals. At higher laser powers, the temperature can reach and go beyond the vaporization temperature leading to more congruent sublimation of Mo and Se atoms. EDS measurement was also performed to study the composition of the vapor by depositing them onto cold substrates **(Figure 4.4)** to confirm this

concept**.** The temperature rises faster at higher laser powers and goes beyond 1200 °C. At these laser powers, selenium escapes during the rising time before the temperature reaches $MoSe_2$ evaporation. Thus at shorter times (<100ms), crystals with more prominent selenium vacancies can grow (since selenium is lost during the rising temperature), and a little longer times (i.e., higher temperatures), more stoichiometric $MoSe_2$ vaporization happens that results in fewer vacancies.

In particular, as observed from **Figure 4.1c**, it is evident from the temperature profile that the heat generated with 20W and 30W are below the vaporization temperatures causing partial and incongruent vaporization of $MoSe_2$, while 60W and 90W generate high enough heat to sublimate the $MoSe_2$ effectively. **Figure 4.1d** schematically illustrates such a vacancy generation concept. The synthesis results for the abovementioned experiments are tabulated in **Figure 4.2**.

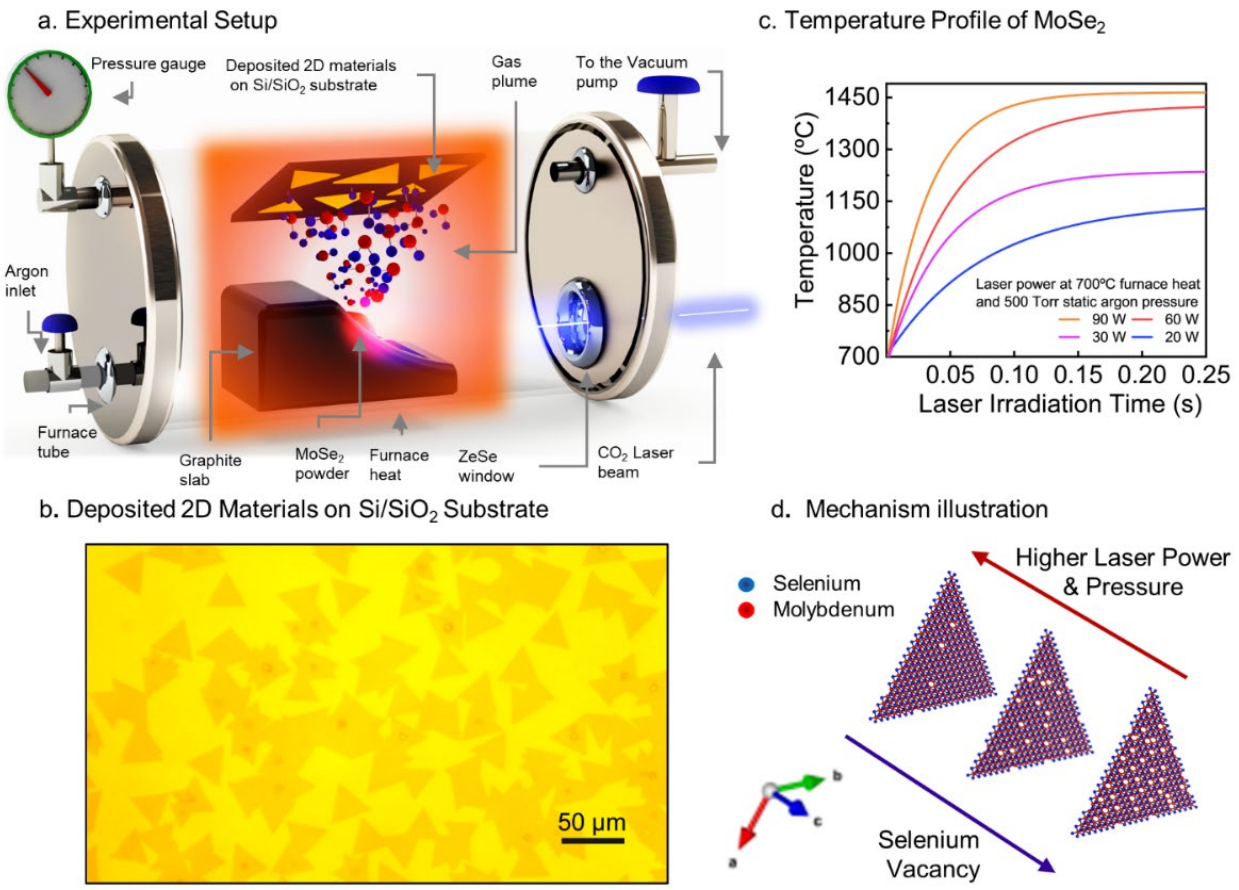

Figure 4.1 Experimental setup for bottom-up vacancy generation in the 2D $MoSe_2$ monolayers grown on Si/SiO_2 substrates. The critical components of the synthesis scheme include a continuous wave CO_2 laser that creates gas flux from stoichiometric bulk precursor powder and a tube furnace, which creates a suitable growth environment (i.e., temperature and pressure) for monolayer crystal growth. Depending on the laser energy supply in terms of various laser irradiation times at different laser power, the amount of laser energy absorption by the stoichiometric bulk precursor powder creates gas flux that contains a diverse degree of inhomogeneity between molybdenum and selenium ($MoSe_{2-x}$), translating to growth of crystal with a distinct amount of selenium vacancies (a). The crystal morphology was captured in an optical microscope showing triangular shapes (b). The temperature profile of the powder while irradiated with different laser powers (c). A pyrometer was used to measure the temperature profile at 700°C furnace temperature and for different laser powers, which tend to saturate after 250ms. Graphically illustrate the vacancy levels in correlation to the pressure and laser energy in the laser-assisted direct vaporization technique (d).

4.6 Probing Defects in Monolayer

There are various methods to study defects in monolayer TMDCs materials, including Raman spectroscopy[162], photoluminescence spectroscopy[163], and transmission electron microscopy.[110, 164] Among these methods, Raman spectroscopy[165] is a simple yet delicate noninvasive method for identifying materials' defects. The quantifiable information on the defect form, concentration, and distribution can be gained from much larger areas of samples using Raman spectroscopy.[166] For example, the disorder in graphene, such as point-like defects, is quantified through defect-activated peaks.[167, 168] Similarly, in one of the monolayer TMDCs defect

studies, LA(M) peak intensity at ~227 cm^{-1} for monolayer MoS_2 has been described as proportional to the density of defects.[169]

4.7 $MoSe_2$ Raman Defect-mode

According to the most reported literature, the defect-free single layer of $MoSe_2$ consists of two prominent Raman peaks at ~ 240 cm^{-1} for A_{1g} mode[157] and at ~ 288 cm^{-1} for E^1_{2g} mode[158]. However, in a $MoSe_2$ vacancy study report, the Se-deficient crystals significantly change the character of the Raman modes. For instance, the A_{1g} mode red-shifts toward ~225 cm^{-1}, while defect-activated peaks emerge at 253 cm^{-1} due to the crystal symmetry breaking[110]. In this study, micro-Raman spectroscopy was, therefore, used to get a general indication of how the phonon modes are influenced by the vacancies and map the uniformity across the crystals. The Raman spectroscopy remarkably revealed the vacancy dynamics of $MoSe_2$ crystals in correlation to the growth parameters, as shown in **Figure 4.2, Figure 4.3,** and **Figure 4.5**. The measurement was performed on a number of crystals in each sample to confirm the uniformity across the substrate. Also, to ensure uniformity across a single crystal, Raman mapping on the crystals was performed **(Figure 4.5c-f).** The results showed excellent uniformity across the sample and across the crystal. STEM further confirmed these, as illustrated in **Section 4.11.3**. These micro-Raman signatures were then correlated to their atomic characteristics obtained from STEM imaging.

4.8 Laser-Based Vacancy Tuning

The Raman modes for the crystals grown with the vaporization conditions described in **Figure 4.1c** show that at 20W and 30W laser powers, the A_{1g} mode is red-shifted, while at 60W and 90W A_{1g} mode primarily goes toward the 240 cm^{-1}. The defect-activated Raman peak intensity remarkably followed the A_{1g} location for all the experimentation, emerging as a vacancy density indicator (D-mode) in terms of the relative intensity variation in conjunction with A_{1g} mode. In

particular, 20W laser power at 0.25s irradiation time (**Figure 4.2a**) gave A_{1g} mode at ~233 cm^{-1} while very prominent D-mode appeared at ~252 cm^{-1} with D/A_{1g} intensity ratio (i.e., I_D/ I_{A1g}) of ~1.33. Further increase of laser irradiation time at 20W laser power, such as 1s, 2s, and 5s, gradually blue-shifted the A_{1g} and settled at ~237 cm^{-1} while the I_D/ I_{A1g} ratio decreased from ~1.33 to ~0.6. Likewise, 30W laser power with analogous irradiation time shows a similar trend as 20W (**Figure 4.2b**). In this case, A_{1g} varied from ~235 cm^{-1} to ~238 $cm^{-1,}$ while the I_D/ I_{A1g} intensity ratio changed from ~0.8 to ~0.5. These two sets of laser energy variation at 20W and 30W with different irradiation times provided clear evidence that stoichiometric deviation between molybdenum and selenium gets narrower as supplied energy increases. This trend was also observed for 60W (**Figure 4.2c**) and 90W (**Figure 4.2d**) until 2 seconds, where A_{1g} mode location continued to blue-shift, and the I_D/I_{A1g} intensity ratio reduced to ~0.32.

Interestingly, for 2-second laser irradiation at 60W laser power, A_{1g} mode reached ~239.2 cm^{-1}, and I_D/ I_{A1g} ratio became very small (~0.32), which is close to the pristine or, more precisely, low vacancy $MoSe_2$ condition according to the reported literature[157]. For radiation beyond 2 seconds at 60W and 90W laser powers, a wider stoichiometric deviation was observed in the crystals as the powder became selenium deficient at prolonged laser irradiation. **Figure 4.2e** and **2f** summarize the Raman spectroscopy results, where **Figure 4.2e** shows A_{1g} Raman mode location while **Figure 4.2f** shows the I_D/ I_{A1g} intensity ratio variation at different laser power and irradiation time.

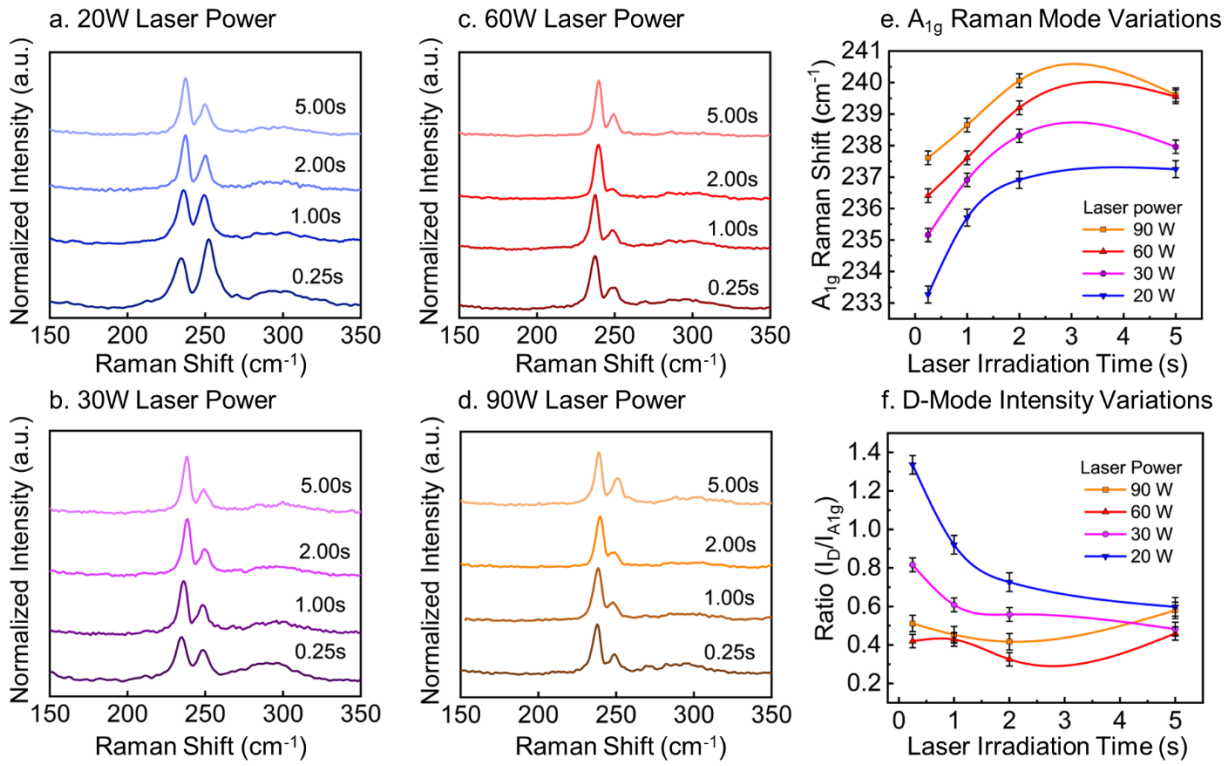

Figure 4.2. Raman spectra of the atomically thin $MoSe_{2-x}$ crystals grown at different laser energies (laser power P = 20W (a), 30W (b), 60W (c), and 90W (d) for different laser irradiation times t = 0.25s, 1s, 2s, and 5s) under constant furnace temperature (700 °C) and background Ar pressure (500 Torr). The graph (a-d) includes out-of-plane Raman vibration mode (A_{1g}) and defect-activated Raman mode (D-mode). In all graphs, the A_{1g} mode is normalized to the same intensities to reveal the D-mode variation visually. In two separate graphs, A_{1g} Raman mode location (e) and D/A_{1g} intensity ratios named I_D/ I_{A1g} ratio (f) are plotted corresponding to the irradiation time at different laser power extracted from the Raman spectra results of the graph (a-d). There are several factors noticeable (i) the A_{1g} mode varies from ~233 cm^{-1} to ~240 cm^{-1} (e), (ii) the I_D/ I_{A1g} intensity ratio varies from 1.33 to 0.32 (f), (iii) 60W laser power and 2s laser irradiation time construct the most intrinsic (Raman shift ~239.2 cm^{-1} and I_D/ I_{A1g} = ~0.32) while 20W laser power and 0.25s laser irradiation time show the most shift from the intrinsic level (Raman shift ~233

cm^{-1} and I_D/ I_{A1g} = ~1.33), and (iv) the 90W laser power I_D/ I_{A1g} becomes worse than the 60W laser power.

4.9 Vacancy Tuning by Background Pressure

Some literature reports the use of overpressure carrier gas that contains chalcogen atoms (e.g., H_2S in the growth MoS_2 crystals)[170] during the cooling time to reduce the uncontrolled chalcogen loss and degradation of crystals. Since there is no carrier gas flow or use of chalcogen-containing gases in this synthesis scheme, and the gas flux emanates solely from the powder, thus the pressure can control the density of the selenium by the degree of spatial confinement of the vapor plume. At low pressures, selenium quickly expands and escapes from the deposition zone, resulting in significant stoichiometric deviation, while higher pressures confine the vapor flux and prevent the divergence between Mo and Se atoms. It should, however, note that higher pressure results in the formation of multilayer flakes.[25]

The growth condition that resulted in the formation of pristine crystals, as found in **Figure 4.2c** (60W laser power, 2S laser irradiation time, 700 C furnace, 500 Torr), was repeated at different pressures such as 70, 100, and 300 Torr to examine the pressure impact. These experiments reveal how the plume expansion creates stoichiometric inhomogeneity, deviates A_{1g} mode from 239.2cm^{-1}, and modulates I_D/I_{A1g} ratio from 0.32 by keeping other parameters constant. **Figure 4.3** shows the experimental results of the pressure impact on Raman (**Figure 4.3**a) and corresponding PL (**Figure 4.3b**) fingerprints. The A_{1g} mode and I_D/ I_{A1g} variation found in **Figure 4.3**a due to pressure variation are summarized in **Figure 4.3c**. Decreasing the pressure red-shifted the A_{1g} mode toward 236.9 $cm^{-1,}$ and at the same time, the I_D/ I_{A1g} ratio increased from 0.32 to 0.535. These results confirmed the interpretation of stoichiometric deviation created by the lower pressures due to the escape of the selenium from the growth zone. The PL peak also showed a

blue-shifted behavior for the 70 Torr (805 nm) than the 500 Torr (810 nm), which is further discussed in the following sections.

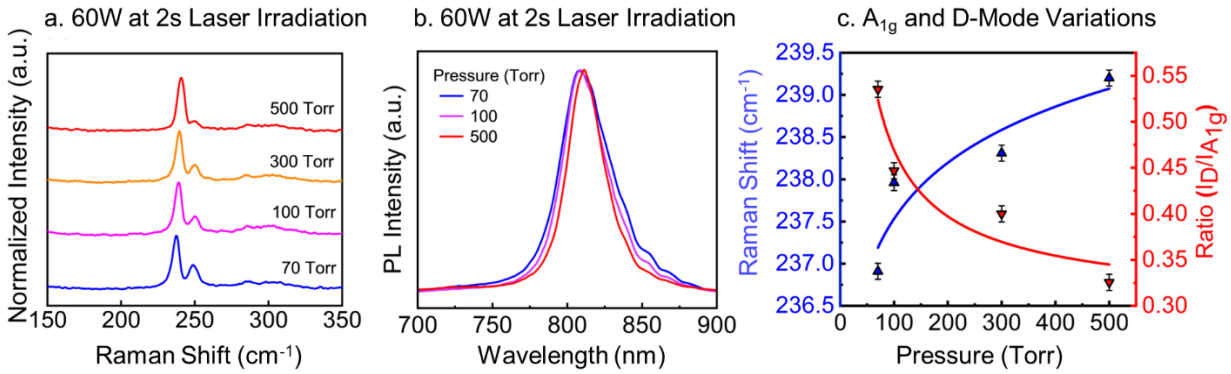

Figure 4.3 Raman and PL spectroscopy result for controlling selenium vacancies on the atomically thin crystals depending on different pressure cases such as 70, 100, 300, and 500 Torr while irradiating the $MoSe_2$ powder at 60W for 2s, which was the best-case scenario for the growth of monolayers with low vacancy levels (A_{1g} = 239.2 cm^{-1} and I_D/ I_{A1g} = 0.32) extracted from **Figure 4.2** (c). The PL spectrum varied from 805 nm to 811 nm for the pressure range of 70 to 500 Torr (b). Since higher pressure confines more selenium in the vapor, increasing pressure from 70 Torr to 500 Torr results in the A_{1g} mode moving from ~236.91 cm^{-1} to ~239.2 cm^{-1} while I_D/ I_{A1g} ratio decreases 0.53 from 0.32, the fitting lines are for guiding eyes (c).

4.10 Vapor Dynamics Analysis

EDS spectroscopy was utilized to analyze the plume and get a figurative idea of how the vapor stoichiometry changes depending on the laser power density. First, the vapor was collected onto cold substrates and performed EDS to confirm the composition of the vapor species. In support of the mechanism explanations, The EDS was performed on the vapor for two different laser energy at room temperatures, such as 120W-s and 30W-s, to see the relative composition of the Mo and Se ratios. The room-temperature vapor collection experiment shows qualitative vapor

composition at different laser energies. At a higher oven temperature, such as 700°C, it should be noted that the volatile Se vapor escapes from the deposition immediately.

On the other hand, most of the released atoms can be collected on the substrate at room temperature vaporization. The qualitative EDS analysis of the collected vapor at room temperature shows that 60W laser power and 2s laser irradiation (120W-s) generate ~3% Mo and ~97% Se (**Figure 4.4**), while 30W-s generate 0% Mo and 100% Se. These results clearly show that Mo vaporization is highly selective to the laser energy than Se atom during laser irradiation of the powder. So for stoichiometric low defect growth of crystals, it needs to ensure that the powder temperature reaches the $MoSe_2$ vaporization temperature as fast as possible to avoid Se loss. At the same time, such dynamics allow us to tune the vaporization temperature with the laser to induce the desired vacancy concentration in crystals intentionally.

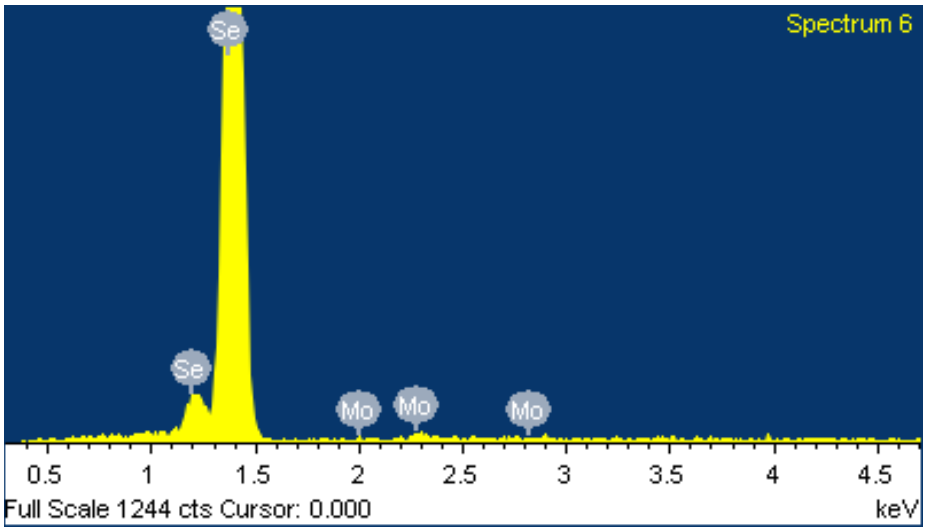

Figure 4.4 Energy Dispersive X-ray Spectroscopy (EDS) of the laser-generated vapor collected on a Si/SiO_2 substrate at room temperature shows the ratio of Se (~97%) to Mo (~3%) in the process when using a 120W-s (2s laser irradiation at 60W) laser irradiation condition. Only selenium is detected at lower laser powers (e.g., 30W).

4.11 Systematic Vacancy Analysis and Characterization

This study's primary characterization of the atomistic vacancy was done by carefully identifying the Raman mode vibration presented in **Figure 4.2**. The color map (**Figure 4.5a** and **b**) and its corresponding bar graphs show both the A_{1g} peak location and the I_D/ I_{A1g} intensity ratio in terms of blue-to the red gradient color for a better visual picture of the vacancy dynamics at different laser power and irradiation time. From the color map, three distinct conditions, including A_{1g} = ~239 cm^{-1}, ~236 cm^{-1}, ~233 cm^{-1} (**Figure 4.5a**) and corresponding I_D/ I_{A1g} ratios of ~0.32, ~0.7, ~1.33 (**Figure 4.5b**) are evident as representative vacancy concentration such as low (pristine), medium, and high vacancy levels, respectively. It should be noted that the quantitative values were derived from atomic STEM imaging and analysis (**Section 4.11.3, Figure 4.8**) and then correlated to their Raman spectra. After this understanding, Raman was chosen as a fast and non-destructive tool for qualitative measurements. For example, low/pristine refers to samples with ~1-2% vacancy, medium refers to samples with ~9-10%, and high refers to samples with ~18-20% vacancy levels qualitatively.

4.11.1 Raman Mapping

Raman mapping was performed to monitor the areal uniformity of the vacancy distributions across the crystals. **Figure 4.5c** shows all the spectra obtained for each map (**Figure 4.5d-f**), including the triangular crystals and their surroundings. As expected, no $MoSe_2$ Raman signal comes from the crystal's surroundings, while the A_{1g} and D-modes can be clearly seen on the triangular crystals. The intensity of the spectra in the maps shows that the vacancy distribution is uniform throughout the crystals. For more details investigation, AFM (tropology), photoluminescence (PL) spectroscopy and PL mapping, time-correlated single-photon counting

(TCSPC), and scanning tunneling electron microscopy (STEM) were utilized to check the crystal quality as a function of different vacancy concentrations, as shown in **Figure 4.6** and **Figure 4.7**.

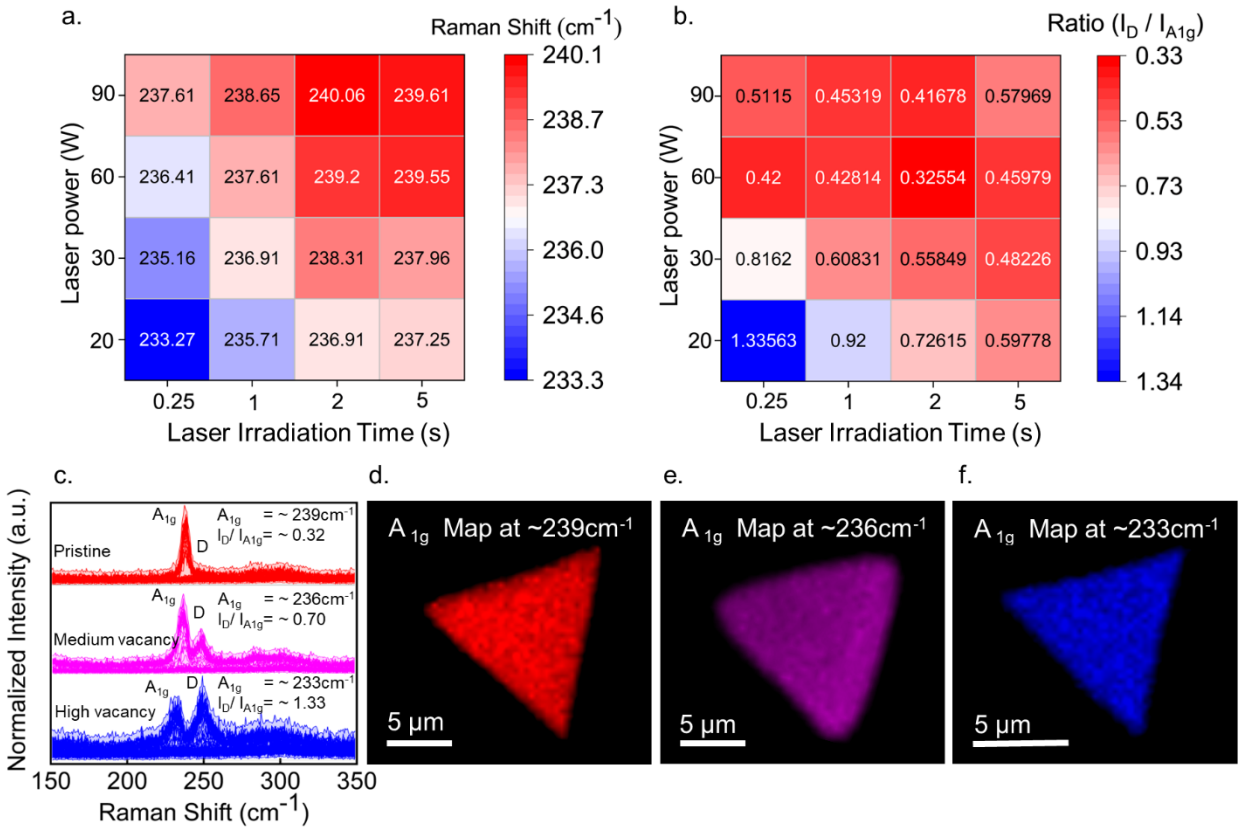

Figure 4.5 The experimental process maps show the A_{1g} mode peak location (a) and the I_D/ I_{A1g} ratios (b) with blue to red gradient color for a better visual picture of the defect dynamics for different laser power and irradiation time. From the color map, three distinct representative conditions were selected and, for simplicity, labeled as pristine (i.e., A_{1g} = ~239cm^{-1}, I_D/ I_{A1g} = ~0.32), medium vacancy (i.e., A_{1g} = ~236cm^{-1}, I_D/ I_{A1g} = ~0.7) and high vacancy (i.e., A_{1g} = ~233cm^{-1}, I_D/ I_{A1g} = ~1.33). The cumulative Raman spectra (c) of the maps obtained from the triangular crystals and their surroundings show the uniformity and homogeneity of the vacancy distribution across the crystals.

4.11.2 Photoluminescence Spectroscopy

First, the photoluminescence (PL) spectroscopy measurements (**Figure 4.6b**) of three conditions corresponding to the representative Raman spectra (**Figure 4.6a**) confirmed that the layers were indeed monolayer as $MoSe_2$ shows indirect band[9] to direct band transition[158] when thinned down from bulk to monolayer. The monolayer nature of the samples was further confirmed with AFM, as shown in **Figure 4.6g**. The PL peak of the high vacancy condition showed a blue shift (801nm) in PL emission compared to the pristine condition (811nm). A slight shoulder was also noticeable in most PL measurements near 720 nm for crystals with Se vacancy that could be attributed to the B exciton, which is typically insignificant at the room-temperature PL measurements. The low-temperature PL[44] for revealing the exciton dynamics is subject to future study. The corresponding PL mapping of these three conditions (**Figures 4.6d**,**e**,**f**) showed excellent uniformity throughout the crystals, similar to their Raman map behavior. Such vacancy tuning capability can broaden the potential use of TMDCs for photonics, quantum optics, and valleytronics applications[171]. Reports have shown that defects impact the exciton dynamics of neutral excitons[43] by providing additional relaxation channels[172]. Another study reported that defect-bound excitons exhibit a much longer valley lifetime[171], and the prolonged PL lifetime[41] is also attributed to defects for reducing exciton–exciton annihilation (EEA) in monolayer WS_2.[118] The lifetime[173] measurement in our study showed similar dynamics. The defective conditions displayed a more extended decay time than the pristine condition, as shown in **Figure 4.6c**.

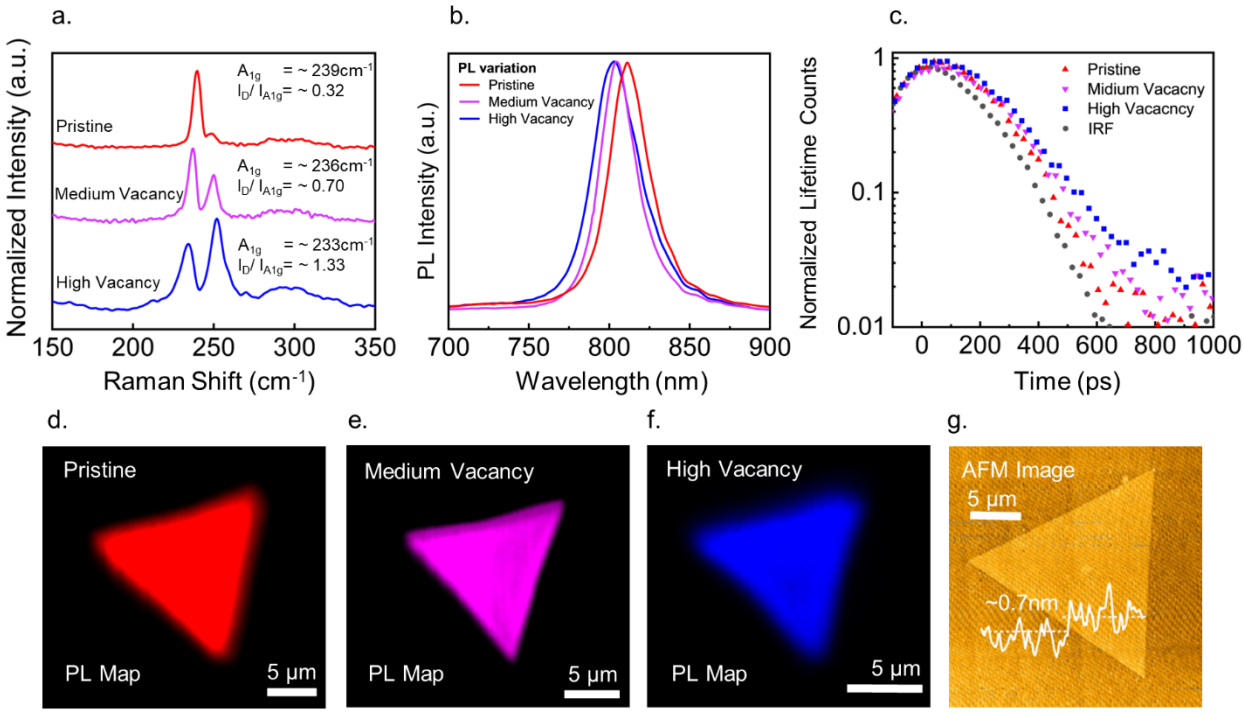

Figure 4.6. The three chosen defect density cases with high, medium, and pristine conditions according to their Raman A_{1g} mode location: 233 (blue), 236 (purple), 239.2 (red), and corresponding I_D/ I_{A1g} rations 1.33, 0.7, and 0.32(a). Corresponding PL spectra of these cases show higher vacancy concentration is blue-shifted compared to the pristine condition (b). TCSPC measurements show that the pristine crystals display a relatively shorter decay time relative to the higher selenium vacancy conditions; also, the decay time is directly correlated with the vacancy concentration, i.e., higher vacancy levels have longer decay time and vice versa (c). PL mapping for pristine (red), medium (purple), and high (blue) vacancy concentrations crystals show good uniformity across the crystals (d, e, f). AFM image of a monolayer crystal confirms the high structural quality and monolayer thickness (0.7 nm) of a representative single-layer crystal (g).

4.11.3 Vacancy Quantification

Atomic resolution imaging using STEM plays an essential role in identifying the defect type and quantifying the vacancy concentration.[118, 174] The STEM study was designed based on

the **Figure 4.6a** conditions to reveal physical properties as the function of vacancy concentrations where **Figure 4.7a**,**b**,**c** correspond to samples with low, medium, and high vacancy concentrations, respectively. **Figure 4.7** consists of three separate high-angle annular dark-field (HAADF) STEM images where the hexagonal lattice of the $MoSe_2$ structure can be seen. From these images, three different intensity sites can be seen, with the highest intensity being sites with two Se atoms, followed by Mo atoms, and then single Se atoms. The single Se sites result in the clearly seen low-intensity triangular areas within the lattice seen in **Figure 4.7**. According to the results, the occurrence of the single-selenium vacancy (V_{Se}) was highly dominant over the double-selenium (V_{2Se}) and the molybdenum vacancies (V_{Mo}) in our samples. Careful analysis of the vacancy concentration indicated that the samples with low (A_{1g}=239.2cm^{-1}, **Figure 4.7a**), intermediate (A_{1g}=236cm^{-1}, **Figure 4.7b**), and high (A_{1g}=233cm^{-1}, **Figure 4.7c**) vacancy levels, had vacancies in ~ 2.5 ± 0.6 %, ~ 12.7 ± 1.0 % and ~ 19.5 ± 4.0 % of the X_2 sites within the $MoSe_2$ structure, respectively. The defect quantification method[175] and statics are also presented (**Section 4.12**, **Figure 4.8**, and **4.9**). These results were remarkably in agreement with the Raman, PL, and TCSPC measurements which shows the promise of our bottom-up synthesis method for accurately generating atomistic vacancy levels in monolayer $MoSe_2$ crystals.

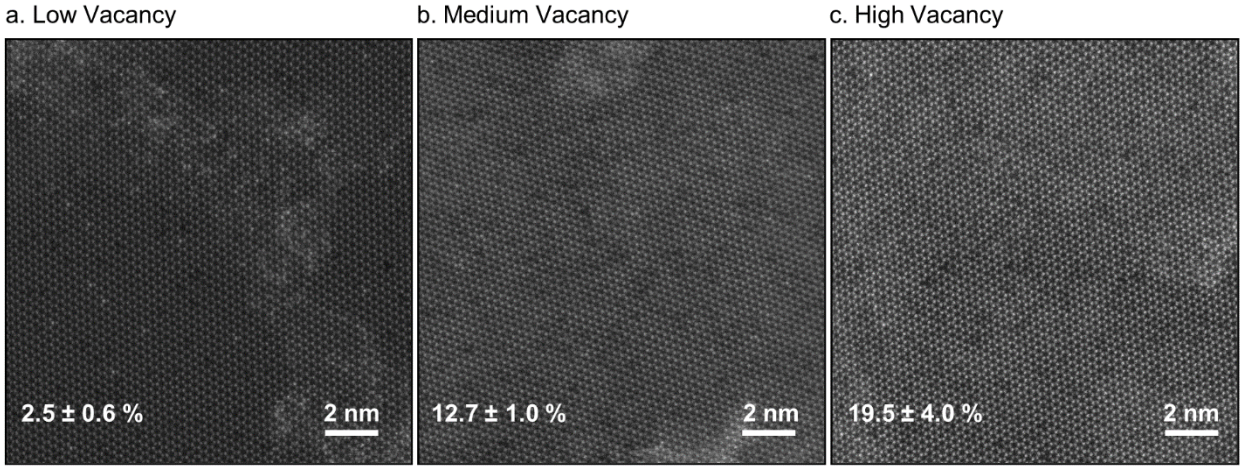

Figure 4.7. STEM images of the samples with various vacancy levels are shown at the atomic scale. The majority of the vacancy type are single-selenium vacancies (V_{Se}), with a few cases of double-selenium vacancies (V_{2Se}). Careful analysis of the vacancy concentrations shows that the samples with low (A_{1g}=239.2cm^{-1}, a), intermediate (A_{1g}=236cm^{-1}, b), and high (A_{1g}=233cm^{-1}, c) vacancy levels have about ~ 2.5 ± 0.6 %, ~ 12.7 ± 1.0 %, and ~ 19.5 ± 4.0 % vacancies, respectively. Bright contrast areas on the surface of the samples result from amorphous PMMA residue from the sample transfer process.

4.12 Vacancy Type Recognition and Estimation Algorithm

Defect concentration analysis was performed using an adaptation of a python-based algorithm from a study by Susarla et al.[175] An example of the defect concentration analysis is seen in **Figure 4.8.** Initial atom count was performed using Gaussian filtering to find the local maximum within the HAADF-STEM images in **Figure 4.8a**, with the associated histogram of the initial atom count plotted as a function of the relative intensity in **Figure 4.8d**. The histogram is then curve-fit to a tri-gaussian function with the three curves associated with the Mo, Se_2, and Se sites (**Figures 4.8 b** and **e**). From the atomic number (*Z*-)contrast, the brightest and dimmest curves are matched to the Se_2 and Se sites (red) and the common mid-range intensity curve associated with the Mo sites (yellow). The atoms within the now split histograms (**Figure 4.8f**) are then counted and plotted in **Figure 4.8c**, with the X sites now split into the Se_2 (red) and Se (blue) sites and the Mo sites (green). **Table 4.1** displays the results from this atom identification and counting. This table shows the estimated total of V_{Se} within several example images from the different samples discussed in **Figure 4.7**. The defect density was defined as the ratio of the number of V_{Se} and V_{2Se} over the total number of Se sites within the field of view. The average over several images was similar to previously found defect concentration estimations.

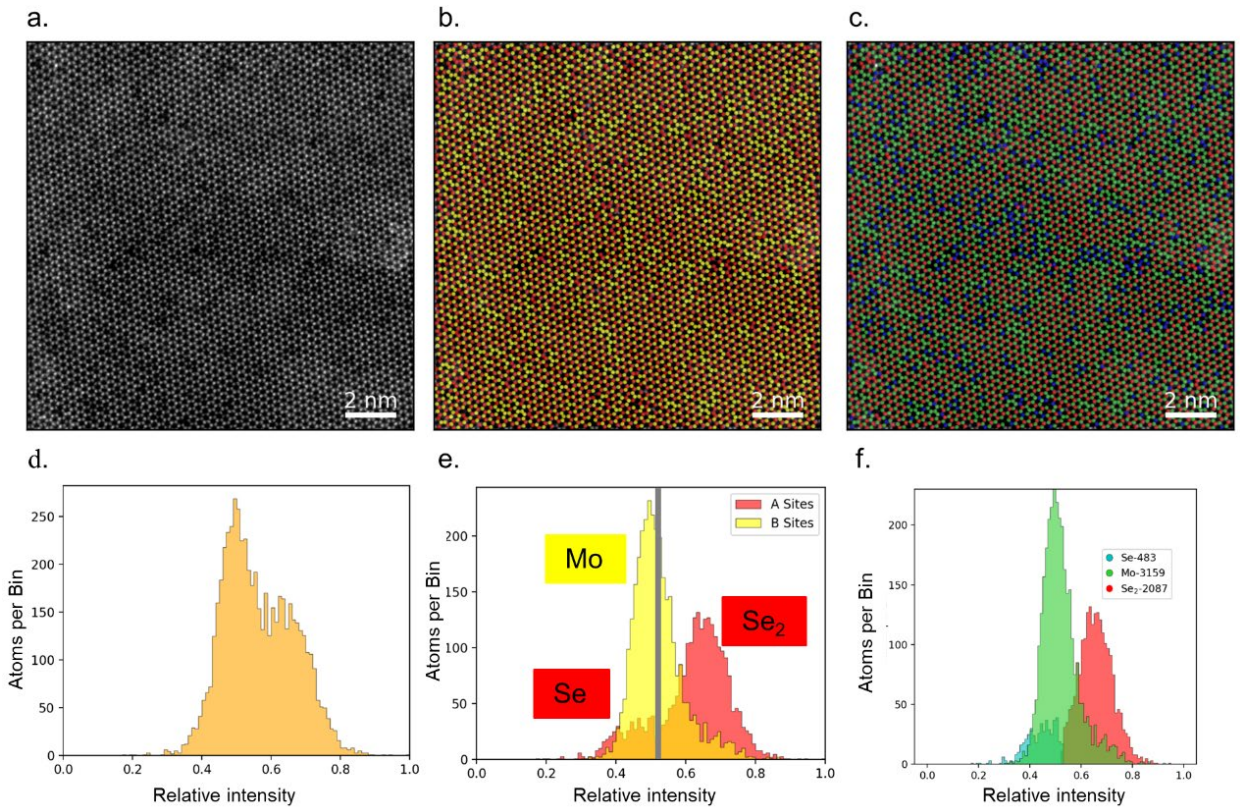

Figure 4.8 An example of the three steps of the defect estimate procedure is shown. Image (a) shows the HAADF-STEM scan of the high defect concentration $MoSe_2$ monolayer, image (b) represents the split of M (red) and X2 (yellow) sites, and image (c) represents the split to base component sites (Mo = green, Se_2 = red, Se = blue) and counts the found atom sites. The corresponding atom counting histogram as a function of the relative intensity analysis of images a, b, and c are presented in terms of initial raw atom count (d), M and X component analysis split (e), and final atom counting (f).

More than three images were analyzed to confirm the validity of the density estimation to develop the statistics. The following table shows the overall statistics derived from the HAADF-STEM images in this study, where the A, B, and C correspond to three distinct conditions discussed in **Figure 4.7.**

Table 4.1. Defect quantification statistics derived from HAADF-STEM images

Images	Number of Se Defects	Defect Density (%)	Average Defect Density
A1	111	3.25	2.5 ± 0.6 %
A2	55	1.69	
A3	83	2.52	
B1	322	12.10	12.7 ± 1.0 %
B2	326	11.23	
B3	386	13.76	
B4	431	13.82	
B5	384	12.45	
C1	701	23.5	19.5 ± 4.0 %
C2	382	14.5	
C3	491	19.1	
C4	437	15.4	
C5	582	23.7	
C6	325	24.4	
C7	478	16.2	

4.13 Vacancy Level as a Function of Laser Energy

The vacancy level found in the STEM images in **Section 4.11.3** and their analysis in **Section 4.12** enables a correlation with the laser energy supplied, which is shown in **Figure 4.9**. It demonstrates the atomistic vacancy tuning capability with the LAST system with precise accuracy.

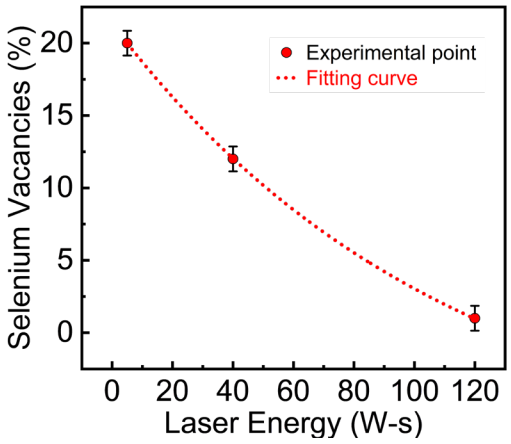

Figure 4.9. The selenium vacancy levels quantified from the STEM analysis shown as a function of laser energy demonstrate the proposed method's controllability.

4.14 Experimental Methods

4.14.1 Vacancy Formation Process

$MoSe_2$ flakes with different vacancy concentrations were synthesized by direct laser vaporization of stoichiometric bulk $MoSe_2$ powder purchased from Alfa Aesar with 99.9% percent of purity and 325 mesh size. 2D monolayer crystals were grown on Si/SiO_2 substrates with 250 nm of a thermal oxide layer. Before starting the growth, these substrates were washed with acetone, methanol, and DI-water to remove contaminants by following the standard cleaning procedures. The evaporation of the stoichiometric bulk powder was performed by placing the powder in a custom-made 45° angle faced graphite holder with a cylinder-shaped hole (1mm deep and 4mm diameter). After placing the $MoSe_2$ powder in the hole, the graphite holder was placed inside a 1-inch tube furnace with one side connected to the vacuum pump and the other to a Zinc Selenide (ZnSe) optical window for the CO_2 laser beam entry. Inside the tube, the graphite boat was directed toward the optical window in a way that the continuous-wave CO_2 laser with 10.6 μm wavelength can directly irradiate the powder through the ZnSe optical window. Since our tube furnace was 1 inch in diameter (Thermo Scientific Lindberg/Blue M Mini-Mite 1100 ºC Tube Furnace), small Si/SiO_2 substrates (~1.5cm X 2cm) were used for the crystals' growth. The Si/SiO_2 substrates were placed upside down 2 mm above the powder boat. Before the synthesis, the tube furnace was vacuumed to a few millitorrs, followed by several minutes of Ar purging to remove the remaining air molecules. Argon gas was just used to fill the tube and reach the desired static background pressure environment, and then the gas flow was immediately stopped. The furnace temperature was set constant to 700 ℃ throughout the experiments to maintain the growth temperature. After

adjusting the tube furnace temperature and pressure, irradiating $MoSe_2$ powder with the CO_2 laser began the synthesis process. According to the experimental design procedure, different laser powers, laser irradiation times, and pressures were used to synthesize samples with various vacancy levels. Soon after switching off the laser, the furnace lid opened instantly to allow the samples to cool down naturally while keeping the vacuum system active.

4.14.2 Materials Used in Experiments

The $MoSe_2$ was purchased from Alfa Aesar with the following specifications:

Table 4.2 Materials Details of Vacancy Study

Material	Molecular formula	Product Number	Molecular weight	Mesh size	Purity (%)
Molybdenum (IV) selenide	$MoSe_2$	13112	253.87	325	99.9%

4.14.3 Raman and PL Spectroscopy and Mapping

Raman and photoluminescence (PL) measurements and PL mapping were performed using a custom-made system with a laser excitation source of 532 nm. A Horiba HR spectrometer with 1,800 grooves/mm grating was used for the Raman spectra, while 300 grooves/mm grating was employed for the PL measurements. The presented data were captured using a 100X objective microscope lens (NA = 0.9) in a confocal micro configuration, and for Raman and PL mapping, a motorized XY stage with a 100 nm step size was utilized.

4.14.4 TCSPC Measurement

PL lifetime measurement was done using a time-correlated single-photon counting (TCSPC) technique with a picosecond 405 nm excitation source and a repetition frequency of 8 MHz. This TCSPC system was attached to the above spectroscopy system as well. A picosecond

photon detection module (PVD-900) from Horiba was used with a spectral response between 230-920nm range and dark current counts <3000 cps.

4.14.5 Temperature Measurement

While the CO_2 laser was heating the $MoSe_2$ powder, the temperature was measured directly through the quartz tube using a pyrometer at a 50 cm distance with a measuring spot size of ~4mm in diameter. In this case, the IGA 15 plus pyrometer from LumaSense Technologies was used for the temperature measurement (range: 250 °C to 1800 °C), which spectral responsivity consistent with the quartz tube transmission range. The built-in tube furnace thermocouple verified the pyrometer's manufacturer calibration for the reliability of the remote temperature measurement.

4.14.6 AFM Measurement

An HR-AFM Workshop system with a 0.3 Hz scan rate and 512 resolution was used for AFM imaging in the noncontact mode. The Gwyddion software was used for AFM data processing and analysis.

4.14.7 STEM Sample Preparation

The samples with monolayer triangular flakes on the Si/SiO_2 substrate were first spin-coated with Poly (methyl methacrylate, PMMA) for transferring the flake to the TEM grids. Rotating the spin coater at 3000 rpm for 45 s created a thin layer of PMMA on the Si/SiO_2 substrate. The PMMA/flake films were then cured at 100 °C for 15 minutes. Subsequently, a 20% KOH solution at 90 °C was used to detach the PMMA/flake films from the substrate. The separated PMMA/flake films were transferred to DI water to remove KOH residue. In the next step, these PMMA/flake films were placed onto the Quantifoil TEM grids and cured at 100 °C for 5 min. In the end, to remove PMMA from the 2D flake sitting on the TEM grid, samples were submerged into the acetone for 10min at 60 °C.

4.14.8 STEM Characterization

An aberration-corrected Nion UltraSTEM 100, operated at 60kV with a spatial resolution capable of ~1 Å was used for all electron microscopy experiments. High-angle annular dark-field (HAADF) STEM images were collected using a convergence angle of 31 mrad and a collection angle between 86 and 200 mrad. Samples were kept in an inert environment before being loaded onto fixed-tilt specimen holders for an 8-hour, 160ºC vacuum bake process before imaging. Defect concentration analysis was performed after data acquisition and is further discussed in section 4.12.

4.15 Summary

This work uses a novel single-step bottom-up synthesis method to tune the chalcogen atomic vacancy concentrations by tailoring the vaporization of stoichiometric powders to induce $MoSe_{2-x}$ growth, where x was tuned by laser energy and pressure confinement in the growth process. The key novelty arises from the localized direct and time-controlled heating of the $MoSe_2$ stoichiometric powder ranging from a few tens of milliseconds to seconds and the capability to control the confinement of the vapor by the background pressure. In addition, the unique advantages of the laser-assisted synthesis techniques, such as separate control of growth and vaporization kinetics, reduction of contamination due to the absence of other species except for the stoichiometric powder, no use of the carrier or reducing gases, and no mixing chemistry made this synthesis technique a feasible solution for controlled defect engineering in 2D materials. Systematic experimentation was performed by varying laser power, irradiation time, and pressure to synthesize different vacancy concentrations, and numerous characterization techniques such as Raman and photoluminescence spectroscopy, time-correlated photon counting, atomic force microscopy, optical microscopy have been employed to validate the merit of the method. It was

observed that the amount of selenium vacancy followed a parabolic curve potentially due to low laser energy absorption by the powder at the beginning, and as the source became selenium-deficient over time, it created a unique gradient of compositional inhomogeneity in terms of different laser irradiation time at each laser power. The vacancy concentrations were estimated optically using Raman spectroscopy and validated atomistically using STEM imaging and analysis, showing tunable selenium vacancy levels ranging from ~1 to 20%. The results from this work will enable the controlled vacancy engineering in 2D material that potentially allows enhanced interaction of gasses and molecules with 2D materials for possible gas and bio-sensing applications.

Note. This chapter is a slightly modified version of Nurul Azam et al." Laser-Assisted Synthesis of Monolayer 2D MoSe2 Crystals with Tunable Vacancy Concentrations: Implications for Gas and Biosensing." ACS Applied Nano Materials 5, no. 7 (2022): 9129-9139. Copyright 2022 American Chemical Society.

CHAPTER 05

CONCLUSION

This comprehensive study introduced several original findings to resolve the pressing research bottleneck of the emerging field of 2D materials. Firstly, this study introduced a new method of laser-based synthesis of quantum materials that presents a simple yet general approach capable of accelerating the synthesis and discovery of 2D quantum materials. The quality of the grown crystals by this approach shows superior crystallinity along with free of contamination. Secondly, The spatiotemporal control of the laser vaporization unlocks the time-resolved, sub-second, and ultra-fast growth of 2D crystal on the non-catalytic substrate such as Si/SiO_2 substrates for the first time. It should be noted that these capabilities are highly scalable with the use of a powerful laser. Thirdly, The utilization of direct laser energy absorption mechanisms by the bulk stoichiometric powder reveals a new area of creating control vacancy with atomic precision, which has many novel applications, including quantum spintronics, gas sensor, biosensors, and numerous others. This multi-facet novel laser-based synthesis technique introduces new controllability during the synthesis, which has been discussed in more detail in the following sections as concluding remarks on each result.

Overall, this first study of laser-assisted synthesis and time-resolved growth control of two-dimensional TMDC materials introduces many new capabilities that are otherwise unavailable. Hence results of this work will be instrumental to the border field of condensed matter physics to develop further understanding or discovery of new science and technologies.

5.1 Laser-Based 2D Quantum Materials Synthesis

In this study, a universal laser-assisted synthesis technique (LAST) for growing a large number of 2D materials directly from stoichiometric powders has been introduced and established. This technique offers a significantly simplified growth mode that eliminates the existing complexities, such as uncontrolled gas-phase reactions and flow dynamics in the current gas-phase growth methods. This method has demonstrated a novel way to decouple the evaporation of stoichiometric powders from their 2D growth temperatures by a selective laser irradiation process. Due to high vaporization temperatures of stoichiometric TMDC powders (e.g., ~1400 ºC for MoS_2) compared to their growth temperature (e.g., ~850 ºC for MoS_2), the use of stoichiometric powders in current CVD systems has not been considered or possible. For selective laser heating, a graphite boat was utilized as a crucible to prevent stoichiometric deviation and uncontrolled vaporization. The indirect selective heating of these stoichiometric powders through laser heating of graphite crucible developed a unique set of synthesis statics that enables predictability to synthesize new 2D materials that are not facilitated in other synthesis strategies. The use of a selective laser heating process allows efficient decoupling of the evaporation and growth processes enabling the growth of a large number of 2D materials directly from their stoichiometric powders. This laser-assisted approach also offered rapid heating, evaporation, and growth as well as cooling and termination control in the system. For selective laser heating, a graphite boat was utilized as a crucible to prevent stoichiometric deviation and uncontrolled vaporization. The indirect selective heating of these stoichiometric powders through laser heating of graphite crucible developed a unique set of synthesis statics that enables predictability to synthesize new 2D materials that are not facilitated in other synthesis strategies. The universality of this laser-assisted approach was verified by growing various TMDC material systems, including monolayer MoS_2, WS_2, $MoSe_2$, and WSe_2

crystals as big as 100 microns. Widely 2D characterization methods such as optical imaging, atomic force microscopy (AFM), transmission electron microscopy (TEM), as well as Raman and photoluminescence (PL) mapping and spectroscopy measurements, confirm the exceptionally high quality of the grown crystal.

5.2 Laser-Based Ultrafast Sub-Second Growth of 2D Quantum Materials

The reduced complexity of growth chemistry via the laser vaporization of stoichiometric powder decoupled control of growth and evaporation and rapid initiation/termination of vapor flux during the growth process further enables the time-resolved growth strategies for 2D materials for the first time. Key system parameters, such as thinner graphite boats, furnace heat, and laser power, are identified to enhance feedstock supply and maximize surface diffusion. In this process, the new forms of growth technique unfolded two unique features, including the fastest growth rate (100 μm/s) on non-catalytic Si/SiO_2 reported to date and the time-resolved sub-second (10ms) growth of WSe_2 crystals for the first time. The crystal quality assessed through Raman and PL suggested good quality at time scales above 500 ms, and with some PL widening and redshifted spectra for some samples at shorter time scales (500 ms), possibly due to the insufficient precursor and time for complete growth. Experimental results complemented with simulations showed that enhanced vaporization by high-power lasers could achieve shorter growth timescales and faster growth rates. This time-resolved technique will be instrumental in revealing the yet-unknown growth kinetics of two-dimensional quantum materials.

5.3 Laser-Based Vacancy Tunning of 2D Quantum Materials

This laser-based synthesis technique further introduces a novel single-step bottom-up synthesis method to tune the chalcogen atomic vacancy concentrations by tailoring the vaporization of stoichiometric powders to induce $MoSe_{2-x}$ growth, where x was tuned by laser

energy and pressure confinement in the growth process. The key novelty arises from the localized direct and time-controlled heating of the $MoSe_2$ stoichiometric powder ranging from a few tens of milliseconds to seconds and the capability to control the confinement of the vapor by the background pressure. This vacancy tuning scheme utilizes all the unique advantages of the laser-assisted synthesis techniques (LAST), such as separate control of growth and vaporization kinetics, reduction of contamination due to the absence of other species except for the stoichiometric powder, no use of the carrier or reducing gases, and no mixing chemistry made this synthesis technique a feasible solution for controlled defect engineering in 2D materials. The only difference from the previous two results in this study, which enables the vacancy tuning capability, is eliminating the indirect heating through the graphite crucible. Systematic experimentation was performed by varying laser power, irradiation time, and pressure to synthesize different vacancy concentrations, and numerous characterization techniques such as Raman and photoluminescence spectroscopy, time-correlated photon counting, atomic force microscopy, optical microscopy have been employed to validate the merit of the method. It was observed that the amount of selenium vacancy followed a parabolic curve potentially due to low laser energy absorption by the powder at the beginning, and as the source became selenium-deficient over time, it created a unique gradient of compositional inhomogeneity in terms of different laser irradiation time at each laser power. The vacancy concentrations were estimated optically using Raman spectroscopy and validated atomistically using STEM imaging and analysis, showing tunable selenium vacancy levels ranging from ~1 to 20%. The results from this work will enable the controlled vacancy engineering in 2D material that potentially allows enhanced interaction of gasses and molecules with 2D materials for possible gas and bio-sensing applications.

FUTURE WORKS

Every successful synthesis scheme of materials enables new capabilities and furthers the development of new technologies. For example, the mechanical exfoliation method established 2D materials as a reality and unleashed countless new technologies and opportunities. Similarly, this laser-assisted synthesis technique provides unique capabilities that are not common in existing synthesis methods. In the following, future work based on this study has been discussed.

1. Discovery of new 2D materials: The LAST can be utilized to discover new 2D materials using unique capabilities offered by the LAST. In general, having solid forms of stoichiometric layered powder materials is the only prerequisite for eligibility in this synthesis strategy.
2. Phase engineering of the 2D materials: Rapid cooling of the growth area and temporal and localized control of this system's flux generation/ termination capabilities can be the critical enabler to lock different meta phases that evolved during the crystal's growth.
3. Revealing in-situ growth kinetics: The temporal and localized control of the LAST simplified the system overhead. The proper instrumentation design can unleash the in-situ growth kinetics in real-time using the synthesis dynamics control knowledge achieved in this study.
4. Machine learning integration: The synthesis parameters of the LAST are highly co-related to the atomistic nature of the precursor materials. In addition, the use of graphite boats as crucible enables to development of a synthesis ladder because of the decoupling of the laser absorption kinetics. For the simplified nature of LAST, the machine learning algorithm

will aid in optimizing the parameters for known materials and finding the synthesis parameters of unknown materials with the correct training data set.

5. Growing 2D on functional substrates: LAST can be used to produce 2D on functional substrates, such as magnetic substrates, to explore novel physics at the interface.

REFERENCES

1. Tiwari, J. N.; Tiwari, R. N.; Kim, K. S., Zero-dimensional, one-dimensional, two-dimensional and three-dimensional nanostructured materials for advanced electrochemical energy devices. *Progress in Materials Science* **2012,** *57* (4), 724-803.

2. Jeevanandam, J.; Barhoum, A.; Chan, Y. S.; Dufresne, A.; Danquah, M. K., Review on nanoparticles and nanostructured materials: history, sources, toxicity and regulations. *Beilstein Journal of Nanotechnology* **2018,** *9*, 1050-1074.

3. Pokropivny, V. V.; Skorokhod, V. V., Classification of nanostructures by dimensionality and concept of surface forms engineering in nanomaterial science. *Materials Science and Engineering: C* **2007,** *27* (5-8), 990-993.

4. Manzeli, S.; Ovchinnikov, D.; Pasquier, D.; Yazyev, O. V.; Kis, A., 2D transition metal dichalcogenides. *Nature Reviews Materials* **2017,** *2* (8).

5. Pospischil, A.; Mueller, T., Optoelectronic Devices Based on Atomically Thin Transition Metal Dichalcogenides. *Applied Sciences* **2016,** *6* (3).

6. Mahjouri-Samani, M.; Lin, M.-W.; Wang, K.; Lupini, A. R.; Lee, J.; Basile, L.; Boulesbaa, A.; Rouleau, C. M.; Puretzky, A. A.; Ivanov, I. N.; Xiao, K.; Yoon, M.; Geohegan, D. B., Patterned arrays of lateral heterojunctions within monolayer two-dimensional semiconductors. *Nature Communications* **2015,** *6*, 7749.

7. Akinwande, D.; Brennan, C. J.; Bunch, J. S.; Egberts, P.; Felts, J. R.; Gao, H.; Huang, R.; Kim, J.-S.; Li, T.; Li, Y.; Liechti, K. M.; Lu, N.; Park, H. S.; Reed, E. J.; Wang, P.; Yakobson, B. I.; Zhang, T.; Zhang, Y.-W.; Zhou, Y.; Zhu, Y., A review on mechanics and mechanical properties of 2D materials—Graphene and beyond. *Extreme Mechanics Letters* **2017,** *13*, 42-77.

8. Novoselov, K. S.; Geim, A. K.; Morozov, S. V.; Jiang, D.; Zhang, Y.; Dubonos, S. V.; Grigorieva, I. V.; Firsov, A. A., Electric Field Effect in Atomically Thin Carbon Films. *Science* **2004,** *306* (5696), 666-669.

9. Geim, A. K.; Novoselov, K. S., The rise of graphene. *Nature Materials* **2007,** *6* (3), 183-191.

10. Lin, Z.; McCreary, A.; Briggs, N.; Subramanian, S.; Zhang, K.; Sun, Y.; Li, X.; Borys, N. J.; Yuan, H.; Fullerton-Shirey, S. K.; Chernikov, A.; Zhao, H.; McDonnell, S.; Lindenberg, A. M.; Xiao, K.; LeRoy, B. J.; Drndić, M.; Hwang, J. C. M.; Park, J.; Chhowalla, M.; Schaak, R. E.; Javey, A.; Hersam, M. C.; Robinson, J.; Terrones, M., 2D materials advances: from large scale synthesis and controlled heterostructures to improved characterization techniques, defects and applications. *2D Materials* **2016,** *3* (4), 042001.

11. Dagdeviren, C.; Yang, B. D.; Su, Y.; Tran, P. L.; Joe, P.; Anderson, E.; Xia, J.; Doraiswamy, V.; Dehdashti, B.; Feng, X.; Lu, B.; Poston, R.; Khalpey, Z.; Ghaffari, R.; Huang, Y.; Slepian, M. J.; Rogers, J. A., Conformal piezoelectric energy harvesting and storage from motions of the heart, lung, and diaphragm. *Proceedings of the National Academy of Sciences of the United States of America* **2014,** *111* (5), 1927-1932.

12. Du, L.; Hasan, T.; Castellanos-Gomez, A.; Liu, G.-B.; Yao, Y.; Lau, C. N.; Sun, Z., Engineering symmetry breaking in 2D layered materials. *Nature Reviews Physics* **2021,** *3* (3), 193-206.

13. Gerstner, E., Nobel Prize 2010: Andre Geim & Konstantin Novoselov. *Nature Physics* **2010,** *6* (11), 836-836.

14. Phiri, J.; Gane, P.; Maloney, T. C., General overview of graphene: Production, properties and application in polymer composites. *Materials Science and Engineering: B* **2017,** *215*, 9-28.

15. It's still all about graphene. *Nature Materials* **2010,** *10* (1), 1-1.

16. Mannix, A. J.; Kiraly, B.; Hersam, M. C.; Guisinger, N. P., Synthesis and chemistry of elemental 2D materials. *Nature Reviews Chemistry* **2017,** *1* (2).

17. Döscher, H.; Schmaltz, T.; Neef, C.; Thielmann, A.; Reiss, T., Graphene Roadmap Briefs (No. 2): industrialization status and prospects 2020. *2D Materials* **2021,** *8* (2).

18. Service, R. F., Beyond graphene. *Science* **2015,** *348* (6234), 490-492.

19. Novoselov, K. S.; Fal′ko, V. I.; Colombo, L.; Gellert, P. R.; Schwab, M. G.; Kim, K., A roadmap for graphene. *Nature* **2012,** *490* (7419), 192-200.

20. Balog, R.; Jørgensen, B.; Nilsson, L.; Andersen, M.; Rienks, E.; Bianchi, M.; Fanetti, M.; Lægsgaard, E.; Baraldi, A.; Lizzit, S.; Sljivancanin, Z.; Besenbacher, F.; Hammer, B.; Pedersen, T. G.; Hofmann, P.; Hornekær, L., Bandgap opening in graphene induced by patterned hydrogen adsorption. *Nature Materials* **2010,** *9* (4), 315-319.

21. Schwierz, F., Graphene Transistors: Status, Prospects, and Problems. *Proceedings of the IEEE* **2013,** *101* (7), 1567-1584.

22. Xia, F.; Farmer, D. B.; Lin, Y.-m.; Avouris, P., Graphene Field-Effect Transistors with High On/Off Current Ratio and Large Transport Band Gap at Room Temperature. *Nano Letters* **2010,** *10* (2), 715-718.

23. Gao, J.; Luo, X.; Fang, F.; Sun, J., Fundamentals of atomic and close-to-atomic scale manufacturing: a review. *International Journal of Extreme Manufacturing* **2021,** *4* (1).

24. Xia, F.; Wang, H.; Xiao, D.; Dubey, M.; Ramasubramaniam, A., Two-dimensional material nanophotonics. *Nature Photonics* **2014,** *8* (12), 899-907.

25. Azam, N.; Ahmadi, Z.; Yakupoglu, B.; Elafandi, S.; Tian, M.; Boulesbaa, A.; Mahjouri-Samani, M., Accelerated synthesis of atomically-thin 2D quantum materials by a novel laser-assisted synthesis technique. *2D Materials* **2019,** *7* (1).

26. Song, X.; Hu, J.; Zeng, H., Two-dimensional semiconductors: recent progress and future perspectives. *Journal of Materials Chemistry C* **2013,** *1* (17).

27. Ahmadi, Z.; Yakupoglu, B.; Azam, N.; Elafandi, S.; Mahjouri-Samani, M., Self-limiting laser crystallization and direct writing of 2D materials. *International Journal of Extreme Manufacturing* **2019,** *1* (1), 015001.

28. Chhowalla, M.; Shin, H. S.; Eda, G.; Li, L.-J.; Loh, K. P.; Zhang, H., The chemistry of two-dimensional layered transition metal dichalcogenide nanosheets. *Nature Chemistry* **2013,** *5* (4), 263-275.

29. Digital transfer growth of patterned 2D metal chalcogenides by confined nanoparticle evaporation. *ACS Nano* **2014,** *8*, 11567.

30. Ahmed, S.; Yi, J., Two-Dimensional Transition Metal Dichalcogenides and Their Charge Carrier Mobilities in Field-Effect Transistors. *Nano-Micro Letters* **2017,** *9* (4).

31. Chaves, A.; Azadani, J. G.; Alsalman, H.; da Costa, D. R.; Frisenda, R.; Chaves, A. J.; Song, S. H.; Kim, Y. D.; He, D.; Zhou, J.; Castellanos-Gomez, A.; Peeters, F. M.; Liu, Z.; Hinkle, C. L.; Oh, S.-H.; Ye, P. D.; Koester, S. J.; Lee, Y. H.; Avouris, P.; Wang, X.; Low, T., Bandgap engineering of two-dimensional semiconductor materials. *npj 2D Materials and Applications* **2020,** *4* (1).

32. Das, S.; Robinson, J. A.; Dubey, M.; Terrones, H.; Terrones, M., Beyond Graphene: Progress in Novel Two-Dimensional Materials and van der Waals Solids. *Annual Review of Materials Research* **2015,** *45* (1), 1-27.

33. Mir, S. H.; Yadav, V. K.; Singh, J. K., Recent Advances in the Carrier Mobility of Two-Dimensional Materials: A Theoretical Perspective. *ACS Omega* **2020,** *5* (24), 14203-14211.

34. Rawat, A.; Jena, N.; Dimple, D.; De Sarkar, A., A comprehensive study on carrier mobility and artificial photosynthetic properties in group VI B transition metal dichalcogenide monolayers. *Journal of Materials Chemistry A* **2018,** *6* (18), 8693-8704.

35. Wang, Q. H.; Kalantar-Zadeh, K.; Kis, A.; Coleman, J. N.; Strano, M. S., Electronics and optoelectronics of two-dimensional transition metal dichalcogenides. *Nature Nanotechnology* **2012,** *7* (11), 699-712.

36. Sun, Y.; Wang, D.; Shuai, Z., Indirect-to-Direct Band Gap Crossover in Few-Layer Transition Metal Dichalcogenides: A Theoretical Prediction. *The Journal of Physical Chemistry C* **2016,** *120* (38), 21866-21870.

37. Zhang, Y.; Chang, T.-R.; Zhou, B.; Cui, Y.-T.; Yan, H.; Liu, Z.; Schmitt, F.; Lee, J.; Moore, R.; Chen, Y.; Lin, H.; Jeng, H.-T.; Mo, S.-K.; Hussain, Z.; Bansil, A.; Shen, Z.-X., Direct observation of the transition from indirect to direct bandgap in atomically thin epitaxial MoSe2. *Nature Nanotechnology* **2013,** *9* (2), 111-115.

38. Elafandi, S.; Christiansen, R.; Azam, N.; Cichon, M.; Park, M.; Hamilton, M. C.; Mahjouri-Samani, M., Monolayer 2D quantum materials subjected to gamma irradiation in high-vacuum for nuclear and space applications. *Applied Physics Letters* **2020,** *116* (21).

39. Ezgi Eroglu, Z.; Contreras, D.; Bahrami, P.; Azam, N.; Mahjouri-Samani, M.; Boulesbaa, A., Filling Exciton Trap-States in Two-Dimensional Tungsten Disulfide (WS2) and Diselenide (WSe2) Monolayers. *Nanomaterials* **2021,** *11* (3).

40. Chen, R.; Li, Y.-C.; Cai, J.-M.; Cao, K.; Lee, H.-B.-R., Atomic level deposition to extend Moore's law and beyond. *International Journal of Extreme Manufacturing* **2020,** *2* (2).

41. Jiang, J.; Xu, T.; Lu, J.; Sun, L.; Ni, Z., Defect Engineering in 2D Materials: Precise Manipulation and Improved Functionalities. *Research* **2019,** *2019*, 1-14.

42. Hunter, N.; Azam, N.; Zobeiri, H.; Wang, R.; Mahjouri-Samani, M.; Wang, X., Interfacial Thermal Conductance between Monolayer WSe2 and SiO2 under Consideration of Radiative Electron–Hole Recombination. *ACS Applied Materials & Interfaces* **2020,** *12* (45), 51069-51081.

43. Eroglu, Z. E.; Comegys, O.; Quintanar, L. S.; Azam, N.; Elafandi, S.; Mahjouri-Samani, M.; Boulesbaa, A., Ultrafast dynamics of exciton formation and decay in two-dimensional tungsten disulfide (2D-WS2) monolayers. *Physical Chemistry Chemical Physics* **2020,** *22* (30), 17385-17393.

44. Huang, X.; Li, Z.; Liu, X.; Hou, J.; Kim, J.; Forrest, S. R.; Deotare, P. B., Neutralizing Defect States in MoS2 Monolayers. *ACS Applied Materials & Interfaces* **2021,** *13* (37), 44686-44692.

45. Fathi-Hafshejani, P.; Azam, N.; Wang, L.; Kuroda, M. A.; Hamilton, M. C.; Hasim, S.; Mahjouri-Samani, M., Two-Dimensional-Material-Based Field-Effect Transistor Biosensor for Detecting COVID-19 Virus (SARS-CoV-2). *ACS Nano* **2021,** *15* (7), 11461-11469.

46. Mondal, N.; Azam, N.; Gartstein, Y. N.; Mahjouri-Samani, M.; Malko, A. V., Photoexcitation Dynamics and Long-Lived Excitons in Strain-Engineered Transition Metal Dichalcogenides. *Advanced Materials* **2022,** *34* (23).

47. Graphene is not alone. *Nature Nanotechnology* **2012,** *7* (11), 683-683.

48. Liu, C.; Chen, H.; Wang, S.; Liu, Q.; Jiang, Y.-G.; Zhang, D. W.; Liu, M.; Zhou, P., Two-dimensional materials for next-generation computing technologies. *Nature Nanotechnology* **2020,** *15* (7), 545-557.
49. Sebastian, A.; Pendurthi, R.; Choudhury, T. H.; Redwing, J. M.; Das, S., Benchmarking monolayer MoS2 and WS2 field-effect transistors. *Nature Communications* **2021,** *12* (1).

50. Liu, X.; Hersam, M. C., 2D materials for quantum information science. *Nature Reviews Materials* **2019,** *4* (10), 669-684.

51. Ahn, E. C., 2D materials for spintronic devices. *npj 2D Materials and Applications* **2020,** *4* (1), 17.

52. Lin, X.; Yang, W.; Wang, K. L.; Zhao, W., Two-dimensional spintronics for low-power electronics. *Nature Electronics* **2019,** *2* (7), 274-283.

53. Schaibley, J. R.; Yu, H.; Clark, G.; Rivera, P.; Ross, J. S.; Seyler, K. L.; Yao, W.; Xu, X., Valleytronics in 2D materials. *Nature Reviews Materials* **2016,** *1* (11).

54. Rasmussen, F. A.; Thygesen, K. S., Computational 2D Materials Database: Electronic Structure of Transition-Metal Dichalcogenides and Oxides. *The Journal of Physical Chemistry C* **2015,** *119* (23), 13169-13183.

55. Anichini, C.; Czepa, W.; Pakulski, D.; Aliprandi, A.; Ciesielski, A.; Samorì, P., Chemical sensing with 2D materials. *Chemical Society Reviews* **2018,** *47* (13), 4860-4908.

56. Jiang, H.; Zheng, L.; Liu, Z.; Wang, X., Two-dimensional materials: From mechanical properties to flexible mechanical sensors. *InfoMat* **2019,** *2* (6), 1077-1094.

57. Ma, Q.; Ren, G.; Xu, K.; Ou, J. Z., Tunable Optical Properties of 2D Materials and Their Applications. *Advanced Optical Materials* **2020,** *9* (2).

58. Feynman, R. P. In *Plenty of Room at the Bottom*, APS annual meeting, 1959.

59. Frisenda, R.; Niu, Y.; Gant, P.; Muñoz, M.; Castellanos-Gomez, A., Naturally occurring van der Waals materials. *npj 2D Materials and Applications* **2020,** *4* (1), 38.

60. Brent, J. R.; Savjani, N.; O'Brien, P., Synthetic approaches to two-dimensional transition metal dichalcogenide nanosheets. *Progress in Materials Science* **2017,** *89*, 411-478.

61. Splendiani, A.; Sun, L.; Zhang, Y. B.; Li, T. S.; Kim, J.; Chim, C. Y.; Galli, G.; Wang, F., Emerging Photoluminescence in Monolayer MoS2. *Nano Letters* **2010,** *10* (4), 1271-1275.

62. Mak, K. F.; Lee, C.; Hone, J.; Shan, J.; Heinz, T. F., Atomically ThinMoS2: A New Direct-Gap Semiconductor. *Physical Review Letters* **2010,** *105* (13).

63. Mahjouri-Samani, M.; Gresback, R.; Tian, M.; Wang, K.; Puretzky, A. A.; Rouleau, C. M.; Eres, G.; Ivanov, I. N.; Xiao, K.; McGuire, M. A.; Duscher, G.; Geohegan, D. B., Pulsed Laser Deposition of Photoresponsive Two-Dimensional GaSe Nanosheet Networks. *Advanced Functional Materials* **2014,** *24* (40), 6365-6371.
64. McCreary, K. M.; Hanbicki, A. T.; Jernigan, G. G.; Culbertson, J. C.; Jonker, B. T., Synthesis of Large-Area WS2 monolayers with Exceptional Photoluminescence. *Scientific Reports* **2016,** *6* (1).

65. Akkanen, S. T. M.; Fernandez, H. A.; Sun, Z., Optical Modification of 2D Materials: Methods and Applications. *Advanced Materials* **2022,** *34* (19).

66. Shen, J.; He, Y.; Wu, J.; Gao, C.; Keyshar, K.; Zhang, X.; Yang, Y.; Ye, M.; Vajtai, R.; Lou, J.; Ajayan, P. M., Liquid Phase Exfoliation of Two-Dimensional Materials by Directly Probing and Matching Surface Tension Components. *Nano Letters* **2015,** *15* (8), 5449-5454.

67. Zhan, Y.; Liu, Z.; Najmaei, S.; Ajayan, P. M.; Lou, J., Large-Area Vapor-Phase Growth and Characterization of MoS2Atomic Layers on a SiO2Substrate. *Small* **2012,** *8* (7), 966-971.

68. Dumcenco, D.; Ovchinnikov, D.; Marinov, K.; Lazić, P.; Gibertini, M.; Marzari, N.; Sanchez, O. L.; Kung, Y.-C.; Krasnozhon, D.; Chen, M.-W.; Bertolazzi, S.; Gillet, P.; Fontcuberta i Morral, A.; Radenovic, A.; Kis, A., Large-Area Epitaxial Monolayer MoS2. *ACS Nano* **2015,** *9* (4), 4611-4620.

69. Cwik, S.; Mitoraj, D.; Reyes, O. M.; Rogalla, D.; Peeters, D.; Kim, J.; Schutz, H. M.; Bock, C.; Beranek, R.; Devi, A., Direct Growth of MoS2 and WS2 Layers by Metal Organic Chemical Vapor Deposition. *Adv Mater Interfaces* **2018,** *5* (16).

70. Yu, J. X.; Li, J.; Zhang, W. F.; Chang, H. X., Synthesis of high quality two-dimensional materials via chemical vapor deposition. *Chem Sci* **2015,** *6* (12), 6705-6716.

71. Zhou, J.; Lin, J.; Huang, X.; Zhou, Y.; Chen, Y.; Xia, J.; Wang, H.; Xie, Y.; Yu, H.; Lei, J.; Wu, D.; Liu, F.; Fu, Q.; Zeng, Q.; Hsu, C.-H.; Yang, C.; Lu, L.; Yu, T.; Shen, Z.; Lin, H.; Yakobson, B. I.; Liu, Q.; Suenaga, K.; Liu, G.; Liu, Z., A library of atomically thin metal chalcogenides. *Nature* **2018,** *556* (7701), 355-359.

72. Fu, D. Y.; Zhao, X. X.; Zhang, Y. Y.; Li, L. J.; Xu, H.; Jang, A. R.; Yoon, S. I.; Song, P.; Poh, S. M.; Ren, T. H.; Ding, Z.; Fu, W.; Shin, T. J.; Shin, H. S.; Pantelides, S. T.; Zhou, W.; Loh, K. P., Molecular Beam Epitaxy of Highly Crystalline Monolayer Molybdenum Disulfide on Hexagonal Boron Nitride. *J Am Chem Soc* **2017,** *139* (27), 9392-9400.

73. Mahjouri-Samani, M.; Tian, M.; Wang, K.; Boulesbaa, A.; Rouleau, C. M.; Puretzky, A. A.; McGuire, M. A.; Srijanto, B. R.; Xiao, K.; Eres, G.; Duscher, G.; Geohegan, D.

B., Digital Transfer Growth of Patterned 2D Metal Chalcogenides by Confined Nanoparticle Evaporation. *Acs Nano* **2014,** *8* (11), 11567-11575.

74. Mahjouri-Samani, M.; Gresback, R.; Tian, M. K.; Wang, K.; Puretzky, A. A.; Rouleau, C. M.; Eres, G.; Ivanov, I. N.; Xiao, K.; McGuire, M. A.; Duscher, G.; Geohegan, D. B., Pulsed Laser Deposition of Photoresponsive Two-Dimensional GaSe Nanosheet Networks. *Advanced Functional Materials* **2014,** *24* (40), 6365-6371.
75. Serna, M. I.; Yoo, S. H.; Moreno, S.; Xi, Y.; Oviedo, J. P.; Choi, H.; Alshareef, H. N.; Kim, M. J.; Minary-Jolandan, M.; Quevedo-Lopez, M. A., Large-Area Deposition of MoS2 by Pulsed Laser Deposition with In Situ Thickness Control. *ACS Nano* **2016,** *10* (6), 6054-6061.

76. Serrao, C. R.; Diamond, A. M.; Hsu, S. L.; You, L.; Gadgil, S.; Clarkson, J.; Carraro, C.; Maboudian, R.; Hu, C. M.; Salahuddin, S., Highly crystalline MoS2 thin films grown by pulsed laser deposition. *Applied Physics Letters* **2015,** *106* (5).

77. Elafandi, S.; Ahmadi, Z.; Azam, N.; Mahjouri-Samani, M., Gas-Phase Formation of Highly Luminescent 2D GaSe Nanoparticle Ensembles in a Nonequilibrium Laser Ablation Process. *Nanomaterials* **2020,** *10* (5), 908.

78. Azam, N.; Boebinger, M. G.; Jaiswal, S.; Unocic, R. R.; Fathi-Hafshejani, P.; Mahjouri-Samani, M., Laser-Assisted Synthesis of Monolayer 2D MoSe2 Crystals with Tunable Vacancy Concentrations: Implications for Gas and Biosensing. *ACS Applied Nano Materials* **2022,** *5* (7), 9129-9139.

79. Cai, Z.; Liu, B.; Zou, X.; Cheng, H.-M., Chemical Vapor Deposition Growth and Applications of Two-Dimensional Materials and Their Heterostructures. *Chemical Reviews* **2018,** *118* (13), 6091-6133.

80. Yu, J.; Hu, X. Z.; Li, H. Q.; Zhou, X.; Zhai, T. Y., Large-scale synthesis of 2D metal dichalcogenides. *Journal of Materials Chemistry C* **2018,** *6* (17), 4627-4640.

81. Roy, A.; Movva, H. C. P.; Satpati, B.; Kim, K.; Dey, R.; Rai, A.; Pramanik, T.; Guchhait, S.; Tutuc, E.; Banerjee, S. K., Structural and Electrical Properties of MoTe2 and MoSe2 Grown by Molecular Beam Epitaxy. *ACS Applied Materials & Interfaces* **2016,** *8* (11), 7396-7402.

82. Briggs, N.; Subramanian, S.; Lin, Z.; Li, X.; Zhang, X.; Zhang, K.; Xiao, K.; Geohegan, D.; Wallace, R.; Chen, L.-Q.; Terrones, M.; Ebrahimi, A.; Das, S.; Redwing, J.; Hinkle, C.; Momeni, K.; van Duin, A.; Crespi, V.; Kar, S.; Robinson, J. A., A roadmap for electronic grade 2D materials. *2D Materials* **2019,** *6* (2).

83. Yang, L.; Xie, C.; Jin, J.; Ali, R.; Feng, C.; Liu, P.; Xiang, B., Properties, Preparation and Applications of Low Dimensional Transition Metal Dichalcogenides. *Nanomaterials* **2018,** *8* (7).

84. Zhang, Z.; Chen, P.; Yang, X.; Liu, Y.; Ma, H.; Li, J.; Zhao, B.; Luo, J.; Duan, X.; Duan, X., Ultrafast growth of large single crystals of monolayer WS2 and WSe2. *National Science Review* **2020,** *7* (4), 737-744.

85. Gao, Y.; Liu, Y.; Liu, Z., Controllable growth of two-dimensional materials on noble metal substrates. *iScience* **2021,** *24* (12).

86. Ji, Q.; Zhang, Y.; Zhang, Y.; Liu, Z., Chemical vapour deposition of group-VIB metal dichalcogenide monolayers: engineered substrates from amorphous to single crystalline. *Chemical Society Reviews* **2015,** *44* (9), 2587-2602.

87. Gao, Y.; Hong, Y.-L.; Yin, L.-C.; Wu, Z.; Yang, Z.; Chen, M.-L.; Liu, Z.; Ma, T.; Sun, D.-M.; Ni, Z.; Ma, X.-L.; Cheng, H.-M.; Ren, W., Ultrafast Growth of High-Quality Monolayer WSe2 on Au. *Advanced Materials* **2017,** *29* (29).

88. Zhang, L.; Dong, J.; Ding, F., Strategies, Status, and Challenges in Wafer Scale Single Crystalline Two-Dimensional Materials Synthesis. *Chemical Reviews* **2021,** *121* (11), 6321-6372.

89. Liu, B.; Fathi, M.; Chen, L.; Abbas, A.; Ma, Y.; Zhou, C., Chemical Vapor Deposition Growth of Monolayer WSe2with Tunable Device Characteristics and Growth Mechanism Study. *ACS Nano* **2015,** *9* (6), 6119-6127.

90. Choudhury, T. H.; Zhang, X.; Al Balushi, Z. Y.; Chubarov, M.; Redwing, J. M., Epitaxial Growth of Two-Dimensional Layered Transition Metal Dichalcogenides. *Annual Review of Materials Research* **2020,** *50* (1), 155-177.

91. Xu, X.; Zhang, Z.; Qiu, L.; Zhuang, J.; Zhang, L.; Wang, H.; Liao, C.; Song, H.; Qiao, R.; Gao, P.; Hu, Z.; Liao, L.; Liao, Z.; Yu, D.; Wang, E.; Ding, F.; Peng, H.; Liu, K., Ultrafast growth of single-crystal graphene assisted by a continuous oxygen supply. *Nature Nanotechnology* **2016,** *11* (11), 930-935.

92. Lu, J.; Carvalho, A.; Chan, X. K.; Liu, H.; Liu, B.; Tok, E. S.; Loh, K. P.; Castro Neto, A. H.; Sow, C. H., Atomic Healing of Defects in Transition Metal Dichalcogenides. *Nano Letters* **2015,** *15* (5), 3524-3532.

93. Lin, Z.; Carvalho, B. R.; Kahn, E.; Lv, R.; Rao, R.; Terrones, H.; Pimenta, M. A.; Terrones, M., Defect engineering of two-dimensional transition metal dichalcogenides. *2D Materials* **2016,** *3* (2).

94. Konar, R.; Tamari, R.; Teblum, E.; Nessim, G. D.; Meshi, L., In-depth characterization of stacking faults forming during the growth of Transition-Metal Di-Chalcogenides (TMDCs) by ambient pressure-CVD. *Materials Characterization* **2022,** *184*.

95. Liang, Q.; Zhang, Q.; Zhao, X.; Liu, M.; Wee, A. T. S., Defect Engineering of Two-Dimensional Transition-Metal Dichalcogenides: Applications, Challenges, and Opportunities. *ACS Nano* **2021,** *15* (2), 2165-2181.

96. Lee, J.; Heo, J.; Lim, H. Y.; Seo, J.; Kim, Y.; Kim, J.; Kim, U.; Choi, Y.; Kim, S. H.; Yoon, Y. J.; Shin, T. J.; Kang, J.; Kwak, S. K.; Kim, J. Y.; Park, H., Defect-Induced in Situ Atomic Doping in Transition Metal Dichalcogenides via Liquid-Phase Synthesis toward Efficient Electrochemical Activity. *ACS Nano* **2020,** *14* (12), 17114-17124.

97. Aharonovich, I.; Englund, D.; Toth, M., Solid-state single-photon emitters. *Nature Photonics* **2016,** *10* (10), 631-641.

98. Robinson, J. A.; Schuler, B., Engineering and probing atomic quantum defects in 2D semiconductors: A perspective. *Applied Physics Letters* **2021,** *119* (14).

99. Barthelmi, K.; Klein, J.; Hötger, A.; Sigl, L.; Sigger, F.; Mitterreiter, E.; Rey, S.; Gyger, S.; Lorke, M.; Florian, M.; Jahnke, F.; Taniguchi, T.; Watanabe, K.; Zwiller, V.; Jöns, K. D.; Wurstbauer, U.; Kastl, C.; Weber-Bargioni, A.; Finley, J. J.; Müller, K.; Holleitner, A. W., Atomistic defects as single-photon emitters in atomically thin MoS2. *Applied Physics Letters* **2020,** *117* (7).

100. Azzam, S. I.; Parto, K.; Moody, G., Prospects and challenges of quantum emitters in 2D materials. *Applied Physics Letters* **2021,** *118* (24).

101. Zhang, X.; Gao, L.; Yu, H.; Liao, Q.; Kang, Z.; Zhang, Z.; Zhang, Y., Single-Atom Vacancy Doping in Two-Dimensional Transition Metal Dichalcogenides. *Accounts of Materials Research* **2021,** *2* (8), 655-668.

102. Shu, H.; Zhou, D.; Li, F.; Cao, D.; Chen, X., Defect Engineering in MoSe2 for the Hydrogen Evolution Reaction: From Point Defects to Edges. *ACS Applied Materials & Interfaces* **2017,** *9* (49), 42688-42698.

103. Ramanathan, A. A., Defect Functionalization of MoS2 nanostructures as toxic gas sensors: A review. *IOP Conference Series: Materials Science and Engineering* **2018,** *305*.

104. Li, B. L.; Setyawati, M. I.; Chen, L.; Xie, J.; Ariga, K.; Lim, C.-T.; Garaj, S.; Leong, D. T., Directing Assembly and Disassembly of 2D MoS2 Nanosheets with DNA for Drug Delivery. *ACS Applied Materials & Interfaces* **2017,** *9* (18), 15286-15296.

105. Kumar, A.; Banerjee, K.; Liljeroth, P., Molecular assembly on two-dimensional materials. *Nanotechnology* **2017,** *28* (8).

106. Ricciardella, F.; Vollebregt, S.; Tilmann, R.; Hartwig, O.; Bartlam, C.; Sarro, P. M.; Sachdev, H.; Duesberg, G. S., Influence of defect density on the gas sensing properties of multi-layered graphene grown by chemical vapor deposition. *Carbon Trends* **2021,** *3*.

107. Linghu, Y.; Wu, C., Gas Molecules on Defective and Nonmetal-Doped MoS2 Monolayers. *The Journal of Physical Chemistry C* **2019,** *124* (2), 1511-1522.

108. Hu, Z.; Wu, Z.; Han, C.; He, J.; Ni, Z.; Chen, W., Two-dimensional transition metal dichalcogenides: interface and defect engineering. *Chemical Society Reviews* **2018,** *47* (9), 3100-3128.

109. Grigoropoulos, C. P., Laser synthesis and functionalization of nanostructures. *International Journal of Extreme Manufacturing* **2019,** *1* (1).

110. Mahjouri-Samani, M.; Liang, L.; Oyedele, A.; Kim, Y.-S.; Tian, M.; Cross, N.; Wang, K.; Lin, M.-W.; Boulesbaa, A.; Rouleau, C. M.; Puretzky, A. A.; Xiao, K.; Yoon, M.; Eres, G.; Duscher, G.; Sumpter, B. G.; Geohegan, D. B., Tailoring Vacancies Far Beyond Intrinsic Levels Changes the Carrier Type and Optical Response in Monolayer MoSe2−x Crystals. *Nano Letters* **2016,** *16* (8), 5213-5220.

111. Sun, L.; Banhart, F.; Warner, J., Two-dimensional materials under electron irradiation. *MRS Bulletin* **2015,** *40* (1), 29-37.

112. Hu, L.; Shan, X.; Wu, Y.; Zhao, J.; Lu, X., Laser Thinning and Patterning of MoS2 with Layer-by-Layer Precision. *Scientific Reports* **2017,** *7* (1).

113. Tosun, M.; Chan, L.; Amani, M.; Roy, T.; Ahn, G. H.; Taheri, P.; Carraro, C.; Ager, J. W.; Maboudian, R.; Javey, A., Air-Stable n-Doping of WSe2 by Anion Vacancy Formation with Mild Plasma Treatment. *ACS Nano* **2016,** *10* (7), 6853-6860.

114. Chee, S. S.; Lee, W. J.; Jo, Y. R.; Cho, M. K.; Chun, D.; Baik, H.; Kim, B. J.; Yoon, M. H.; Lee, K.; Ham, M. H., Atomic Vacancy Control and Elemental Substitution in a Monolayer Molybdenum Disulfide for High Performance Optoelectronic Device Arrays. *Advanced Functional Materials* **2020,** *30* (11).

115. Zhang, H.; Huang, J. X.; Wang, Y. W.; Liu, R.; Huai, X. L.; Jiang, J. J.; Anfuso, C., Atomic force microscopy for two-dimensional materials: A tutorial review. *Opt Commun* **2018,** *406*, 3-17.

116. He, S.; Tian, R.; Wu, W.; Li, W.-D.; Wang, D., Helium-ion-beam nanofabrication: extreme processes and applications. *International Journal of Extreme Manufacturing* **2021,** *3* (1).

117. Liang, Q.; Gou, J.; Arramel; Zhang, Q.; Zhang, W.; Wee, A. T. S., Oxygen-induced controllable p-type doping in 2D semiconductor transition metal dichalcogenides. *Nano Research* **2020,** *13* (12), 3439-3444.

118. Gao, L.; Hu, Z.; Lu, J.; Liu, H.; Ni, Z., Defect-related dynamics of photoexcited carriers in 2D transition metal dichalcogenides. *Physical Chemistry Chemical Physics* **2021,** *23* (14), 8222-8235.

119. Hong, J.; Jin, C.; Yuan, J.; Zhang, Z., Atomic Defects in Two-Dimensional Materials: From Single-Atom Spectroscopy to Functionalities in Opto-/Electronics, Nanomagnetism, and Catalysis. *Advanced Materials* **2017,** *29* (14).

120. Enyashin, A. N.; Bar-Sadan, M.; Houben, L.; Seifert, G., Line Defects in Molybdenum Disulfide Layers. *The Journal of Physical Chemistry C* **2013,** *117* (20), 10842-10848.

121. Mitterreiter, E.; Schuler, B.; Cochrane, K. A.; Wurstbauer, U.; Weber-Bargioni, A.; Kastl, C.; Holleitner, A. W., Atomistic Positioning of Defects in Helium Ion Treated Single-Layer MoS2. *Nano Letters* **2020,** *20* (6), 4437-4444.

122. Zan, R.; Ramasse, Q. M.; Jalil, R.; Georgiou, T.; Bangert, U.; Novoselov, K. S., Control of Radiation Damage in MoS2 by Graphene Encapsulation. *ACS Nano* **2013,** *7* (11), 10167-10174.

123. Lee, J.; Kim, C.; Choi, K.; Seo, J.; Choi, Y.; Choi, W.; Kim, Y.-M.; Jeong, H. Y.; Lee, J. H.; Kim, G.; Park, H., In-situ coalesced vacancies on MoSe2 mimicking noble metal: Unprecedented Tafel reaction in hydrogen evolution. *Nano Energy* **2019,** *63*.

124. Bilgin, I.; Raeliarijaona, A. S.; Lucking, M. C.; Hodge, S. C.; Mohite, A. D.; de Luna Bugallo, A.; Terrones, H.; Kar, S., Resonant Raman and Exciton Coupling in High-Quality Single Crystals of Atomically Thin Molybdenum Diselenide Grown by Vapor-Phase Chalcogenization. *ACS Nano* **2018,** *12* (1), 740-750.

125. Mehta, P.; Sarma, A.; Ghosh, J.; Pandya, S.; Pandya, S.; Choudhuri, P.; Govindarajan, J.; Schrittwieser, C. I.; Schrittwieser, R., Temperature profile measurement of graphite material using a CO2 laser. *Phys Scripta* **2010,** *82* (5).

126. Butler, S. Z.; Hollen, S. M.; Cao, L.; Cui, Y.; Gupta, J. A.; Gutiérrez, H. R.; Heinz, T. F.; Hong, S. S.; Huang, J.; Ismach, A. F.; Johnston-Halperin, E.; Kuno, M.; Plashnitsa, V. V.; Robinson, R. D.; Ruoff, R. S.; Salahuddin, S.; Shan, J.; Shi, L.; Spencer, M. G.; Terrones, M.; Windl, W.; Goldberger, J. E., Progress, Challenges, and Opportunities in Two-Dimensional Materials Beyond Graphene. *ACS Nano* **2013,** *7* (4), 2898-2926.

127. Zhang, X.; Tan, Q. H.; Wu, J. B.; Shi, W.; Tan, P. H., Review on the Raman spectroscopy of different types of layered materials. *Nanoscale* **2016,** *8* (12), 6435-6450.

128. Tonndorf, P.; Schmidt, R.; Bottger, P.; Zhang, X.; Borner, J.; Liebig, A.; Albrecht, M.; Kloc, C.; Gordan, O.; Zahn, D. R. T.; de Vasconcellos, S. M.; Bratschitsch, R., Photoluminescence emission and Raman response of monolayer MoS2, MoSe2, and WSe2. *Opt Express* **2013,** *21* (4), 4908-4916.

129. Bhimanapati, G. R.; Lin, Z.; Meunier, V.; Jung, Y.; Cha, J.; Das, S.; Xiao, D.; Son, Y.; Strano, M. S.; Cooper, V. R.; Liang, L. B.; Louie, S. G.; Ringe, E.; Zhou, W.; Kim, S. S.; Naik, R. R.; Sumpter, B. G.; Terrones, H.; Xia, F. N.; Wang, Y. L.; Zhu, J.; Akinwande, D.; Alem, N.; Schuller, J. A.; Schaak, R. E.; Terrones, M.; Robinson, J. A.,

Recent Advances in Two-Dimensional Materials beyond Graphene. *Acs Nano* **2015,** *9* (12), 11509-11539.

130. Zhang, Y.; Chang, T. R.; Zhou, B.; Cui, Y. T.; Yan, H.; Liu, Z. K.; Schmitt, F.; Lee, J.; Moore, R.; Chen, Y. L.; Lin, H.; Jeng, H. T.; Mo, S. K.; Hussain, Z.; Bansil, A.; Shen, Z. X., Direct observation of the transition from indirect to direct bandgap in atomically thin epitaxial MoSe2. *Nature Nanotechnology* **2014,** *9* (2), 111-115.

131. Yu, Z. G.; Yakobson, B. I.; Zhang, Y.-W., Realizing Indirect-to-Direct Band Gap Transition in Few-Layer Two-Dimensional MX2 (M = Mo, W; X = S, Se). *ACS Applied Energy Materials* **2018,** *1* (8), 4115-4121.

132. Song, X. F.; Hu, J. L.; Zeng, H. B., Two-dimensional semiconductors: recent progress and future perspectives. *Journal of Materials Chemistry C* **2013,** *1* (17), 2952-2969.

133. Huang, J.; Yang, L.; Liu, D.; Chen, J.; Fu, Q.; Xiong, Y.; Lin, F.; Xiang, B., Large-area synthesis of monolayer WSe2 on a SiO2/Si substrate and its device applications. *Nanoscale* **2015,** *7* (9), 4193-4198.

134. Huang, J.-K.; Pu, J.; Hsu, C.-L.; Chiu, M.-H.; Juang, Z.-Y.; Chang, Y.-H.; Chang, W.-H.; Iwasa, Y.; Takenobu, T.; Li, L.-J., Large-Area Synthesis of Highly Crystalline WSe2 Monolayers and Device Applications. *ACS Nano* **2013,** *8* (1), 923-930.

135. Brekhov, K. A.; Grishunin, K. A.; Ilyin, N. A.; Shestakova, A. P.; Lavrov, S. D.; Mishina, E. D., Optical Diagnostics of WSe2 Monolayers. *Technical Physics Letters* **2018,** *43* (12), 1112-1114.

136. Gutierrez, H. R.; Perea-Lopez, N.; Elias, A. L.; Berkdemir, A.; Wang, B.; Lv, R.; Lopez-Urias, F.; Crespi, V. H.; Terrones, H.; Terrones, M., Extraordinary Room-Temperature Photoluminescence in Triangular WS2 Monolayers. *Nano Letters* **2013,** *13* (8), 3447-3454.

137. Zhan, Y. J.; Liu, Z.; Najmaei, S.; Ajayan, P. M.; Lou, J., Large-Area Vapor-Phase Growth and Characterization of MoS2 Atomic Layers on a SiO2 Substrate. *Small* **2012,** *8* (7), 966-971.

138. Lv, R.; Robinson, J. A.; Schaak, R. E.; Sun, D.; Sun, Y.; Mallouk, T. E.; Terrones, M., Transition Metal Dichalcogenides and Beyond: Synthesis, Properties, and Applications of Single- and Few-Layer Nanosheets. *Accounts of Chemical Research* **2015,** *48* (1), 56-64.

139. Shi, Y.; Li, H.; Li, L.-J., Recent advances in controlled synthesis of two-dimensional transition metal dichalcogenides via vapour deposition techniques. *Chemical Society Reviews* **2015,** *44* (9), 2744-2756.

140. Liu, H. F.; Wong, S. L.; Chi, D. Z., CVD Growth of MoS2-based Two-dimensional Materials. *Chemical Vapor Deposition* **2015,** *21* (10-11-12), 241-259.

141. Choi, W.; Choudhary, N.; Han, G. H.; Park, J.; Akinwande, D.; Lee, Y. H., Recent development of two-dimensional transition metal dichalcogenides and their applications. *Materials Today* **2017,** *20* (3), 116-130.

142. Eichfeld, S. M.; Hossain, L.; Lin, Y.-C.; Piasecki, A. F.; Kupp, B.; Birdwell, A. G.; Burke, R. A.; Lu, N.; Peng, X.; Li, J.; Azcatl, A.; McDonnell, S.; Wallace, R. M.; Kim, M. J.; Mayer, T. S.; Redwing, J. M.; Robinson, J. A., Highly Scalable, Atomically Thin WSe2 Grown via Metal–Organic Chemical Vapor Deposition. *ACS Nano* **2015,** *9* (2), 2080-2087.

143. Yue, R.; Nie, Y.; Walsh, L. A.; Addou, R.; Liang, C.; Lu, N.; Barton, A. T.; Zhu, H.; Che, Z.; Barrera, D.; Cheng, L.; Cha, P.-R.; Chabal, Y. J.; Hsu, J. W. P.; Kim, J.; Kim, M. J.; Colombo, L.; Wallace, R. M.; Cho, K.; Hinkle, C. L., Nucleation and growth of WSe2: enabling large grain transition metal dichalcogenides. *2D Materials* **2017,** *4* (4), 045019.

144. Zhan, L.; Wan, W.; Zhu, Z.; Shih, T.-M.; Cai, W., MoS2 materials synthesized on SiO2/Si substrates via MBE. *Journal of Physics: Conference Series* **2017,** *864*.

145. Bulgakova, N. M.; Bulgakov, A. V., Pulsed laser ablation of solids: transition from normal vaporization to phase explosion. *Appl Phys a-Mater* **2001,** *73* (2), 199-208.

146. Lowndes, D. H.; Geohegan, D. B.; Puretzky, A. A.; Norton, D. P.; Rouleau, C. M., Synthesis of Novel Thin-Film Materials by Pulsed Laser Deposition. *Science* **1996,** *273* (5277), 898-903.

147. Mahjouri-Samani, M.; Gresback, R.; Tian, M.; Wang, K.; Puretzky, A. A.; Rouleau, C. M.; Eres, G.; Ivanov, I. N.; Xiao, K.; McGuire, M. A., Pulsed laser deposition of photoresponsive two-dimensional GaSe nanosheet networks. *Advanced Functional Materials* **2014,** *24* (40), 6365-6371.

148. Mahjouri-Samani, M.; Liang, L. B.; Oyedele, A.; Kim, Y. S.; Tian, M. K.; Cross, N.; Wang, K.; Lin, M. W.; Boulesbaa, A.; Rouleau, C. M.; Puretzky, A. A.; Xiao, K.; Yoon, M.; Eres, G.; Duscher, G.; Sumpter, B. G.; Geohegan, D. B., Tailoring Vacancies Far Beyond Intrinsic Levels Changes the Carrier Type and Optical Response in Monolayer MoSe2-x Crystals. *Nano Letters* **2016,** *16* (8), 5213-5220.

149. Saito, R.; Tatsumi, Y.; Huang, S.; Ling, X.; Dresselhaus, M. S., Raman spectroscopy of transition metal dichalcogenides. *J Phys-Condens Mat* **2016,** *28* (35).

150. Pawbake, A. S.; Pawar, M. S.; Jadkar, S. R.; Late, D. J., Large area chemical vapor deposition of monolayer transition metal dichalcogenides and their temperature dependent Raman spectroscopy studies. *Nanoscale* **2016,** *8* (5), 3008-3018.

151. Sugawara, H.; Ohkubo, T.; Fukushima, T.; Iuchi, T. In *Emissivity measurement of silicon semiconductor wafer near room temperature*, SICE 2003 Annual Conference (IEEE Cat. No.03TH8734), 4-6 Aug. 2003; 2003; pp 2201-2204 Vol.2.

152. Sopori, B.; Chen, W.; Madjdpour, J.; Ravindra, N. M., Calculation of emissivity of Si wafers. *Journal of Electronic Materials* **1999,** *28* (12), 1385-1389.

153. Li, H.; Li, Y.; Aljarb, A.; Shi, Y.; Li, L.-J., Epitaxial Growth of Two-Dimensional Layered Transition-Metal Dichalcogenides: Growth Mechanism, Controllability, and Scalability. *Chemical Reviews* **2017,** *118* (13), 6134-6150.

154. Kumar, S.; Schwingenschlögl, U., Thermoelectric Response of Bulk and Monolayer MoSe2 and WSe2. *Chemistry of Materials* **2015,** *27* (4), 1278-1284.

155. Zavabeti, A.; Jannat, A.; Zhong, L.; Haidry, A. A.; Yao, Z.; Ou, J. Z., Two-Dimensional Materials in Large-Areas: Synthesis, Properties and Applications. *Nano-Micro Letters* **2020,** *12* (1).

156. Lee, J.; Pak, S.; Giraud, P.; Lee, Y.-W.; Cho, Y.; Hong, J.; Jang, A. R.; Chung, H.-S.; Hong, W.-K.; Jeong, H. Y.; Shin, H. S.; Occhipinti, L. G.; Morris, S. M.; Cha, S.; Sohn, J. I.; Kim, J. M., Thermodynamically Stable Synthesis of Large-Scale and Highly Crystalline Transition Metal Dichalcogenide Monolayers and their Unipolar n-n Heterojunction Devices. *Advanced Materials* **2017,** *29* (33).

157. Terrones, H.; Corro, E. D.; Feng, S.; Poumirol, J. M.; Rhodes, D.; Smirnov, D.; Pradhan, N. R.; Lin, Z.; Nguyen, M. A. T.; Elías, A. L.; Mallouk, T. E.; Balicas, L.; Pimenta, M. A.; Terrones, M., New First Order Raman-active Modes in Few Layered Transition Metal Dichalcogenides. *Scientific Reports* **2014,** *4* (1).

158. Tonndorf, P.; Schmidt, R.; Bottger, P.; Zhang, X.; Borner, J.; Liebig, A.; Albrecht, M.; Kloc, C.; Gordan, O.; Zahn, D. R.; Michaelis de Vasconcellos, S.; Bratschitsch, R., Photoluminescence emission and Raman response of monolayer MoS(2), MoSe(2), and WSe(2). *Opt Express* **2013,** *21* (4), 4908-16.

159. Fang, L.; Chen, H.; Yuan, X.; Huang, H.; Chen, G.; Li, L.; Ding, J.; He, J.; Tao, S., Quick Optical Identification of the Defect Formation in Monolayer WSe2 for Growth Optimization. *Nanoscale Research Letters* **2019,** *14* (1).

160. Kanik, A.; Sarma, A.; Ghosh, J.; Elumalai, A.; Pandya, S.; Bhope, K.; Manchanda, R., Temperature response of laser heated emissive probe materials under vacuum and free atmospheric conditions. *Laser Physics* **2021,** *31* (1).

161. Mazumder, J.; Kar, A., Photolytic LCVD. In *Theory and Application of Laser Chemical Vapor Deposition*, 1995; pp 123-214.

162. Hunter, N.; Azam, N.; Zobeiri, H.; Van Velson, N.; Mahjouri-Samani, M.; Wang, X., Interface Thermal Resistance between Monolayer WSe2 and SiO2 : Raman Probing with Consideration of Optical–Acoustic Phonon Nonequilibrium. *Adv Mater Interfaces* **2022,** *9* (7).

163. Molina-Sánchez, A.; Wirtz, L., Phonons in single-layer and few-layer MoS2and WS2. *Physical Review B* **2011,** *84* (15).

164. Lee, C.; Jeong, B. G.; Yun, S. J.; Lee, Y. H.; Lee, S. M.; Jeong, M. S., Unveiling Defect-Related Raman Mode of Monolayer WS2 via Tip-Enhanced Resonance Raman Scattering. *ACS Nano* **2018,** *12* (10), 9982-9990.

165. Wang, R.; Xu, S.; Yue, Y.; Wang, X., Thermal behavior of materials in laser-assisted extreme manufacturing: Raman-based novel characterization. *International Journal of Extreme Manufacturing* **2020,** *2* (3).

166. Zhang, S.; Zhang, N.; Zhao, Y.; Cheng, T.; Li, X.; Feng, R.; Xu, H.; Liu, Z.; Zhang, J.; Tong, L., Spotting the differences in two-dimensional materials – the Raman scattering perspective. *Chemical Society Reviews* **2018,** *47* (9), 3217-3240.

167. Cançado, L. G.; Jorio, A.; Ferreira, E. H. M.; Stavale, F.; Achete, C. A.; Capaz, R. B.; Moutinho, M. V. O.; Lombardo, A.; Kulmala, T. S.; Ferrari, A. C., Quantifying Defects in Graphene via Raman Spectroscopy at Different Excitation Energies. *Nano Letters* **2011,** *11* (8), 3190-3196.

168. Eckmann, A.; Felten, A.; Mishchenko, A.; Britnell, L.; Krupke, R.; Novoselov, K. S.; Casiraghi, C., Probing the Nature of Defects in Graphene by Raman Spectroscopy. *Nano Letters* **2012,** *12* (8), 3925-3930.

169. Mignuzzi, S.; Pollard, A. J.; Bonini, N.; Brennan, B.; Gilmore, I. S.; Pimenta, M. A.; Richards, D.; Roy, D., Effect of disorder on Raman scattering of single-layerMoS2. *Physical Review B* **2015,** *91* (19).

170. Jayachandran, D.; Oberoi, A.; Sebastian, A.; Choudhury, T. H.; Shankar, B.; Redwing, J. M.; Das, S., A low-power biomimetic collision detector based on an in-memory molybdenum disulfide photodetector. *Nature Electronics* **2020,** *3* (10), 646-655.

171. Moody, G.; Tran, K.; Lu, X.; Autry, T.; Fraser, J. M.; Mirin, R. P.; Yang, L.; Li, X.; Silverman, K. L., Microsecond Valley Lifetime of Defect-Bound Excitons in Monolayer WSe2. *Physical Review Letters* **2018,** *121* (5).

172. Liu, H.; Wang, C.; Liu, D.; Luo, J., Neutral and defect-induced exciton annihilation in defective monolayer WS2. *Nanoscale* **2019,** *11* (16), 7913-7920.

173. Mondal, N.; Azam, N.; Gartstein, Y. N.; Mahjouri-Samani, M.; Malko, A. V., Photoexcitation Dynamics and Long-Lived Excitons in Strain-Engineered Transition Metal Dichalcogenides. *Advanced Materials* **2022**.

174. Wang, S.; Robertson, A.; Warner, J. H., Atomic structure of defects and dopants in 2D layered transition metal dichalcogenides. *Chemical Society Reviews* **2018,** *47* (17), 6764-6794.

175. Susarla, S.; Kutana, A.; Hachtel, J. A.; Kochat, V.; Apte, A.; Vajtai, R.; Idrobo, J. C.; Yakobson, B. I.; Tiwary, C. S.; Ajayan, P. M., Quaternary 2D Transition Metal Dichalcogenides (TMDs) with Tunable Bandgap. *Advanced Materials* **2017,** *29* (35).